

AD-A149 609

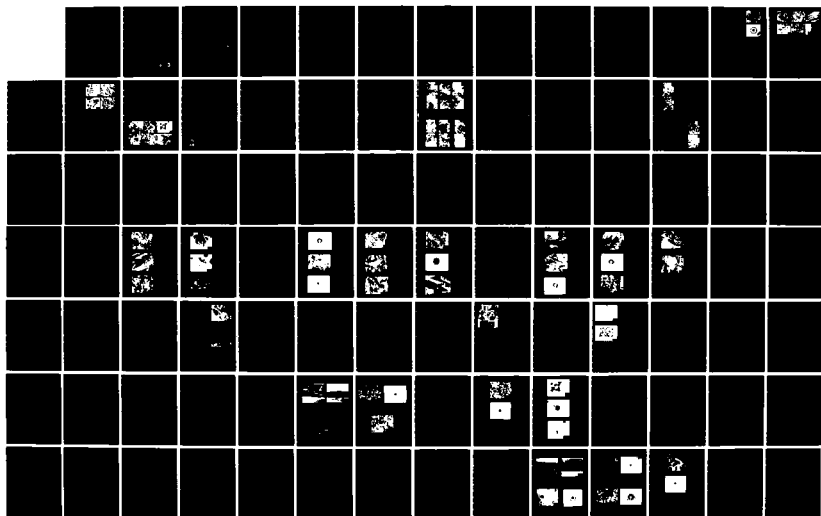
ALLOY DEVELOPMENT PROCESSING AND CHARACTERIZATION OF
DEVITRIFIED TITANIUM. (U) NORTHEASTERN UNIV BOSTON MA
BARNETT INST OF CHEMICAL ANALYSIS. S H WHANG DEC 84
N00014-82-K-0597

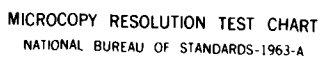
1/2

UNCLASSIFIED

F/G 11/6

NL





MICROCOPY RESOLUTION TEST CHART
NATIONAL BUREAU OF STANDARDS-1963-A

12

ALLOY DEVELOPMENT, PROCESSING AND CHARACTERIZATION OF
DEVITRIFIED TITANIUM BASE MICROCRYSTALLINE ALLOYS

AD-A149 609

ANNUAL REPORT
CONTRACT - N00014-82-K-0597

FOR
OFFICE OF NAVAL RESEARCH
ARLINGTON, VA 22217

DECEMBER, 1984

S.H. WHANG

BARNETT INSTITUTE OF CHEMICAL ANALYSIS AND MATERIALS SCIENCE
NORTHEASTERN UNIVERSITY, BOSTON, MA 02115

DTIC
ELECTE

JAN 15 1985

This document has been approved
for public release and sale; its
distribution is unlimited.

85 01 08 059

| REPORT DOCUMENTATION PAGE | | READ INSTRUCTIONS BEFORE COMPLETING FORM |
|--|---|---|
| 1. REPORT NUMBER | 2. GOVT ACCESSION NO. A149609 | 3. RECIPIENT'S CATALOG NUMBER |
| 4. TITLE (and Subtitle) ALLOY DEVELOPMENT, PROCESSING AND CHARACTERIZATION OF DEVITRIFIED TITANIUM BASE MICROCRYSTALLINE ALLOYS | | 5. TYPE OF REPORT & PERIOD COVERED Annual Report September 1983-August 1984 |
| 7. AUTHOR(s) S.H. Whang | | 6. PERFORMING ORG. REPORT NUMBER |
| 9. PERFORMING ORGANIZATION NAME AND ADDRESS 341 Mugar, Northeastern University Barnett Institute of Chem. Anal. & Mat. Science Boston, MA 02115 | | 8. CONTRACT OR GRANT NUMBER(s) N00014-82-K-0597 |
| 11. CONTROLLING OFFICE NAME AND ADDRESS Office of Naval Research 800 N. Quincy St. Arlington, VA 22217 | | 10. PROGRAM ELEMENT, PROJECT, TASK AREA & WORK UNIT NUMBERS |
| 14. MONITORING AGENCY NAME & ADDRESS (if different from Controlling Office) | | 12. REPORT DATE December 1984 |
| | | 13. NUMBER OF PAGES 109 |
| | | 15. SECURITY CLASS. (of this report) Unclassified |
| | | 15a. DECLASSIFICATION/DOWNGRADING SCHEDULE |
| 16. DISTRIBUTION STATEMENT (of this Report) This document has been approved for public release and its distribution is unlimited. Reproduction in whole or in part is permitted by the U.S. Government. | | |
| 17. DISTRIBUTION STATEMENT (of the abstract entered in Block 20, if different from Report) <div style="text-align: right;">DTIC SELECTE JAN 15 1985 A</div> | | |
| 18. SUPPLEMENTARY NOTES | | |
| 19. KEY WORDS (Continue on reverse side if necessary and identify by block number) Rapidly solidified Ti alloy, arc melt spinning, rare earth dispersoid, Ostwald ripening of rare earth dispersoids, age hardening in rapidly solidified Ti alloy, alpha Ti alloys, high temperature Ti alloys | | |
| 20. ABSTRACT (Continue on reverse side if necessary and identify by block number) Principles that govern metastability in rapidly solidified Ti alloys have been investigated with respect to solid solubility and phase transformation. Sub- sequent heat treatment in ternary Ti alloys results in precipitation reaction between group IIIA or IVA elements and rare earth metals in the absence of Ti. The Ostwald ripening of these binary dispersoids (rare earth metals Y, La, Er Al or Sn compounds) has been and is being studied. Characteristics such as transient coarsening behavior and very slow coarsening in these dispersoids | | |

DEPARTMENT OF DEFENSE FORMS

. DD Form 1473: Report Documentation Page

SECURITY CLASSIFICATION OF THIS PAGE (When Data Entered)

were identified. Mechanical properties (hardness) of alloy ribbon and splat were studied through isochronal and isothermal heat treatment. The alloy ingot was consolidated from alloy flakes by HIPing and is being studied with respect to mechanical properties.

SECURITY CLASSIFICATION OF THIS PAGE (When Data Entered)

TABLE OF CONTENTS

ABSTRACT

| | | |
|----|---|----|
| 1. | SUMMARY OF PRINCIPAL RESULTS | 1 |
| 2. | RAPIDLY SOLIDIFIED Ti ALLOYS CONTAINING NOVEL ADDITIVES | 4 |
| 3. | RAPIDLY SOLIDIFIED Ti ALLOYS CONTAINING METALLOIDS AND RARE EARTH METALS - THEIR MICROSTRUCTURE AND MECHANICAL PROPERTIES | 12 |
| 4. | THERMAL STABILITY OF PRECIPITATES IN A RAPIDLY QUENCHED Ti-Al-Si ALLOY | 20 |
| 5. | MICROSTRUCTURAL CHARACTERISTICS OF RAPIDLY QUENCHED ALPHA-Ti ALLOYS CONTAINING La | 28 |
| 6. | SECOND PHASE COARSENING IN Ti-5Si-4.5La SYSTEM | 67 |
| 7. | PILOT SCALE ARC MELT SPINNING PROCESS FOR Ti RICH ALLOYS | 72 |
| 8. | MICROSTRUCTURES AND AGE HARDENING OF RAPIDLY QUENCHED Ti-Zr-Si ALLOYS | 77 |
| 9. | PRECIPITATION HARDENING OF RAPIDLY QUENCHED Ti-Zr-B ALLOYS | 92 |

| | |
|--------------------|--|
| Accession For | |
| NTIS GRA&I | <input checked="checked" type="checkbox"/> |
| DTIC TAB | <input type="checkbox"/> |
| Unannounced | <input type="checkbox"/> |
| Justification | |
| By | |
| Distribution/ | |
| Availability Codes | |
| Dist | Avail and/or Special |
| A1 | |



ABSTRACT

Principles that govern metastability in rapidly solidified Ti alloys have been investigated with respect to solid solubility and phase transformation. Subsequent heat treatment in ternary Ti alloys results in precipitation reaction between group IIIA or IVA elements and rare earth metals in the absence of Ti. The Ostwald ripening of these binary dispersoids (rare earth metals [Y, La, Er] - Al or Sn compounds) has been and is being studied. Characteristics such as transient coarsening behavior and very slow coarsening in these dispersoids were identified. Mechanical properties (hardness) of alloy ribbon and splat were studied through isochronal and isothermal heat treatment. The alloy ingot was consolidated from alloy flakes by HIPing and is being studied with respect to mechanical properties.

SUMMARY OF PRINCIPAL RESULTS

The scope of rapidly solidified (RS) Ti alloy research at Northeastern University covers three principal areas: 1) a study of heat transport in arc melting and casting during arc melt spinning of Ti alloys; 2) microstructural studies as a function of heat treatment, including precipitation, and identification, morphology and stability of dispersoids; 3) an investigation of structure-property relations in RS Ti alloy at various stages of heat treatment.

PROCESSING

Rapid solidification processing (RSP) by arc melt spinning has advantages over other techniques in many ways. It is contamination-free, inexpensively operated, and results in high quench rates (10^5 - 10^6 K/sec). Since the heat transport and temperature profile of Ti melt in the cold copper crucible are not well known, melting experiments in a cold copper crucible by arc heating were conducted using Ti-6.3Si alloy. The temperature measurement at both the surface and the bottom of the alloy button were performed by optical pyrometer and thermocouple, respectively, as a function of nominal input power. The results show that: 1) in the molten state, the heat transfer coefficient of the alloy at the interface between the melt and crucible is ~ 0.6 W/cm²-K; 2) the temperature gradient in the melt reaches as high as ~ 100 deg/mm; 3) radiation loss at the surface of the molten alloy is significant at this temperature; 4) the estimated quench rate of Ti alloy ribbon and splat from the heat transfer coefficient ranges from 5×10^5 to 5×10^6 K/sec.

Currently, one charge of 20g alpha-Ti alloy is routinely processed into ribbon. Continuous melting and casting requires preheating of feed alloy. The spinning unit for this purpose is planned for modification in the fiscal year 1985/1986.

MICROSTRUCTURE

a) SOLID SOLUBILITY BY RAPID QUENCHING

Increased solid solubility of alloys by rapid quenching is widely known. In binary Ti alloys, the extended solid solubility varies significantly depending upon phase diagram features. More specifically, the solubility of solute increases significantly in alloy systems having β -eutectoid transformation such as Ti-Cr, Mn, Fe, Co, Ni, etc. By contrast, no distinct increase in solubility due to rapid quenching is observed in alloy systems having peritectoid transformations except for B and C. Examples are Ti-Ge, Ti-R.E. (where R.E. is Ce, La,...). A large solubility of B and C in Ti is a result of interstitial solution, but some questions about the occupying lattice site have been raised since the increased lattice parameter of Ti-B is smaller than would occur when all boron atoms occupy interstitial sites. On the other hand, rapid quenching stabilizes β phase against α phase in β -isomorphous type phase diagrams. For instance, as in Ti-Mo, Ti-Ta, Ti-Nb, etc.

b) PRECIPITATION

Super saturated solid solution of additive elements results in

precipitation upon heat treatment. The precipitates in ternary Ti alloys (under high vacuum) take non-Ti, non-oxide binary compounds. Dispersoids in Ti-5Sn-4.5La were identified as La_2Sn (B8_2). Currently, precipitates in Ti-5Sn-3Y, Ti-5Sn-5.4Er and Ti-2.5Al-5.4Er alloys are being investigated. Experimental techniques for identification includes carbon extraction replica, diffraction ring pattern, micro-diffraction and x-ray diffraction.

c) PARTICLE COARSENING

In the past, qualitative observations have shown that particle coarsening of rare earth dispersoids in Ti is slower than in metalloid dispersoids. Present investigations aim at exploring the kinetic aspects of particle coarsening in ternary Ti alloy systems. Some of the experimental results are listed in Table 1. The low coarsening rate of the precipitates in Ti-5Sn-3Y and Ti-5Sn-4.5La are distinctive, which indicates that the lower diffusivity of rare earth metals is responsible for the slow coarsening, provided the diffusivity of Sn is similar to the self-diffusivity of Ti at 800°C (they are virtually the same above 950°C). Nevertheless, a high coarsening rate in a Ti-Al-Er system appears to contradict the foregoing results. In order to clear up the confusion, it is important to investigate the possibility that a coupled diffusion between rare earth metals (Er) and alloying elements might operate. Currently, the Ti-Sn-Er system is under study for this objective. During the study of particle coarsening in the Ti-Sn-Y and Ti-Al-Er alloys, it was found that none of the single diffusion mechanisms can explain the transient coarsening occurring in the Ti-5Sn-3Y and the Ti-2.5Al-5.4Er alloys at 800°C. Nevertheless, the polynomial equation ($\sum r^n$, where $n = 1, 2, 3, \dots$) can fit the coarsening curve. In addition, the microstructure shows that in the early stage of annealing a large fraction of precipitates is associated with a subgrain boundary. Further detailed studies are underway to understand the diffusion mechanisms involved in this transient coarsening behavior.

In summary, current results suggest that further investigation is needed in: a) the controlling mechanism of rare earth particle coarsening, i.e., rare earth diffusion control or a coupled diffusion mechanism; b) diffusion mechanisms involving the transient coarsening behavior being investigated; c) the prime reason for the discrepancy in coarsening rates among rare earth metals.

MECHANICAL PROPERTIES

Emphasis is placed on mechanical behavior of alloy ribbon at the aged state and the HIPed from flake materials.

Age hardened ribbon alloy exhibits a relatively moderate increase in hardness in contrast with splat alloy. This appears to be associated with less fine microstructures resulting from the low cooling rate, which in turn has to do with the "lift-off" in the substrate-side ribbon surface.

Presently, produced ribbons were chopped into pieces 2~3mm long and HIPed at 900°C. The mechanical properties (hot hardness) and the microstructures are being characterized.

Table 1

| Alloy System At. % | Coarsening Rate at 800°C in α phase (m ³ /sec) | Compound Structure | Estimated diffusion coefficient at 800°C (cm ² /sec) |
|-----------------------|--|---|--|
| Ti-5Sn-3Y | $\sim 5 \times 10^{-28}$ | under study | under study |
| Ti-5Sn-4.5La | $\sim 9 \times 10^{-29}$ | La ₂ Sn (B8 ₂) | $\sim 4 \times 10^{-14}$ (La) |
| Ti-2.5Al-5.4Er | $\sim 8 \times 10^{-26}$ | under study | under study |
| Ti-5Al-2Si | $\sim 3 \times 10^{-26}$ | Ti ₅ Si ₃ (D8 ₈) | $\sim 1 \times 10^{-11}$ (Si) |

Coarsening rate = $(r^3 - r_0^3)/t$ where r and t are average particle radius and annealing time, respectively. Self-diffusivity of Ti is $\sim 2 \times 10^{-12}$ cm²/sec (800°C).

RAPID SOLIDIFIED TI ALLOYS CONTAINING NOVEL ADDITIVES

S.H. Whang

Journal of Metals, Vol. 36, No. 4, 1984, pp. 34-40

Rapidly Solidified Ti Alloys Containing Novel Additives

S. H. Whang

SUMMARY

The rapid solidification of Ti alloys by an arc plasma melt spinning technique is reviewed. Attention is given to the melt spinning technique, and guidelines for the selection of alloying additives are presented. As a new approach for Ti alloy processing, the devitrification of Ti-rich glasses is introduced and discussed. The microstructures of several rapidly solidified Ti alloys which remain crystalline are described for the as-quenched as well as heat-treated conditions. Preliminary results on the age-hardening response of rapidly solidified Ti alloys are also discussed and their thermal stability is reviewed.

INTRODUCTION

In recent years, there is an increased interest in the development of high-specific-strength and high-temperature alloys through rapid solidification processing (RSP). RSP offers a distinct advantage: small amounts of elements that normally have nearly no solid solubility in titanium at room temperature can be homogeneously dissolved in titanium through RSP. Subsequent heat treatment of such alloys can form precipitates which give rise to additional strengthening at moderate or, depending on the precipitate stability, even at highly elevated temperature. As a result, RSP offers alloy designers more flexibility than ever before to control microstructure as well as to select alloy compositions.

Rapid solidification of Ti alloys has been previously studied using melt extraction techniques based on the conventional alloy compositions without additives.¹ However, new approaches for the syntheses of rapidly solidified (RS) Ti alloys include the devitrification (or crystallization) of glassy phase² and the rapid solidification of the molten alloys containing metalloids³⁻⁵ or rare-earth elements.^{6,7} Upon heat treatment, these alloys yield various second phases which comprise of compounds based on (a) Ti-metalloids (B, Si), (b) rare-earth metalloids, (c) rare-earth group III or IVA metals, and (d) rare-earth interstitial (C, N, O). Microstructures and mechanical properties of rapidly solidified Ti alloys depend significantly on the type of second phases. Aspects of RSP of Ti alloys as well as some current results of such processing are reviewed in the following.

MELT SPINNING TECHNIQUE

While some of the techniques for rapidly solidified Ti alloy processing have been previously summarized,⁴ the technique of melt spinning of Ti alloys is new. The advantage of the melt spinning processes lies in the fact that extremely refined microstructures of good uniformity can be attained through the high cooling rate derived from the geometry of the ribbon. Previously, many different melt spinning processes for Ti alloy have been available; these include the pendant drop melt extraction, the crucible melt extraction,⁸ and the arc plasma melt spinning.⁹ The extraction processes are different from the arc plasma process in that the extraction spinning depends on a natural contact mode (i.e., "free fall and contact") in the drop melt extraction and a "contact and drag" mode in the crucible melt extraction. This contrasts with the orifice-shaped, high-velocity molten jet in the arc plasma melt spinning. Thus, instead of a half-circled wire, the product in the plasma melt spinning is a thin ribbon. A pilot-scale, arc plasma melt spinning unit is shown in Figure 1 and consists primarily of three functional parts: melting compartment A, melt spinning compartment B, and ribbon processing chamber C. The pre-melted alloy ingot is charged directly into a cold copper crucible while additional granule alloy is continually supplied by an auto-feeder to maintain the molten alloy level. When the melt is adequately superheated, additional inert gas is introduced into compartment A creating a pressure differential between

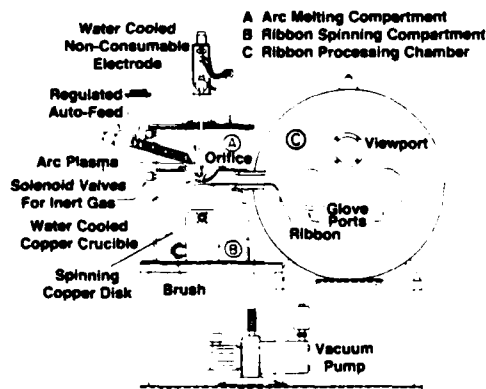


Figure 1. Schematic drawing of pilot arc plasma melting spinning unit.

the melting and the spinning compartments. As a result, the molten alloy forms a jet through the orifice centered at the bottom of the crucible. The jet subsequently impinges onto the highly conductive spinning disk underneath the crucible and rapidly solidifies into ribbons or flakes depending on the disk employed. The ribbon or the flake can be further processed into particulates by means of mechanical pulverization in the chamber before discharging or canning under the protective environment. Detailed description of the pilot-scale arc melt spinning process is given elsewhere.¹⁰

ADDITIVE ELEMENTS

It is well known that a small amount of Si additions to Ti alloys improve their creep resistance.¹¹ In RS Ti alloys, other metalloids and rare-earth elements can also be used as additives to provide the second phases for high-temperature properties. Since extended solid solubility of normally insoluble element can be achieved via rapid quenching from liquid, the choice of the additive element is quite broad, in particular, it includes metalloids to rare-earth metals.

The benefits of these alloying additives in Ti alloys are twofold: (a) while both types of additives have very low solubilities at room temperature, they may be rapidly solidified into solution and (b) they both have the potential of forming thermally stable compounds. In fact, both metalloids and rare-earth metals have similarities as well as dissimilarities in atomic nature; they have unfilled P shells and a large atomic size difference from that of titanium. The dissimilarities are that metalloids have a large electronegativity difference as well as high negative heat of solution in titanium, whereas rare-earth elements have the opposite characteristics. As a result, the metalloid prefers to form compound phases directly with titanium, but the rare-earth element tends to form an immiscible phase due to the positive heat of solution. Alternatively, the rare-earth elements can produce compound phases in the Ti matrix with other elements such as metalloids (B, Si), interstitials (C, N, O) or group IIIA, IVA metals (Al, Sn, Ge, etc.).

There is also an important contrast between the solubility of the metalloid and the rare-earth element upon rapid quenching. The metalloids (B, C, Si) have an extended solubility range of 6-10 at.%, this is larger than the maximum equilibrium solubility at the eutectoid temperature.⁶ On the other hand, the rare-earth elements (La, Ce) have a range of less than 0.6 at.% which in turn is smaller than the maximum equilibrium solubility at α -transus.⁶ Microscopically, the small metalloid atom can occupy either the interstitial site or substitutional site or both, while the rare-earth atom can only replace Ti atom at the substitutional site. The combined effects of the unfavorable atomic size as well as atomic interaction make the rare-earth elements the least soluble elements in titanium. The morphology and thermal stability of second phases based either metalloids or rare-earth elements are an important basis for determining which type of additives is most promising; this will be discussed later.

DEVITRIFIED (DV) Ti ALLOYS

The principal advantage of a devitrified (DV) Ti alloy (i.e., one which has been quenched to an amorphous state and is subsequently crystallized by heat treatment) is that extremely fine and homogeneous microstructures can be generated from a glassy phase. The microstructures in DV Ti alloys are genetically different from those in rapidly solidified microcrystalline alloys. When the glassy phase undergoes crystallization, the initial crystallized phase is that which has the lowest critical energy for crystallization, not necessarily the one which has the lowest free energy.¹² For this reason, frequently unknown metastable alloy phases occur in the early stage of the crystallization. As a result, the crystallization process in glassy metals often produces different phase mixtures from those in the rapidly solidified crystalline alloys.

The synthesis of DV alloy must satisfy one stringent compositional requirements; the alloy composition must be glass-forming at the given cooling rate. Although glass forming tendencies in binary and ternary alloy systems can be estimated using a phenomenological model,¹³⁻¹⁵ the following empirical expression is useful in determining the glass forming ability of a given alloy at the cooling rate of $\sim 10^6$ K/s:

$$\text{Ti}_x(\text{Zr, Hf, V, Mo etc.})_y(\text{Si, B, Fe, Co, Ni, Cu etc.})_z$$

where $x \geq 50$ at.%, $y \leq 30$ at.%, and $z = 20-30$ at.%. As the cooling rate increases, the z value can be reduced below 20 at.%. The elements in the first parenthesis normally have extended solid solubility in titanium while

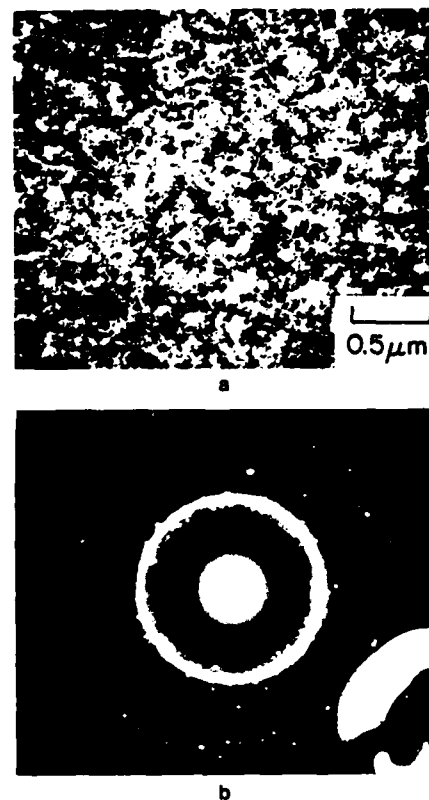


Figure 2. Microstructures of $\text{Ti}_{65}\text{Zr}_6\text{Al}_4\text{Ni}_{10}\text{B}_{12}$ glass after crystallization at $550^\circ\text{C}/2$ h; (a) bright field and (b) selected area diffraction pattern.

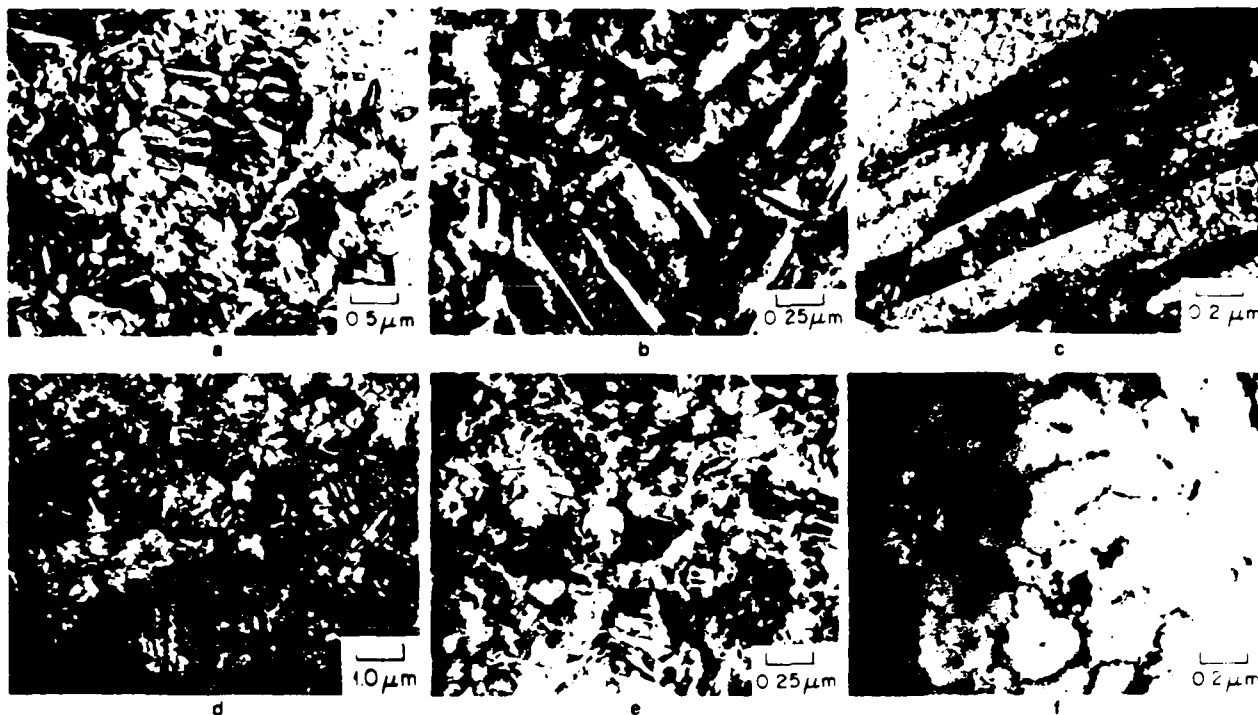


Figure 3. Microstructures of splat-quenched Ti alloys. (a) Ti-5Al-2.5Sn-1B. (b) Ti-5Al-3La. (c) Ti-5Al-2.5Sn-3Ce. (d) Ti-18.2Zr-1.3B. (e) Ti-17.9Zr-3.3Si. and (f) Ti-8Mo-2.3Al-3.5Si.

the elements in the second parenthesis tend to form eutectics with titanium. Using the above relationship, alloys based on the late-transition metal-rich glass or metalloid-rich glass can be synthesized. In either case, the crystallization results in very high-volume fraction of one or more intermetallic phases.

As an example of a DV Ti alloy, $Ti_{88}Zr_{6}Al_4Ni_{12}B_{12}$ (at %) has been quenched into glassy phase and crystallized by the succeeding heat treatment. Figures 2a and b show the microstructure of the crystallized alloy and the corresponding diffraction pattern in which split rings derived from the typical amorphous diffused ring are distinctive. The crystallized "grain size" at this stage is extremely small, being less than 100 Å diameter.

RAPIDLY SOLIDIFIED (MICROCRYSTALLINE) Ti ALLOYS

RSP of crystalline Ti alloys offers improvements in mechanical properties based not only on the refinement of existing α - β microstructures during rapid quenching but also on new phase formation through heat treatment. Both the ability to form finely dispersed precipitate particles and their subsequent high-temperature stability are essential to rapidly solidified Ti alloy design. Microstructural characteristics of rapidly solidified Ti alloys can be conveniently described in three different stages: as quenched, annealed at intermediate temperatures, and annealed at high temperatures.

Microstructures

As-Quenched. In general, microstructural refinement of Ti alloys can be attained through rapid quenching.¹⁶ Furthermore, a small amount of an additive element can alter microstructural characteristics of the as-quenched state. Such additive elements exist in the as-quenched state either in the form of a supersaturation solid solution or in the form of solute cluster. Figures 3a, b, c show micrographs for α -Ti alloys containing B, La, and Ce, respectively. In all alloys, a well-developed, very fine acicular α microstructure is present. A careful observation shows that when the concentration of rare-earth metals exceeds the maximum extended solubility, precipitation occurs along a sub-grain boundary network. This network of sub-grain boundaries is only observed if an excess amount of the rare-earth element is present. The sub-grain size is also approximately inversely proportional to the content of the rare earth element.¹⁷ In the Zr-rich alloy, an extremely refined martensite structure is present and is combined with dendritic structure in the background as shown in Figures 3d and e. However, the Mo-rich alloy (Figure 3f) exhibits a clear cellular structure with an absence of martensite structure.

Annealing at Intermediate Temperature. When rapidly solidified Ti alloys are subjected to heat treatment at a range of 500-700°C, the resulting microstructural changes include G.P. zone-like precipitation and disappearance of both martensite and sub-grain boundaries. No apparent grain growth can be detected at this stage. In the rapidly solidified alloys containing either metalloids or rare-earth elements, precipitation is a universal phenomenon. The Ti-3La alloy annealed at 700°C/2 h exhibits cuboidal precipitates (Figure 4a) while the Ti-5Al-2.5Sn-3La alloy annealed under the same conditions yields fine precipitates of spherical shape (Figure 4b). These precipitates in the Ti-5Al-3La and Ti-5Al-2.5Sn-3La have been identified as Al₃La (orthorhombic) and Al₃La(C15) from the selected area diffraction rings and as a non-oxide form from EELS.⁶ Previously, the dispersoids in a Ti-rare-earth system was found to be rare-earth oxide, i.e., Y₂O₃ in Ti-8Al-4Y (at.%),¹⁷ etc. In addition to the nucleation and growth of compound phases, both the fine-scale martensite structure and the sub-grain boundaries disappear as the grain structure becomes more distinctive (Figures 4c and d). At this stage, the particle shapes and morphologies can be identified. For example, the boride particle has a needle or rod shape in contrast with the polyhedral or spherical shape of silicide and carbide particles. However, all rare-earth precipitates in ternary and quaternary alloys are spherical. These discrepancies are summarized in Table I.

Annealing at High Temperature. After exposure of the rapidly solidified Ti alloys to high temperatures significant microstructural coarsening may occur (900-950°C). Extensive Ostwald ripening occurs in all of the metalloid-containing alloys (Figures 5a-d). In contrast, the coarsening of precipitate is minimal in the alloys containing rare-earth additives (Figures 5e and f). In all cases, the grain size increases to 1-2 µm diameter after the exposure at 900-950°C/2 h.

Depending upon additive element, the morphological characteristics of the precipitates become distinctively different after high-temperature annealing. The silicide particle tends to coarsen along the grain boundary while the boride with a rod shape takes random orientation. The rare-earth precipitates remain relatively uniform in distribution but some precipitate-free zone formation begins at this stage.

Mechanical Properties

Rapidly solidified Ti alloys can show a strong enhancement in hardness in the aged condition even after high-temperature annealing. This is primarily a consequence of precipitation hardening, the stages of which are described below for the rapidly solidified Ti alloys.

As-Quenched State. A significant hardness increase occurs after rapid quench primarily due to the supersaturation of additive elements and microstructural refinements. The supersaturation of 1 at.% metalloid in the Ti alloy increases the hardness by 4-13% from that of the base alloy. In contrast, the

TABLE I: Dependence of Particle Space and Morphology on Additive Elements

| Additive | Compound | Age Hardening (Temperature) | Particle Shape | Particle Morphology | Ref. |
|----------|---|-----------------------------|-------------------------|---|-------|
| Si | Ti ₃ Si ₃ | Yes (550-700°C) | Polyhedral or spherical | Grain boundary precipitate and coarsening | 6 |
| B | TiB | Yes (550-700°C) | Needle or rod | Random | 3 |
| C | TiC | No (700°C) | Spherical | Uniform | 6 |
| Y | Y ₂ O ₃ | Yes (500-700°C) | Spherical or cuboidal | Uniform | 17, 3 |
| La | Al ₃ La & Al ₃ La | Yes (500-700°C) | Spherical | Uniform | 6 |

TABLE II: Microhardness of As-Quenched and Heat-Treated Alloys*

| Alloy Composition, wt.% | As-Quenched, GPa | Aged, GPa | High Temperature Annealing, GPa |
|------------------------------|------------------|-----------------|---------------------------------|
| Ti-5Al-2.5Sn-3C _e | 4.3 | 5.8 (600°C/2 h) | 4.0 (900°C/2 h) |
| Ti-5Al-2.5Sn-1B | 5.7 | 6.8 (600°C/2 h) | 4.9 (900°C/2 h) |
| Ti-5Al-4Zr-2.5Sn-3La | 6.4 | 7.5 (700°C/2 h) | 5.4 (900°C/2 h) |
| Ti-18Zr-4.4Si | 5.5 | 5.6 (550°C/4 h) | 3.9 (850°C/2 h) |
| Ti-7.7Zr-3.4Al-3.6Si | 4.5 | 5.6 (700°C/2 h) | 4.7 (900°C/2 h) |
| Ti-8.2Mo-2.3Al-1.4B | 4.8 | 5.4 (700°C/2 h) | 4.5 (900°C/2 h) |
| Ti-6Al-4V-2.2Si | 4.1 | 6.4 (500°C/2 h) | 4.6 (900°C/2 h) |
| Ti-5Al-2.5Sn | 3.6 | --- | --- |

*Based on sputter foils of 20 µm thick

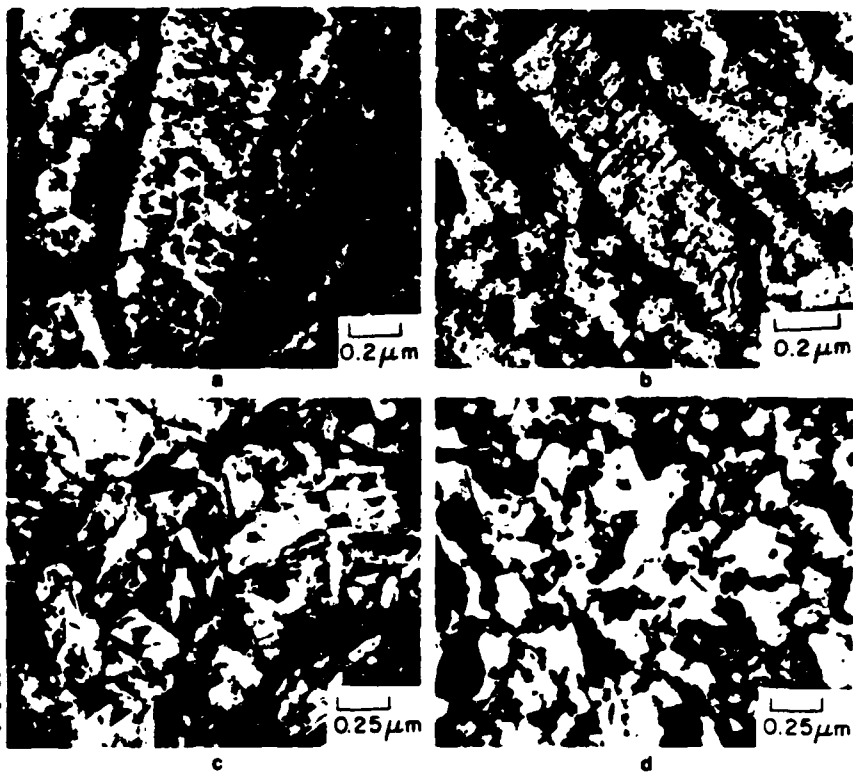


Figure 4. Microstructures of aged alloys: (a) Ti-3La, 700°C/2 h, (b) Ti-5Al-2.5Sn-3La, 700°C/2 h, (c) Ti-18.2Zr-1.3B, 550°C/24 h, and (d) Ti-17.9Zr-3.3Si, 550°C/20 h.

same amount of rare-earth metals causes an increase of 20-47% from the same standard.⁶ These large increases are proportional to the atomic misfit parameter of the rare-earth atom and Ti atom.⁶ However, when the concentration of rare-earth additives is increased above 1 at.%, the hardness instead begins to decrease.

Aged State. The most important and universal phenomenon in rapidly solidified Ti alloys is the presence of age hardening. A typical age hardening response is shown in Figure 6. The hardness increase per atomic percent is much higher in the rare-earth-containing alloy than in the metalloid-containing alloy. As an exception, the alloys containing carbon apparently do not age harden (at least at 700°C), even though a very large solubility of carbon is observed as well as a large strength increase in the as-quenched state is noted. As is the case in the as-quenched state, age hardening is a function of an atomic misfit parameter in the alloys containing rare-earth additives (Figure 7).³ Isochronal annealing treatments of as-quenched specimens indicate a difference in behavior between alloys based on single-phase α or α - β Ti alloys. Specifically, over-aging occurs at a much lower temperature in α - β alloys than in α -type alloy (Figure 8). This is probably due to the fact that the high diffusivity (and possibly a higher solubility) of the additive elements in β phase accelerates particle coarsening. In other alloys, a large drop in hardness occurs at or above 800°C. Also, it is observed that alloying elements such as zirconium and tin are effective in delaying or impeding the over-aging process in rapidly solidified alloys.

High Temperature Exposure. As would be expected, annealing the age-hardened rapidly solidified Ti alloys at 900°C causes a decline in hardness associated primarily with the second-phase coarsening, and secondarily with other microstructural coarsening. It is observed that the precipitate coarsening varies significantly depending upon the type of alloying additive. The grain size remains sub-micron in most alloys even after 900°C 2 h. The hardness, which at this stage is still as much as 20% higher than that of the as-quenched condition, after aging, and after high-temperature anneal, is listed in Table II.

SECOND-PHASE COARSENING

The potential for developing high-temperature Ti alloys based on RSP relies heavily on the thermal stability of the second phase derived from the alloying additives. In Figure 5a-d, extensive particle coarsening occurs

in the alloys containing metalloids, (C, B, Si) upon being exposed to anneals in the range 800-900°C. The coarsening is characterized by morphological differences between silicide, carbide, and boride particles.

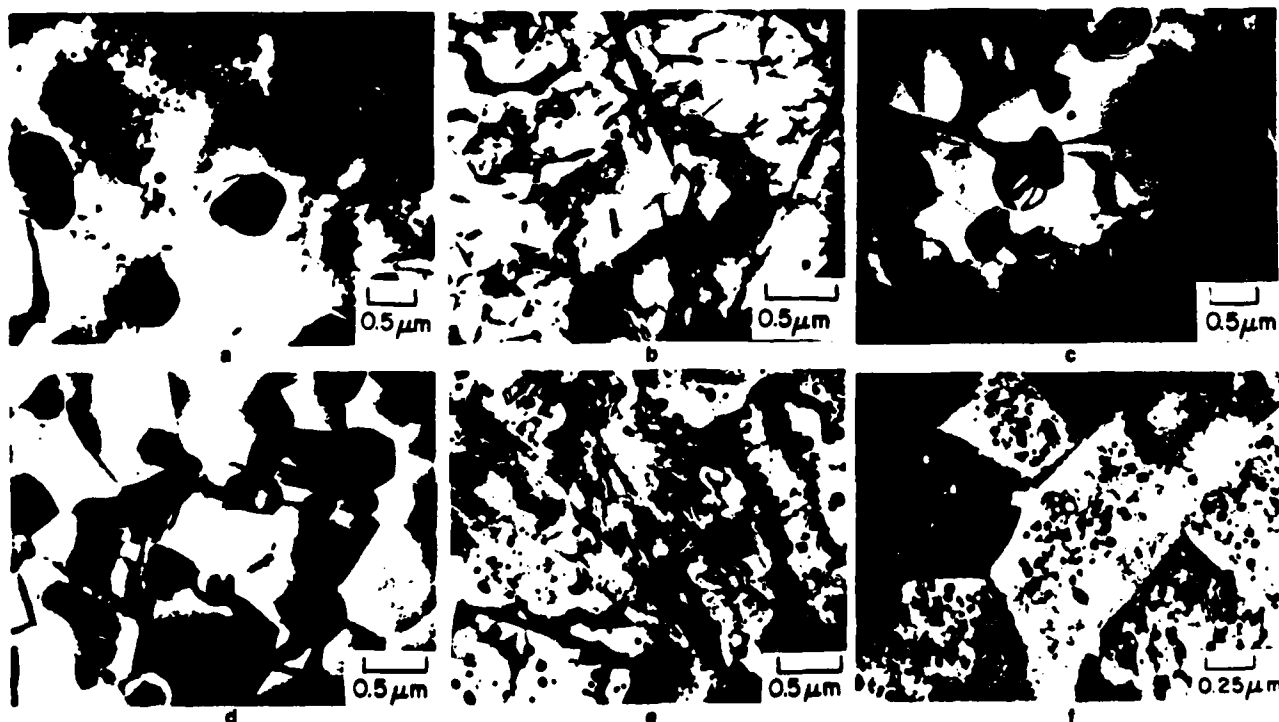
A study of the coarsening kinetics for Ti-5Al-2Si alloy has been conducted by transmission electron microscopy in the range of 600-800°C. The average particle diameter as a function of the annealing time for 700-800°C of particle diameter and the soaking time agree with Wagner's lattice diffusion model, but the data for 600°C is better described by a high diffusivity model.¹⁸ Similarly rapid coarsening kinetics at low temperature has been previously observed in rapidly quenched Al alloy systems.¹⁹ It should be noted that lattice diffusion coarsening may occur in the bulk form of these alloys due to an absence of a high dislocation density.

In contrast to the metalloid-containing alloys, Figures 5e and f show a resistance to coarsening in the rare-earth alloys. Therefore, at 900°C the particle coarsening in the Ti alloy containing the rare-earth elements (La, Ce) appears to be lower by an order of magnitude than those of the alloys containing the metalloids (C, B, Si). As a result, particles of 1000 Å diameter remain stable (see Figures 5e and f).

EFFECTS OF COOLING RATE

It is well established that microstructural features such as dendrite arm spacing, grain size, cell size, second-phase inclusion size, etc., are exponential functions of the average cooling rate. Any enhancement of the mechanical properties is a consequence of the combined effects of one or more of the microstructural refinements. Therefore, the relationship between the two quantities, i.e., the cooling rate and the mechanical property is only meaningful under well-defined circumstances. The effects of the cooling rates on hardness in rapidly solidified Ti alloys are evident both in the as-quenched state and after intermediate temperature annealing. There is an approximately 10% decrease in microhardness from 20 μm to the 40 μm .⁶ The estimated change in cooling rates is a factor of two, assuming a Newtonian cooling in which the average cooling rate is inversely proportional to the sample thickness and directly to the heat transfer coefficient between the sample and the substrate.²⁰ In the present case, the ribbon is cooled by a substrate from one surface and by a gas medium from the other surface. The gas cooling is three or four orders of magnitude smaller than that of substrate quenching. Hence, the cooling rate difference between the ribbon materials and splat materials is roughly a factor of two for the same thickness. It is important to note that the thickness of the as-quenched alloy ribbon thus is a critical parameter if a rapidly solidified Ti alloy is to benefit from rapid solidification processing.

Figure 5. Microstructures of annealed alloys; (a) Ti-5Al-2.5Sn-1C, 950°C/2 h, (b) Ti-18.2Zr-1.3B, 950°C/2 h, (c) Ti-17.9Zr-3.3Si, 950°C/2 h, (d) Ti-7.7Zr-3.4Al-3.6Si, 950°C/2h, (e) Ti-5Al-2.5Sn-3La, 900°C/2 h, (f) Ti-5Al-2.5Sn-3Ce, 900°C/2 h.



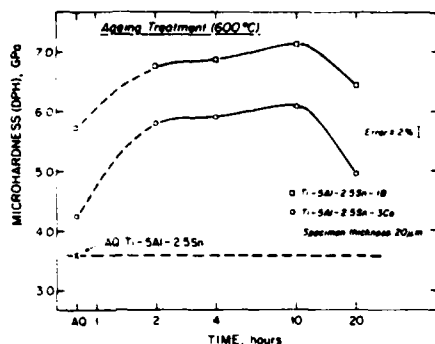


Figure 6. Age treatment at 600°C of RS Ti-5Al-2.5Sn-1B and RS Ti-5Al-2.5Sn-3Ce.

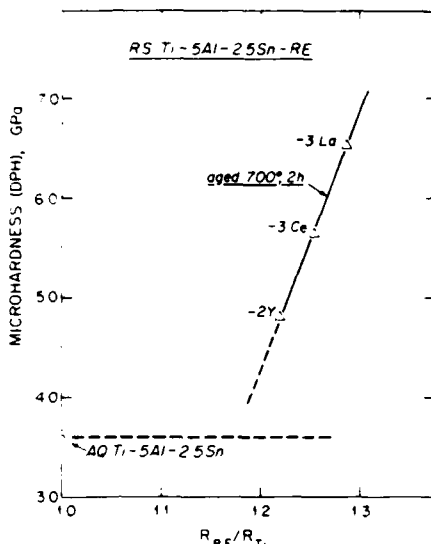


Figure 7. A correlation between microhardness and atomic misfit parameter in Ti-5Al-2.5Sn-2Y (-3Ce, -3La).

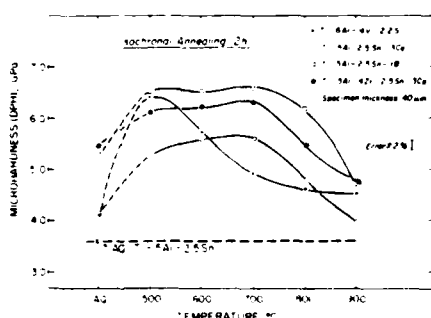


Figure 8. Microhardness as a function of isochronal annealing (2 hours) in rapidly solidified Ti alloys.

CONCLUSION

While preliminary results on some mechanical and microstructural properties of rapidly solidified Ti alloys appear promising there is no doubt that the critical areas remain to be explored in the years ahead. Critical to the development of Ti alloys based on RSP are the following areas:

1. Identification, morphology, and thermal stability of second-phase particles used to strengthen the alloys.
2. Effects of the solidification rate on the both as-quenched and annealed microstructures and the resulting mechanical properties in conjunction with the evaluation of various RSP techniques.
3. The ability to consolidate rapidly solidified Ti alloys into bulk form and to retain the enhanced mechanical properties.
4. The effectiveness of age hardening in structure-sensitive properties such as fatigue, fracture toughness, creep, etc., of bulk materials.

ACKNOWLEDGMENT

The major portion of this article is based on research sponsored by the Office of Naval Research, Contract No. ONR-N00014-82-K-0597. The author thanks Prof. D.A. Koss, Michigan Technological University for many suggestions in the preparation of this manuscript. The author is indebted to Dr. C.S. Chi and Mr. Y.Z. Lu for their enthusiasm and dedication to rapidly solidified Ti alloy research. The author thanks Ms. N. Barnett for the preparation of illustrations. Contribution #194 of the Barnett Institute of Chemical Analysis and Materials Science.

References

1. E.W. Collings, C.E. Mobley, R.E. Maringer, and H.L. Giegel, "Selected Properties of Melt-Extracted Titanium-Based Polycrystalline Alloys," in *Third Int. Conf. Rapidly Quenched Metals III*, edited by B. Cantor, The Metals Society, England, 1978, pp. 188-192.
2. S.H. Whang and Y.Z. Lu, "Aging Behavior of Devitrified Ti Rich Alloys Containing Metalloids," in *Proc. Third Conf. Rapid Solidification Processing*, edited by R. Mehrabian, NBS, 1982, pp. 286-290.
3. C.S. Chi and S.H. Whang, "Effects of Novel Additives (B, Ce) on Microstructural and Mechanical Properties in Rapidly Solidified Alpha Ti Alloys," TMS-AIME, Paper No. F83-14, The Metallurgical Society of AIME, Warrendale, Pennsylvania.
4. S.M.L. Sastry, T.C. Peng, P.J. Meschter, and J.E. O'Neal, "Rapid Solidification Processing of Titanium Alloys," *J. Metals*, 35 (9) (1983), pp. 21-28.
5. A.G. Jackson, T.F. Broderick, F.H. Froese, and J. Motteff, "Effect of Aging on the Microstructure of Rapidly Cooled Ti-5Al-2.5Sn with Si Additions," in *Proc. Third Conf. Rapid Solidification Processing*, edited by R. Mehrabian, NBS, 1982, pp. 585-589.
6. C.S. Chi and S.H. Whang, "Rapidly Solidified Ti Alloys Containing Metalloids and Rare Earth Metals — Their Microstructures and Mechanical Properties," paper presented 1983 Annual Materials Research Society Meeting, November 14-17, 1983, Boston. To be published in the proceedings.
7. S.M.L. Sastry, T.C. Peng, and J.E. O'Neal, "Consolidation, Thermomechanical Processing, and Mechanical Properties of Rapidly Solidified, Dispersion-Strengthened Titanium Alloys," in *Proc. Third Conf. Rapid Solidification Processing*, edited by R. Mehrabian, NBS, 1982, pp. 579-584.
8. R. Maringer and C. Mobley, "Casting of Metallic Filament and Fiber," *J. Vac. Sci. Technology*, 11 (1974), pp. 1067-1071.
9. S.H. Whang and B.C. Giessen, "An Arc Furnace Melt-Spinner for the RSR Processing of Refractory and Reactive Alloys," in *Proc. Third Conf. Rapid Solidification Processing*, edited by Robert Mehrabian, NBS, 1982, pp. 439-442.
10. S.H. Whang, "Pilot Scale Arc Plasma Melt Spinning for Ti and Refractory Alloy," to be submitted to Materials Letters, in preparation.
11. N.E. Paton and M.W. Mahoney, "Creep of Titanium-Silicon Alloys," *Met. Trans.*, 7A (1976), pp. 1685-1694.
12. U. Koster and U. Herold, "Crystallization of Metallic Glasses," in *Glassy Metals I*, edited by H.J. Guntherodt and H. Beck, Springer-Verlag Berlin, Heidelberg, New York, 1981, pp. 225-259.
13. S.H. Whang, "New Prediction of Glass Forming Ability in Binary Alloys Using a Temperature-Composition Map," *Mat. Sci. & Eng.*, 57 (1983), pp. 87-95.
14. S.H. Whang, "Glass Forming Ability for Binary Alloy Systems by Modified T-C Map in Relation to Phase Diagram," presented at Fifth Int. Conf. Liquid & Amorphous Metals, August 1983, *J. Non-Cryst. Sol.*, 61 & 62, Part II, January 1984, pp. 841-846.
15. S.H. Whang, "Glass Forming Property of a Ti-Zr-Si System Determined by Temperature-Composition Map," *Scripta Met.*, 18 (4) (1984).
16. H. Jones, "Some Principles of Solidification at High Cooling Rates," in *Proc. First Int. Conf. on Rapid Solidification Processing*, edited by R. Mehrabian, B. Kear, and M. Cohen, Claitors Publishing Div., Baton Rouge, 1977, pp. 28-45.
17. D.G. Konitzer, B.C. Muddle, and H.L. Fraser, "A Comparison of the Microstructures of As-Cast and Laser Surface Melted Ti-8Al-4Y," *Met. Trans.*, A, 14A (1983), pp. 1979-1988.
18. Y.Z. Lu, S.H. Whang, and B.C. Giessen, "Thermal Stability of Precipitates in Rapidly Quenched Ti-5Al-2Sn Alloys," paper presented at Materials Research Society, November 1983, Boston. To be published in the proceedings.
19. I. Pontikakos and H. Jones, "Coarsening of Intermetallic Particles in Rapidly Solidified Aluminum-Transition-Metal Alloys," *Metal Science*, 16 (1982), pp. 27-30.
20. R.C. Ruhl, "Cooling Rate in Splat Cooling," *Mat. Sci.*, 1 (1967), pp. 313-320.

ABOUT THE AUTHOR



Sung H. Whang, Senior Scientist, Barnett Institute of Chemical Analysis and Materials Science, Northeastern University, Boston, Massachusetts 02115.

Dr. Whang received his BS in metallurgical

engineering at Seoul National University, Korea, and D-Eng Sci in physical metallurgy from Columbia University. He has been with the Barnett Institute since 1978. Currently, he directs the research of a number of sponsored programs including rapidly solidified Ti alloy research. His research interests include rapid solidification processing, microstructural stability and mechanical properties in RS alloys.

thermal stability in Al5 alloys, and metallic glasses, effects of hydrogen on mechanical properties of RS alloys and glassy alloys, and non-equilibrium phase diagram. He is a member of The Metallurgical Society of AIME.

RAPIDLY SOLIDIFIED TI ALLOYS CONTAINING METALLOIDS
AND RARE EARTH METALS - THEIR MICROSTRUCTURE AND MECHANICAL PROPERTIES

C.S. Chi and S.H. Whang

MRS Sym, Vol. 28, 1984, pp. 353-360

RAPIDLY SOLIDIFIED Ti ALLOYS CONTAINING METALLOIDS AND RARE EARTH METALS-- THEIR MICROSTRUCTURE AND MECHANICAL PROPERTIES

C.S. Chi and S.H. Whang, Barnett Institute of Chemical
Analysis and Materials Science, Northeastern University,
Boston, MA 02115

ABSTRACT

Rapidly solidified (RS) Ti alloys containing novel additives were prepared by splat quenching and melt spinning techniques. Microstructures of the as-quenched and heat-treated alloys were studied by electron microscopies. The results show that microstructural refinement and precipitation reaction are universal phenomena in all RS Ti alloys. A significant difference in second phase coarsening was observed between metalloid-origin precipitates and those of rare earth-origin. The precipitates in a Ti-Al-La(Co) were identified predominantly as rare earth-Al compounds. Excellent stability for rare earth-origin precipitates was found.

Except for a carbon-containing alloy (7000C), age hardening behavior is a universal phenomenon in all RS Ti alloys with additives. A significant strength increase (hardness) in the RS alloy was noted at both room and elevated temperatures.

INTRODUCTION

In the last several years, much attention has been paid to high strength and high temperature Ti alloys through rapid solidification processing (RSP). The advantages of RSP for Ti alloys may be that microstructural refinement can be achieved through high cooling rates and in addition, an insoluble element can be incorporated in a Ti matrix through RSP and later precipitated out as a second phase. Therefore, major efforts have been directed toward dispersion hardened Ti alloys containing novel second phases. For such a second phase formation, two groups of additives have been employed. They are: 1) metalloids--B, C, Si; 2) rare earth metals--Y, La, Ce, Nd, Er, etc. Among these elements, Si has already been added to conventional Ti alloys to improve creep resistance. In contrast, some rare earth metals were used as oxygen scavengers in Ti [1]. However, in current RS Ti alloys, both metalloids and rare earth metals play a major role in strengthening the alloy matrices from room to elevated temperatures through second phase formation. The studies show that RS Ti alloys differ significantly from the conventional alloy in microstructure [2], age hardening [3], strength [2,3] particle coarsening [4] and creep strength [5].

In this paper, microstructures and mechanical properties of RS Ti alloys based on splat and ribbon materials will be reviewed.

EXPERIMENTS

Ti rich alloys were quenched rapidly from the melt into foils by the hammer and anvil technique and into ribbons by an arc plasma melt spinning

technique. The samples were sealed in a quartz tube under vacuum 10^{-6} torr and heat treated at various temperatures. Microstructures of as-quenched as well as heat-treated alloys were studied by SEM, TEM, STEM, EDXS, EELS, x-ray, etc. Sample thinning was carried out by twin jet polishing and ion bombardment, or by the combination of both. Microhardness and bend ductility of the as-quenched and heat-treated samples were measured. A careful measurement of the sample thickness was performed before proceeding with further experiments.

SOLUBILITY OF ADDITIVE ELEMENTS

In an equilibrium alloy phase, the solid solubility of an additive element is known to depend on atomic size, electronegativity, and heat of solution of the solute. The solubility of a solute in an equilibrium state has been predicted in a two-dimensional map [6-8] based on the above parameters. In non-equilibrium phases, extended solid solution due to rapid solidification has been observed to obey the same rules, though a systematic shift in the solubility boundary in the map was noted [9]. In E8T alloys, 1) at eutectic temperature, maximum equilibrium solubility is associated with atomic size ratio between the host and solute atoms, i.e., with increasing atomic size mismatch between solvent and solute, solubility declines. Si has the highest solubility among these solute atoms. 2) Size factor provides an explanation for the extended solid solubility of rare earth metals in Ti due to rapid solidification [10]. However, in addition, a very large positive heat of solution is responsible for the low solubility of rare earth metals in Ti. Another explanation for this phenomenon is suggested by Ti-Ce phase diagram. The diagram demonstrates that the super-cooled liquid requires 0.46 TiJ to reach the solidus line from the liquid, where TiJ is reduced liquidus temperature.

MICROSTRUCTURES

In rapidly solidified Ti alloys, microstructural characteristics are significantly different from those of conventional Ti alloys. Some of the most distinctive characteristics are microstructural refinement and precipitation reaction. Since these microstructures change drastically from one particular heat treatment to another, these characteristics have a great influence on the resulting mechanical properties. Details of an individual microstructure will be described in the following.

a) Dendritic and Cellular Structure

Both structures are frequently observed in as-quenched Ti alloys containing Zr or Mo. However, the shape of dendrites is spherical due to rapid quenching from liquid. Furthermore, primary and secondary dendrites are not easily distinguishable from one another. Typical examples of such dendrite structure are shown in Figures 1(a), (b) and (c). The measured size of the primary dendrites in the figures ranges from 0.4 to $0.8 \mu\text{m}$. If the average value $0.6 \mu\text{m}$ is taken, the following analysis can be made using an exponent relation [11,12]:

$$d = AU^{-n}$$

when d : dendritic arm spacing, μm A : materials constant
 U : average cooling rate, $^{\circ}\text{C}/\text{sec}$ n : constant

In order to calculate n value, two extreme A values, 50 and 150, and the cooling rate, $10^6 \text{ }^{\circ}\text{C}/\text{sec}$ are considered. The calculated n values fall

between 0.27 and 0.34. In other words, $n = 0.305 \pm 0.035$. A more accurate determination of n value requires direct cooling rate measurements.

b) Martensite Structure

Ti alloys containing Zr or Mo result in very fine martensite structure upon rapid liquid quenching. Figures 1(a), (b) and (c) show fine martensitic structure inside dendritic structure. The martensite cell size is extremely small compared with those in the conventional Ti alloys. Therefore, it is expected that very high average dislocation density due to such a morphology may exist in the as-quenched alloy. Later, this refined martensite structure changes into a lath-type structure as a result of intermediate temperature annealing as demonstrated in Figure 2(a). This lath-like martensite structure is very similar in shape to that in the conventional alloys. Nevertheless, the lath-like martensite in E8T alloys is much smaller in size than that in the conventional alloys.

c) Grain Structure

In alpha Ti alloys, with increases in cooling rate, the grain size decreases and the shape changes from spherical into acicular or rectangular as shown in Figures 1(d), 2(b) and (c). The width of the acicular grain ranges from 0.2 to $1 \mu\text{m}$. The aspect ratio of width to length is roughly 10 in the alloy quenched at a rate of $\sim 10^6 \text{ }^{\circ}\text{C}/\text{sec}$. A pre-beta grain boundary is also identified, in which all acicular grains take a particular orientation. At high temperature ($900-950^{\circ}\text{C}/2\text{h}$), these fine acicular grains are replaced by circular grains of $\sim 1 \mu\text{m}$ diameter (Figures 3(a), (b) and (c)). In fact, during high temperature annealing ($900-950^{\circ}\text{C}/1-4\text{h}$), grain size in most E8T Ti alloys increases up to $1-2 \mu\text{m}$ diameter.

d) Second Phase

In the past, Si-containing solution-treated and quenched Ti-Alloys have been studied with respect to microstructures and mechanical properties [13,14]. Recently, after being synthesized by liquid quenching, many Ti alloys containing novel additives have exhibited significant differences in microstructures and mechanical properties from those in the Si containing alloys. In particular, the morphology and Ostwald ripening behavior of rare earth-containing Ti alloys are unique. Several atomic percent rare earths can dissolve in the Ti matrix while one atomic percent of rare earth metals (Co, La) in part dissolves and in part exists in a form of cluster ($< 50 \text{ \AA}$). Such clusters appear along sub-grain boundaries as shown in Figure 1(d). It was found in Ti-6Al-4V-xLa system where x is 1-4 wt. % [15] that the sub-grain size is inversely proportional to the concentration of rare earth metals. However, no increased cluster size after increasing the concentration was noted. Aging at temperatures between $550-700^{\circ}\text{C}/2\text{h}$ results in uniform precipitates in the matrix (Figures 2(b),(c)) or precipitation from solid solution (Figure 2(d)) while these network-like sub-grains disappear. It should be pointed out that in the Ti-5Al-3La alloy, the majority of precipitates due to a rare earth additive (La) turn out to be $\text{Al}_3\text{La}(\text{Hex. DO}_{19})$ and $\text{Al}_4\text{La}(\text{Orth. D}_{13})$ compounds [10] instead of rare earth oxides.

In high temperature annealing ($900-950^{\circ}\text{C}$), it was observed that a significant difference in particle coarsening behavior exists between the metalloid and the rare earth containing alloys. For examples, Figures 3(a), (b) and (d) show coarse particles in the metalloid-containing alloys, in contrast with fine particles in the Ti-5Al-2.58-3Ce (Figure 3(c)). Morphological differences between the particles from different additives is also clearly demonstrated in these figures. Boride precipitates tend to

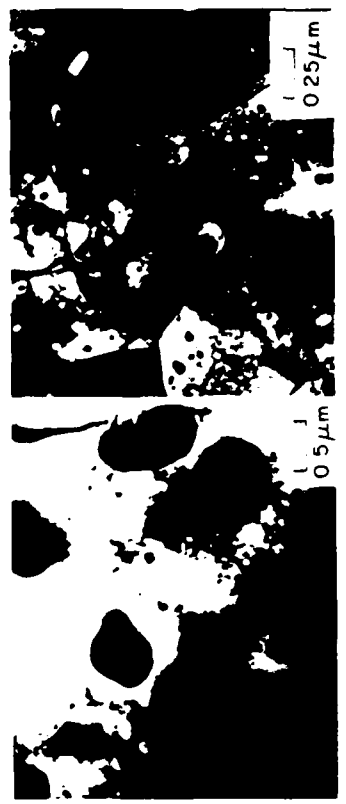
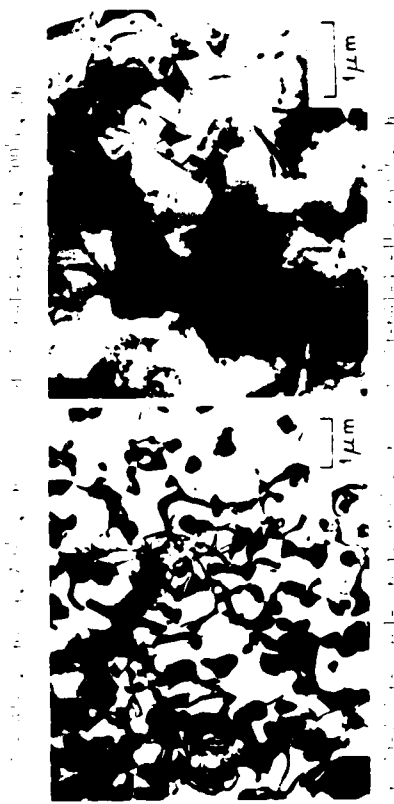


Fig. 1. Scanning electron micrographs of the surface of the sample annealed at 1000°C for 100 h. (a) Secondary electron image (SEI) and (b) backscattered electron image (BEI-TOPO).

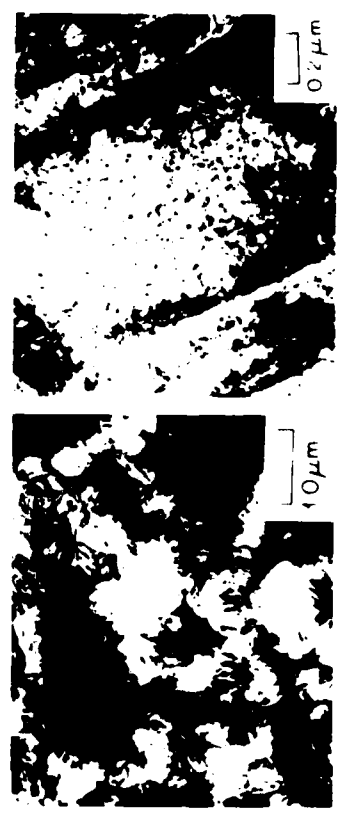
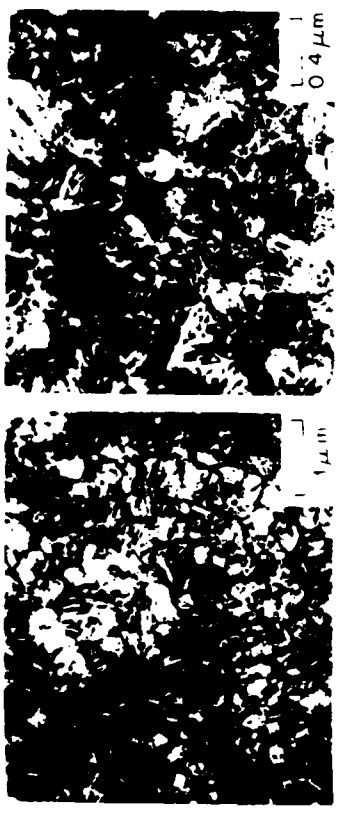


Fig. 2. Scanning electron micrographs of the surface of the sample annealed at 1000°C for 100 h. (a) Secondary electron image (SEI) and (b) backscattered electron image (BEI-TOPO).

grow in acicular or rod shape. On the other hand, all other particles (silicide, boride or rare earth-origin (Ce,La) particles) take spherical shapes.

MECHANICAL PROPERTIES

Concomitant with their distinctive microstructural characteristics, unique mechanical properties of RS Ti alloys have been reported. They are high strength, creep resistance, and age hardening.

a) As-Quenched Alloy

It has been shown that a rapidly quenched alloy shows very refined microstructures, including martensitic structure, sub-grain structure, grain structure, and dendritic structure. In addition, what is not shown in the micrograph is the solid solution of additive elements. The additive elements have two extreme atomic sizes—much smaller or much larger atoms than the Ti atom. Hence, in both cases, the extended solid solution of the additive results in a large strain field in the Ti matrix, regardless of types of lattice sites the additive atom occupies. Let's consider strength increase due to the additive element alone. Total alloy strength may be written as

$$\sigma_{\text{total}} = \sigma_0 + (\sigma_e + \sigma_G) + \sigma_{\text{H.P.}}$$

where σ_0 : conventional alloy strength without additive
 σ_e : strength increment due to atomic volume misfit
 σ_G : strength increment due to modulus mismatch
 $\sigma_{\text{H.P.}}$: Hall-Petch type strength increase due to microstructural refinement such as grain, uncut particles and martensite structure, etc.

In as-quenched alloys, where the additive element dissolves homogeneously, the microstructural refinements are roughly equal to each other. Thus, the difference in total strength of different alloys comes from atomic volume misfit and modulus mismatch. Table 1 shows hardness increment per one atomic percent additive element, per atomic volume misfit and per modulus mismatch parameter. There is a correlation between the hardness increment and the atomic misfit parameter, but not between the hardness and modulus mismatch (Figure 4). It appears that in these alloys, atomic volume misfit plays an important role in strength increase, but not modulus mismatch parameter.

b) Heat Treatment

When as-quenched Ti alloys are heat treated at an intermediate temperature, a strong aging response arises. Such enhancement of strength at both room and high temperatures is a microstructural effect of RS Ti alloys containing additives. Figure 5 shows that hardness increase in Ti alloys is a function of annealing time. A strong aging response is shown in the α -type alloys, in contrast with a weak response in the Ti-6Al-4V-2.2Si. However, the real difference is not the intensity of aging. Instead, different overaging behaviors between the α -Ti alloys and the α/β Ti alloy are evidenced in the isochronal annealing (Figure 6). The Ti-6Al-4V-2.2Si alloy exhibits strong aging at 500°C but overages quickly at temperatures as low as 600°C. In other α -Ti alloys, overaging occurs near 800°C. One possible explanation is that diffusivity of Si is faster in the β phase than in the α phase and, therefore, particle coarsening is accelerated in the β phase.

TABLE 1. Relationship between hardness and alloy strengthening parameters

| RS alloy composition | As-quenched microhardness (DPH) GPa | Hardness increment (%) per atomic % | Atomic ^{oo} volume misfit | Modulus ^{oo} mismatch |
|----------------------|-------------------------------------|-------------------------------------|------------------------------------|--------------------------------|
| Ti-5Al-2.5Sn | 3.14 | | | |
| Ti-5Al-2.5Sn-1B | 5.7 | 18 | 0.57 | 5.06 |
| Ti-5Al-2.5Sn-2Y | 4.2 | 33 | 0.87 | 0.75 |
| Ti-5Al-2.5Sn-3Ce | 4.3 | 37 | 0.95 | 0.98 |
| Ti-5Al-2.5Sn-3La | 5.1 | 62 | 1.10 | 0.93 |

* : Atomic volume misfit parameter = $\{(V_B/V_A)/V_A\}$, where V_A, V_B are atomic volumes of solvent and solute.
^{oo} : Modulus mismatch = $\{(G_B^2 - G_A^2)/G_A^2\}^{1/2}$, where G_A, G_B are shear moduli of soft and hard phases

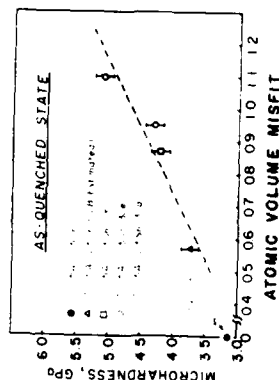


Fig. 4

Fig. 4 Microhardness vs. atomic volume misfit parameter

Fig. 5 Age response in isothermally annealed alloys

Fig. 6 Microhardness in the isochronally annealed alloys

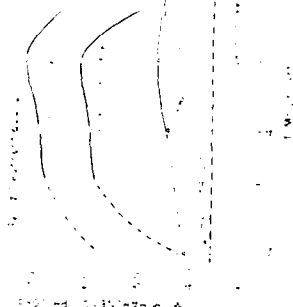


Fig. 5

Fig. 6

THERMAL STABILITY OF PRECIPITATES IN A
RAPIDLY QUENCHED Ti-Al-Si ALLOY

S.H. Whang, Y.Z. Lu, and B.C. Giessen

Proc. MRS Sym, Vol. 28, 1984 pp. 367-373

THERMAL STABILITY OF PRECIPITATES IN A RAPIDLY QUENCHED Ti-5Al-2Si ALLOY*

S.H. WHANG, Y.Z. LU and B.C. GIESSEN

Materials Science Division, Barnett Institute of Chemical Analysis and Materials Science, Northeastern University, Boston, MA 02115

ABSTRACT

Ostwald ripening of precipitates in rapidly solidified Ti-5Al-2Si (wt %) has been studied by TEM. Results show that particle coarsening at 700 and 800°C is controlled by volume diffusion. Diffusion coefficients of Si in α -Ti were found to be $\sim 7.5 \times 10^{-13}$ cm²/sec at 700°C and $\sim 1.2 \times 10^{-11}$ cm²/sec at 800°C. At these temperatures, microstructural refinement due to rapid quenching had no noticeable effect on the coarsening mechanism for the RS Ti-5Al-2Si alloy.

INTRODUCTION

Since the foundation of the theory of particle coarsening was laid by Lifshitz-Slyozov [1] and Wagner [2] (LSW), coarsening characteristics of many different types of particles have been investigated in conventional alloys.

In recent years, alloys with novel second phases and dispersoids have been synthesized in various alloy systems through rapid solidification processing (RSP) combined with the addition of new alloying elements. In particular, many new additives such as metalloids and rare earth metals can be homogeneously dissolved in Ti alloys through RSP. Second phases resulting from these additives play an important role in strengthening the matrices at elevated temperatures [3,4]. The thermal stability of these precipitates then becomes a critical parameter for high temperature applications. In addition, it is important to know the effect of microstructural refinement due to rapid quenching on the coarsening mechanism in RS Ti alloys since very high defect densities and grain refinement exist in alloys quenched from the liquid. However, no study of coarsening in Ti base RS alloys has yet been reported; this is also true for RS alloys in general, with the exception of Al-transition alloy systems [5].

Silicon is often added in conventional Ti alloys to increase creep strength at elevated temperatures [6,7]. Again, there is no report on the Ostwald ripening of Ti silicides or the diffusivity of Si in Ti, although recently a preliminary study on particle coarsening in RS Ti-5Al-2Si has been presented [8]. This paper presents further results and an analysis of the data obtained from this alloy.

EXPERIMENTAL

Alloy buttons were melted several times in an arc furnace under inert gas atmosphere in order to prepare microscopically homogeneous alloys.

*Contribution #192 from the Barnett Institute

Small pieces of these alloy buttons were splat quenched into foils at a cooling rate of $\sim 10^4$ /sec by the hammer and anvil technique. Disk samples (3 mm diameter and $\sim 20 \mu\text{m}$ thick) were punched out from the quenched foils. These samples were annealed in vacuum at 700°C and 800°C for various durations. After annealing, the samples were electropolished and studied by TEM. From the TEM micrographs, the diameters of 400-500 particles were measured for each annealing condition. Also, the microhardness of the alloys was measured as a function of annealing time with a Vickers diamond pyramid tester.

RESULTS

Microstructure

As-quenched Ti-5Al-2Si (Figure 1(a)) shows fine grains of 0.1 to $0.2 \mu\text{m}$ and the absence of precipitates. The former fact represents considerable grain refinement over cast alloys; the latter indicates that Si is dissolved completely in the matrix and is retained upon rapid solidification. The shape of the subgrains in the quenched alloy is spherical, in contrast with the acicular shape found in Ti-5Al-3Si and Ti-5Al-2.5Sn-3Ce [4]. From the electron diffraction ring pattern, the as-quenched alloy was identified as consisting solely of α -Ti s.s. After annealing at 600°C for 4h (Figure 1(b)), the substructure has partially disappeared and nucleation and growth of precipitates have begun; however, at this stage, the volume fraction of the precipitate is still far from its maximum value. Figure 1(c) shows particle coarsening to an average particle radius of $\sim 0.03 \mu\text{m}$ after annealing at 700°C and 4h; the precipitate volume fraction has reached its final, maximum value. The shape of the precipitate is ellipsoidal, but close to spherical in all samples. Annealing at 800°C for 4h results in significant grain growth and further particle coarsening, as shown in Figure 1(d). It is of interest that there is no preferential site for the precipitates at this stage, which is in contrast with the fact that a large portion of precipitate is preferentially located along the grain boundary in the alloys annealed at 900 - 950°C [3].

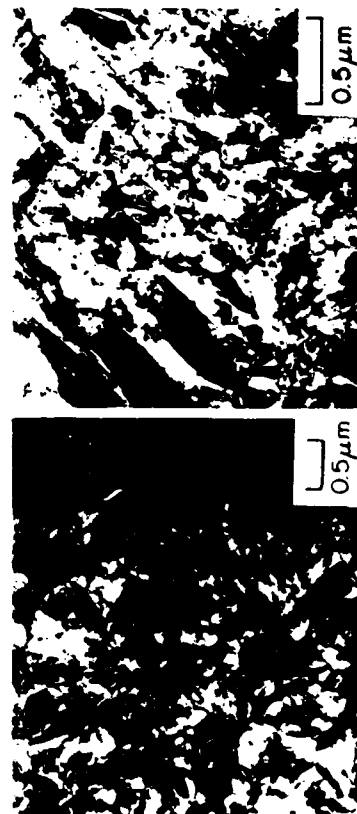
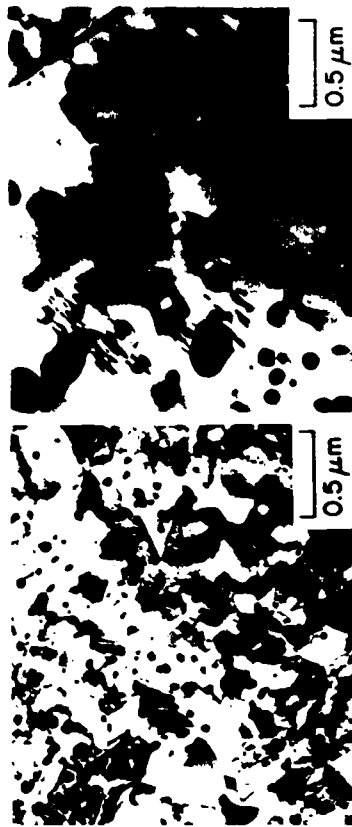


Figure 1(a-d): Microstructure of RS Ti-5Al-2Si alloys



(c) after annealing for 4 h at 700°C (d) after annealing for 4 h at 800°C

Ostwald Ripening

Particle radii measured from TEM micrographs are plotted against annealing time for 700°C and 800°C , respectively (Figure 2). The fact that the observed smooth correlation curves extrapolate to the origin indicates that the coarsening process starts immediately at the beginning of annealing. The particle size distribution, shown in Figure 3, is a skewed Gaussian distribution, a type frequently seen in particle coarsening. The radius of maximum frequency (mode) $r_{\text{mode}} = 1.0$ - $1.2 \bar{r}$ and the cut-off value $r_{\text{max}} = 1.7 \bar{r}$, where \bar{r} is the average particle radius. To test for the dimensionality of the diffusion process, 2nd, 3rd and 4th powers of the average particle radius were plotted against annealing time; only the plots of the 3rd powers with time yield linear correlations at 700°C and 800°C , respectively (Figures 4(a) and (b)). This observation justifies use of the LSW volume diffusion model for particle coarsening in conjunction with the precipitate volume fraction factor [9,10] K to calculate diffusion coefficients D from the observed slope f according to:

$$r^3 - r_0^3 = f(K, T) \cdot (t - t_0) \quad (1)$$

with

$$f(K, T) = \frac{8}{9} \cdot \frac{K \cdot C_s(\infty) \cdot D \cdot \gamma \cdot V_m}{R \cdot T} \quad (1-1)$$

where

$$f(K, T) = \text{measured slope of } \bar{r}^3 \text{ in plot of } \bar{r}^3 \text{ vs } t$$

| | |
|----------------|---|
| r_0, \bar{r} | = average particle radii for the onset and final states |
| K | = volume fraction factor |
| $C_s(\infty)$ | = equilibrium solubility of solute in the matrix with particles of infinite size at a given temperature T |
| D | = diffusion coefficient of solute, cm^2/sec |
| γ | = interfacial free energy of particle, J/m^2 |
| V_m | = gram-molar volume of precipitate, $\text{cm}^3/\text{g-mole}$ |
| t_0, t | = onset and final annealing time, sec |
| R | = gas constant, $\text{J}/\text{mole-K}$ |
| T | = absolute annealing temperature, K . |

The given values and calculated diffusion coefficients are tabulated in Table 1.

TABLE 1. Diffusion coefficients calculated from the slopes $f(K, T)$ taken from plots of r^2 vs t .

| Temp. | $f(K, T)$ (m^2/sec) | (1) | (2) | (3) | (4) |
|-------|----------------------------|-----|----------------|----------------------------------|---------------------------|
| | | K | $C_5 (\omega)$ | V_m ($m^3/g\text{-mole}$) | $D-\gamma$ (J/sec) |
| 700°C | 2.134×10^{-17} | 5.0 | 0.0055 | 0.9377×10^{-5} | 7.53×10^{-17} |
| 800°C | 3.353×10^{-16} | 5.0 | 0.0059 | 0.9377×10^{-5} | 1.22×10^{-15} |
| | | | | | -1.2×10^{-11} |

(1) value from Southoff-Kabliweit [9] and Ardell [10] (SKA)

(2) from Ti-Si phase diagram (Shunk) [17]

(3) calculated from lattice parameter of $Ti_3Si_2(D8_1)$ (Shunk) [17]

(4) assuming interfacial free energy of $1.0 J/m^2$

The microhardnesses of the alloys isothermally annealed at 700 and 800°C are shown in Figure 5. At both temperatures, the hardness had already reached a maximum after annealing for 2h, suggesting that particle coarsening starts within two hours at these temperatures. At long time periods, both curves reach similar values. This is thought to be due to excessive particle coarsening; after annealing at 700°C for 50h and at 800°C for 40h, the particle radii are $0.07 \mu m$ and $0.16 \mu m$, respectively. As a result, the hardness difference between the two alloys annealed at these temperatures for long time periods becomes very small due to significant particle coarsening, showing that the contribution of particles to the matrix strengthening is minimal at these stages.

DISCUSSION

We discuss several of the assumptions underlying the above calculations for $D(Si)$ in Ti.

The results depend sensitively upon the values of the volume fraction factor K derived from theoretical models and the assumed value of the interfacial free energy γ . However, at this time the choice of a model is a matter of convenience since the theory of the volume fraction in coarsening kinetics has not been well established.

The normalized particle size distribution in Figure 6 shows a clear deviation from that predicted by the LSW model. The cut-off value for the present experiment is ~ 1.7 , compared to 1.5 in the LSW model but very close to the value of 1.7 for 8% volume fraction found by Ardell [10].

In order to determine the diffusion coefficients, the precipitate volume was required. It was obtained both through an experimental technique (TEM) and, independently, phase diagram data. However, subsequently only the volume fraction of $\sim 8.2\%$ calculated from the phase diagram was used since the TEM technique appears to slightly overestimate the volume fraction.

The diffusion coefficients shown in Table 1 were calculated using the SKA model. Alternatively, when the volume fraction factor K is taken from the Brailsford-Wynblatt model [11], the relation (1-1) yields the following diffusion coefficients of Si in α -Ti: $\sim 2.1 \times 10^{-15} cm^2/sec$ for 700°C and $\sim 3.4 \times 10^{-11} cm^2/sec$ for 800°C which are larger by a factor ~ 3 than the values from the SKA model. The Si diffusivity values by both models are roughly an order of magnitude larger than the self diffusivity of α -Ti: 1.2

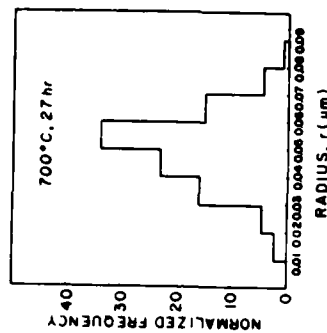


Figure 3: Particle size distribution of precipitate after annealing for 27 h at 700°C.

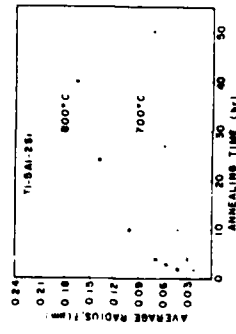
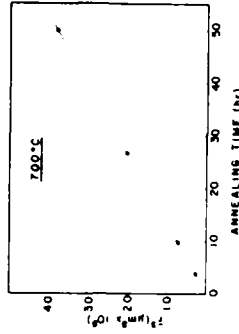
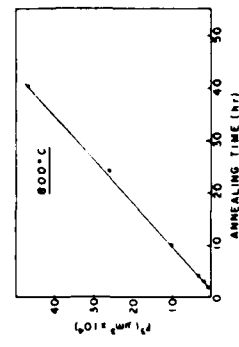


Figure 2: Measured average precipitate particle radius r as a function of annealing time at 700°C and 800°C.



(a) 700°C



(b) 800°C

Figure 4(a,b): Plots of third power of average particle size as a function of annealing time

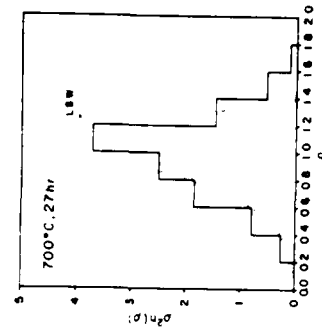


Figure 5: Microhardness as a function of annealing time at 700°C and 800°C.

Figure 6: Particle size distribution from Figure 2 plotted in terms of normalized parameters, where $\rho = r/\bar{r}$.

5. I. Pontikakas and H. Jones, *Materials Science*, **16**, 27 (1982).
6. M.W. Mahoney and N.E. Paton, *Metall. Trans. A*, **9A**, 1497 (1978).
7. K.C. Anthony, *Trans. TMS-AIME*, **242**, 1454 (1968).
8. Y.Z. Lu and S.H. Whang, 1983 AIME Fall meeting, Oct. 2-6, Philadelphia, PA.
9. G. Sauthhoff and M. Kahlweit, *Acta Metall.*, **17**, 1501 (1969).
10. A.J. Ardell, *Acta Met.*, **20**, 61 (1972).
11. A.D. Brailsford and P. Wymblait, *Acta Metall.*, **27**, 489 (1979).
12. M. Doner and H. Conrad, *Met. Trans.*, **4**, 2809 (1975).
13. T.P. Papazoglu and M.T. Hepworth, *Trans. TMS-AIME*, **242**, 698 (1968).
14. G.R. Purdy, *Met. Sci. J1*, **5**, 81 (1971).
15. P.K. Footner and C.B. Alcock, *Met. Trans.*, **3**, 2633 (1972).
16. A.J. Ardell, *Acta Metall.*, **15**, 1772 (1967).
17. F.A. Shunk, *Constitution of Binary Alloys*, Second Supplement, McGraw-Hill Book Co., 682 (1969).

$\times 10^{-13}$ cm²/sec for 700°C and 1.9×10^{-11} cm²/sec for 800°C [12]. In fact, the Si diffusion coefficients fall between the self diffusion coefficient of α -Ti and the diffusion coefficient of carbon in α -Ti (7.9×10^{-10} cm²/sec for 700°C [13]), but are closer to the self-diffusion coefficient.

Further, the interfacial free energy between the dispersoid and the matrix was assumed here to be 1.0 J/m^2 since the reported interfacial free energies for incoherent particles range from 0.5 J/m^2 [14] to 1.5 J/m^2 [15]. Thus, the uncertainty in the diffusion coefficients due to the choice of the interfacial energy value are not assumed to exceed 100%. One way to check the interfacial free energy would be to measure the time variation of the average concentration of solute in the matrix [16].

Last, the possible effect of the refined subgrain structure on the coarsening mechanism is considered. For example, in the annealed alloy (700°C, 4h), the grain size and the calculated center-to-center particle distance are $\sim 0.5 \mu\text{m}$ and $\sim 0.05 \mu\text{m}$, respectively. Hence, the average grain diameter is ten times larger than the particle spacing. This situation is significantly different from the one where the particle spacing and the grain diameter are of the same order and where, therefore, the grain boundary coarsening mechanism comes into operation. It therefore appears that grain boundary diffusion is not large enough to affect the overall coarsening rate.

In order to improve the general understanding of the particle coarsening kinetics in this system, the following experiments would be worthwhile:

- 1) particle size distribution as a function of the volume fraction of precipitate and
 - 2) the diffusivities at more than two temperatures to obtain activation energies.
- SUMMARY**
- (1) Ostwald ripening of silicide in Ti follows the volume diffusion model by SEW in the temperature range of 700-800°C.
 - (2) the diffusivities of Si in Ti obtained in the range of 700-800°C are an order of magnitude larger than the corresponding self-diffusivity of Ti.
 - (3) the measured cut-off value of ~ 1.7 in z/r is in agreement with the value predicted by the SEA model.
 - (4) microstructural refinement had no effect on the coarsening kinetics in this temperature range.

ACKNOWLEDGEMENT

The authors gratefully acknowledge support of this work by the Office of Naval Research (Contract N00014-82-K-0597).

REFERENCES

1. I.M. Lifshitz and V.V. Slyozov, *J. Phys. Chem. Solids*, **19**, 35 (1961).
2. C. Wagner, *Z. Elektrochem.*, **65**, 581 (1961).
3. S.H. Whang, *J. Metals (AIME)*, Vol. 36, No. 4 (1984).
4. C.S. Chi and S.H. Whang, See proceedings of this symposium.

MICROSTRUCTURAL CHARACTERISTICS OF RAPIDLY QUENCHED

alpha-Ti ALLOYS CONTAINING LA

C.S. Chi and S.H. Whang

Submitted to Met. Trans. A. Dec., 1984

Barnett Institute, Materials Science Division,
Northeastern University, Boston, MA 02115

MICROSTRUCTURAL CHARACTERISTICS OF RAPIDLY QUENCHED α -Ti ALLOYS CONTAINING La

C.S. Chi and S.H. Whang

Rapidly quenched Ti-La alloys show that the maximum extended solubility of La in Ti at the cooling rate of $\sim 10^6$ K/sec is ~ 0.3 at. %. An excess amount of La (> 0.3 at. %) deposits in the form of clusters (< 50 Å diameter) along the subgrain boundary. Grain refinement resulting from rapid quenching is effectively aided by alloying elements (Al, Sn), but no apparent effect, however, on grain refinements by La was found. Fine precipitates in Ti-5Al-3La alloy were identified as a mixture of binary La compounds: Al_4La (Hex., DO_{19}) and Al_3La (Orth., DI_3) while those in Ti-5Sn-3La alloy appeared to be La_2Sn (Hex., B8_2). So far, no ternary compound has been identified in these alloy systems. An EELS study clearly shows that the precipitates of these alloys treated in a high vacuum contain La, Al and Sn, but not Ti. Various substructures resulting from rapid quenching often remain in the matrix even after high temperature annealing, probably due to the pinning by fine precipitates. These precipitates appear to be stable and coarsening resistant at high temperatures. Strong age hardening accompanied by fine dispersoids exists in the Ti alloys containing Al (or Sn) and La. Microhardnesses of the alloy ribbons annealed isothermally or isochronally are systematically lower than those of splat quenched foils, consistent with coarser precipitates of alloy ribbon.

I. INTRODUCTION

The development of high temperature Ti alloys through precipitation or dispersion hardening dates back more than two decades. Since then,

strengthening of Ti alloy matrix has been achieved by a small addition of such compound forming elements as rare earth metals (Ce, La, Gd, etc.) [1-4], actinide (Th) [4] and metalloids (Si, B, C) [4, 5, 6]. Of these additives, Si, has been systematically incorporated into Ti alloys through conventional ingot casting and subsequent solution treatment to yield fine silicide precipitates, since the maximum solid solubility of Si in β -Ti reaches at a maximum of ~5 at. % at 1300°C. These silicide hardened alloys show good creep resistance at or near 500°C, due to thermally stable precipitates at these temperatures [7]. Nevertheless, the coarsening rate of silicide particles in the Ti-matrix at or above 700°C significantly high, resulting in a major loss in the strength gained by the Orowan mechanism [8].

In contrast, rare earth metals have a solid solubility range of less or equal to 1 at. %, even at high temperatures. As a result, not only is an adequate solution treatment within the solubility range not possible, but also a larger addition of these elements than 1 at % results in coarse particles, ranging from one to several microns in diameter through conventional ingot casting [4]. Therefore, in some earlier works, it was reported that the addition of rare earth metals did not produce an increase in strength [2], but did improve creep strength [4] and creep rupture time [3].

One recent method of more effectively producing dispersion strengthening of Ti alloy is through rapid solidification processing, through which significant amounts of rare earth elements are dissolved into solid solution or precipitate uniform clusters in the matrix. The succeeding heat-treatment results in fine rare earth dispersoids in the matrix. Such dispersoids in Ti-5Sn-4.5La alloy [9] demonstrate that they are far more coarsening resistant

electro-polishing contains perchloric acid 4%, 2-butoxyethanol 35% and methanol 61%. The polishing was carried out at a voltage range of 20 V and a current of less than 12 mA/cm². The annealed samples containing coarse particles were thinned by electropolishing followed by the ion mill technique. In order to study the structure of dispersoids in RS Ti alloys, carbon extraction replicas were prepared from the annealed samples containing coarse particles. Microstructure was studied by a Philips EM300, a JOEL 100CX and a vacuum generator HB5 field emission STEM with EELS and EDXS capabilities. The structure of dispersoids was determined by diffraction ring patterns while, the composition was confirmed mainly by EELS and EDX studies. Microhardness was measured on heat treated samples by a Vickers diamond pyramid tester with 50 and 100 g loads.

III. RESULTS

A. Extended Solid Solubility

Extended solubility of solutes by rapid liquid quenching is a well-known phenomenon. During rapid solidification, phase separation and phase formation are restricted within one per hundred thousand second ($\sim 10^6$ k/sec) so that excess solutes are trapped in the matrix. Therefore, the degree of supersaturation in rapid liquid quenching ($\sim 10^6$ deg/sec) far exceeds that in the equilibrium phase. The resulting effects include solid solubility increase, lattice parameter change, strength increase and microstructural refinement. Table 1 shows that in general, the extended solid solubility is much larger than the equilibrium solubility at room temperature where the equilibrium solid solubility of the solutes becomes very small. In particular, upon rapid quenching, the increase in solubility is large in phase diagrams with a terminal eutectic, i.e., Ti-metalloid systems (C, B, Si) with eutectic show a large extended solubility. From a structural point of view, solid solution may be a substitutional type (Si) or an interstitial type (C), and at least in part

Microstructures of Ti-5Al-3La alloy may be better understood by studying microstructures of binary alloys: Ti-5Al and Ti-3La (Figs. 1a and 1b). The addition of Al to Ti results in grain refinement and twin structure during rapid quenching. In contrast, grain refinement is less apparent and no twin structure can be observed in the Ti-3La system. Instead, very fine clusters of La are dispersed in the matrix. The microstructures of as-quenched Ti-5Al-3La alloy appear to be a combination of these two binary microstructures, as shown in Fig. 1c, i.e., a strong grain refinement with uniform clusters. The excess La beyond the extended solid solubility (Table 1) deposits preferentially along sub-grain boundaries (Fig. 1b). When the alloy is heat treated at 700°C, 2h, precipitate coarsening initially occurs along the sub-grain boundary (Fig. 2). In particular, large particles are observed at the triple junctions of high angle grain boundary. After the Ti-5Al-3La alloy was annealed at 700°C, 1h (Fig. 3a), an EELS study of the precipitates (Fig. 3b) showed very high La concentrations in the precipitate while no apparent oxygen peak was detected in these spectra. In contrast, those spectra from the matrix consist of a strong Ti peak with the absence of La peak (Fig. 3c).

Since oxygen levels in both the precipitate and the matrix are not distinct, no comparison between the two levels can not be made based on the spectra alone. Further, the precipitates isolated by the extraction replica technique (Figure 4a) yield the diffraction patterns in Fig. 4b. Listed in Table 2 are those d spacings of the ring patterns, Al_4La (Orth., D_{13}) and Al_3La (Hex., D_{019}). Other d spacings from La_2O_3 , TiO_2 , $\text{Ti}_2\text{O}_3 \cdot 0.03$, $\text{Al}_{12}\text{La}_{0.88}$ (FCC), Al_2La and pure La were checked against the obtained d spacings and no similarity found between them. Neither the diffraction patterns of Al_3La nor those of Al_4La alone can satisfy all the experimental data. However, the d spacings of both Al_4La and Al_3La together match the experimental results.

d spacings of LaSn_3 (Cu_3Au), Ti-Sn binary compounds, La_2O_3 , TiO_2 and found to disagree with them. EELS of a precipitate in the Ti-9.5Sn-5.3La alloy exhibits a strong La peak and a weak Ti peaks which probably comes from the background (Fig. 9b). Another spectrum of the matrix (Fig. 9c) shows a strong Ti peak, but no La peak can be identified. In both figures, the intensities of oxygen and Sn peaks cannot be evaluated, since the intensities appear to overlap with Ti peak intensity.

Microstructures of as-quenched alloy ribbons of 50 μm were studied by TEM after the ribbon specimens were thinned by mechanical polishing and later the ion mill technique. A micrograph of the alloy ribbon (Fig.10) shows relatively coarse precipitates (average ~50nm diameter) within large grains without substructures. This indicates that the low cooling rate is responsible for such coarse microstructures.

c) Ti-5Al-2.5Sn-3La and Ti-5Al-2.5Sn-4Zr-3La alloys.

These alloy systems are made of conventional α -Ti alloys and La addition. Microstructural characteristics of as-quenched Ti-5Al-2.5Sn-3La alloy are predictably similar to those of ternary alloy systems, Ti-Al-La or Ti-Sn-La. These similarities include the formation of La origin cluster and the degree of grain refinement. Although grain refinement in the Ti-5Al-2.5Sn-3La alloy is more extensive than in the ternary alloys (Fig. 11a). Diffraction patterns of the Ti-5Al-2.5Sn-3La alloy indicate that no compound exists at the as-quenched state. (Fig. 11b). Upon aging, uniform precipitates start to emerge in the matrix while slight coarse precipitates already appear along grain boundary (Figure 12a). As a result, the diffraction patterns (Fig. 12b) exhibit new ring patterns which do not belong to Ti, presumably resulting from the precipitates or dispersoids. After high temperature annealing of this alloy at 900°C, 2h, particle coarsening accompanied by substructure disappearance

(Cu₃Au), Ti-Sn binary compounds, La₂O₃, TiO₂ and found to disagree with them. EELS of a precipitate in the Ti-9.5Sn-5.3La alloy exhibits a strong La peak and a weak Ti peaks which probably comes from the background (Fig. 9b). Another spectrum of the matrix (Fig. 9c) shows a strong Ti peak, but no La peak can be identified. In both figures, the intensities of oxygen and Sn peaks cannot be evaluated, since the intensities appear to overlap with Ti peak intensity.

Microstructures of as-quenched alloy ribbons of 50μm were studied by TEM after the ribbon specimens were thinned by mechanical polishing and later the ion mill technique. A micrograph of the alloy ribbon (Fig.10) shows relatively coarse precipitates (average ~50nm diameter) within large grains without substructures. This indicates that the low cooling rate is responsible for such coarse microstructures.

c) Ti-5Al-2.5Sn-3La and Ti-5Al-2.5Sn-4Zr-3La alloys.

These alloy systems are made of conventional α-Ti alloys and La addition. Microstructural characteristics of as-quenched Ti-5Al-2.5Sn-3La alloy are predictably similar to those of ternary alloy systems, Ti-Al-La or Ti-Sn-La. These similarities include the formation of La origin cluster and the degree of grain refinement. Although grain refinement in the Ti-5Al-2.5Sn-3La alloy is more extensive than in the ternary alloys (Fig. 11a). Diffraction patterns of the Ti-5Al-2.5Sn-3La alloy indicate that no compound exists at the as-quenched state. (Fig. 11b). Upon aging, uniform precipitates start to emerge in the matrix while slight coarse precipitates already appear along grain boundary (Figure 12a). As a result, the diffraction patterns (Fig. 12b) exhibit new ring patterns which do not belong to Ti, presumably resulting from the precipitates or dispersoids. After high temperature annealing of this alloy at 900°C, 2h, particle coarsening accompanied by substructure disappearance occurs in some grains, whereas in other grains, fine precipitates and

the calculated Nusselt number shows that splat quenching covers over a cooling range from the Newtonian to the intermediate regimes. Presently, no direct measurement of cooling rate for Ti alloy ribbons or splat foils is available. Nevertheless, the estimation of the cooling rate for Ti-6.3Si alloy is possible, using the measured heat transfer coefficient [31] at the interface between the molten alloy and the cold copper crucible. From a one dimensional heat flow relation, the cooling rate at the liquid state may be written as

$$\frac{dT}{dt} = \frac{h \cdot \Delta T}{d \cdot \rho \cdot C_p}$$

Where $\Delta T = (T_i - T_s)$, T_i , T_s are superheat temperature and substrate temperature; ρ , C_p and d are density, heat capacity, and half thickness of splat foil, respectively. The calculated cooling rate for Ti-6.3Si shown in Table 4 is an order of magnitude smaller than those values measured by other authors (Table 4). On the other hand, two dimensional models with the aid of computer calculations yield systematically lower cooling rates, e.g., $3.2-6.4 \times 10^5$ °C/sec for Fe-25Ni splat of 40µm thick (d) [29] and $\sim 10^5-10^6$ °C/sec for Ta-45 at. %Ir, Nb-45 at. %Rh and Cu-34 at. %Zr [30]. It is important to note that the outcome of the cooling rate calculations depends significantly on what value of the heat transfer coefficient is being used among the large selections available. Therefore, it is not reasonable to compare these cooling rate values to each other without checking into the heat transfer values employed. It is interesting to note, however, that the Nusselt numbers from our present work and the work of Predecki et al are close to Newtonian cooling whereas Harbur et al have found numbers large enough to fall into the intermediate cooling regime. Such discrepancies may be rationalized by the fact that in the former two experiments, the melt was not quenched under the high pressure

temperature. Nevertheless, kinetic conditions such as kinetic undercooling and interface attachment kinetics may allow only certain compositions to undergo partitionless solidification below T_0 [38]. From these arguments, alloy compositions near the eutectic, where high undercooling can be achieved through rapid quenching, are expected to show high extended solubility. By contrast, monotectic compositions of Ti-rare earth metal systems are expected to lead to lean solid solution, since the magnitude of reduced undercooling for the critical cooling may be too large to achieve in these systems [22]. Table 1 demonstrates that a large solubility extension is achieved in eutectic systems, whereas little extension is possible in monotectic systems.

Another phenomenological approach by fundamental parameters may be considered in the following. The solubility ratio (between the extended and the maximum equilibrium solid solubility, α -phase) calculated from Table 1 is listed in Table 4 together with atomic size ratio and electronegativity of additive elements. These data were plotted in Fig. 16a and b. Both Figures indicate that the solubility extension is correlated with atomic size and electronegativity. Since the pioneer works by Hume-Rothery and his coworkers have demonstrated that the solubility of solutes is governed by atomic size ratio and relative valence electron value [39], many other parameters such as electronegativity [40], heat solution [41,42] have been employed to predict the solubility of solutes in equilibrium alloy systems using a two-dimensional map. These electronic parameters are basically related to each other, but more effective prediction has been made by a combination of heat of formation and atomic size for a two dimensional map [42]. A similar approach has been successfully applied to quenched alloy systems: ion implanted alloys [43] and RS Al alloys [44]. Such success in RS alloys indicates that the parameters used for the equilibrium alloy systems are equally effective in solubility

1. At the cooling rate of $\sim 10^6$ deg/sec, a large solubility extension of additives is observed in the eutectic type alloy systems whereas a small extension is noted in the monotectic type alloy systems. This phenomenon may be analyzed with fundamental parameters such as atomic size, heat of mixing, and electronegativity.
2. Ternary alloy Ti-5Al-3La yields uniform precipitates (average size ~ 200 Å dia.) upon aging at 700°C under high vacuum. These precipitates, prepared by the extraction replica technique, were identified from the diffraction ring patterns as a mixture of particles of Al₃La (Hex., DO₁₉) and Al₄La (Orth., DI₃).
3. Precipitates of annealed Ti-9.5Sn-5.3La alloy (800°C) yield diffraction ring patterns similar to those of La₂Sn (Hex., B8₂).
4. No rare earth oxide was identified from the diffraction ring pattern in the aged Ti-5Al-3Al and Ti-9.5Sn-5.3La alloys. This indicates that the oxide formation under vacuum is insignificant compared to non-oxide formation.
5. Coarser precipitates were found in the as-quenched ribbon of Ti-5Al-2.5Sn-3La alloy, in comparison with fine precipitates of splat foil with the same thickness. This indicates that the average cooling rate of the spun ribbon appears much lower than that of the splat foil ($\sim 10^6$ deg/sec). The cause of the lower cooling appears to originate in the poor contact between the melt and the substrate, as evidenced by air pockets and wetting patterns.

ACKNOWLEDGEMENT

The authors gratefully acknowledge the support of the Office of Naval Research for this work (Contract N00014-82-K-0597). In particular, we thank Dr. Donald E. Polk for his thoughtful suggestion for rapidly solidified Ti alloy research at Northeastern University. Contribution No. 202 from the Barnett Institute of Chemical Analysis and Materials Science.

REFERENCES

1. E.J. Chapin and R. Liss, Report of NRL Program, December 1955.
2. B. Love, WADC Tech. Report, No. TR57-666, Part II, March 1959.
3. N.J. Grant, U.S. Patent 3,070,468, 1962.
4. M.B. Vordahl, U.S. Patent 3,622,406, 1971.
5. K.C. Antone, Trans. AIME, 1968, Vol. 242, pp.1454-1456.
6. H.M. Flower, P.R. Swann and D.R.F. West, Met. Trans., 1971, Vol. 2, p.3289.
7. N.W. Paton and M.W. Mahoney, Met. Trans. A, 1976, Vol. 7A, p.1685.
8. S.H. Whang, Y.Z. Lu and B.C. Giessen, Mat. Res. Soc. Sym. Proc. 1984, Vol. 28, 367-373.
9. Y.Z. Lu, C.S. Chi and S.H. Whang, Proc. 5th Int. Conf. Rapidly Solidified Metals, Sept. 2-7, 1984, Würzburg, W. Germany, in press.
10. B.B. Rath, et al., Proc. Fourth Int. Conf. on Titanium, H. Kimura and O. Izumi, eds, AIME, N.Y., N.Y., 1980, pp. 1185-1196.
11. S.M.L. Sastry, T.C. Peng, P.J. Meschter and J.E. O'Neil, Journal of Metals, Vol. 35, No. 9 (1983) pp. 21-28.
12. S.H. Whang, Journal of Metals, 1984, Vol. 36, No. 4, pp.34-40.

33. B.P. Bardes and M.C. Flemmings, "Modern Castings," 1966, Vol. 50, pp.100-106.
34. W.W. Mullins and R.F. Sekerka, J. Appl. Phys., 1964, Vol.35, p.444
35. S.R. Coriell and R.F. Sekerka, Rapid Solidification Processing II, R. Mehrabian, et al eds, Claitor's Baton Rouge, LA 1980.
36. S.P. Midson and H. Jones, Proc 4th Int. Conf. Rap. Que. Met. Sendai, 1981 pp. 1539-1544.
37. M. Cohen, B.H. Kear and R. Mehrbrian, Rapid Solidification Processing II, R. Mehrabian, et al, eds, Claifor's Baton Rouge, LA 1980, pp. 1-23.
38. W.J. Boettinger, Proc. MRS Sym. Vol. 8, B.H. Kear, B.C. Giessen, M. Cohen eds, 1982, pp. 15-31.
39. W. Hume-Rothery, G.W. Mabbott and K.M. Channel-Evans, Phil. Trans. R. Soc., Ser. A, London 1934, Vol. 233, pp. 1-97.
40. Darken-Gurrey, "Physical Chemistry of Metals," McGraw-Hill, New York 1952 pp.86-90.
41. S.R. Chelikowsky, phys. Rev. B, 1979, Vol. 19, pp.686-701.
42. J.A. Alonso and S. Simozar, Phy. Rev. B, 1980, Vol. 22, pp.5583-5589.
43. D.K. Sood, phys Lett., 1978, Vol. 68A, pp.469-472.
44. H. Jones, Proc. Mat. Res. Soc., 1984, Vol. 28.
45. L.E. Marr: "Electron and Ion Microscopy and Microanalysis, 1982," Marcel Dekker, Inc., pp.78-187.

| | | | | | | |
|-------|---|--------|----|--------------|----|--------------|
| | | | | 1.840 | 16 | [232 105 |
| | | 1.8001 | 10 | 202 | | |
| 1.774 | M | 1.774 | 2 | 301 | | |
| | | | | 1.687 | 16 | [233 163 |
| | | | | 1.668 | 6 | 204 |
| | | 1.664 | 16 | 220 | | |
| | | | | 1.657 | 4 | 064 |
| | | 1.584 | 10 | 212 | | |
| | | 1.511 | 20 | 311 | | |
| 1.467 | W | 1.480 | 16 | [103 302 | | |
| | | 1.442 | 4 | 400 | | |
| | | 1.376 | 10 | 401 | | |
| 1.342 | W | 1.353 | 30 | [203 222 | | |

TABLE 4: Calculated cooling rate for Ti-6.3Si compared with those reported in other metals.

| alloy | Half thickness of splat foil (d) cm | Thermal conductivity (k) W/cm-K | Heat Transfer Coefficient W/cm ² -K | Nusselt number | Cooling rate* (20μm thick) °C/sec | Substate materials used | Technique used |
|----------|-------------------------------------|---------------------------------|--|----------------|-----------------------------------|-------------------------|----------------|
| Ti-6.3Si | 2.0x10 ⁻³ | 0.218 (pure Ti) | 0.6 | 0.0027 | 3.3x10 ⁵ | Cu & Cu | Hammer & Anvil |
| Al | 7.0x10 ⁻³ | 2.20 | 18.4 | 0.06 | (4.8x10 ⁶) [26] | Fe & Al | Plate & Plate |
| Pb | 8.8x10 ⁻³ | 0.33 | 20.9 | 0.26 | (5.3x10 ⁶) [26] | Fe & Al | Plate |
| Al | 1.0x10 ⁻⁴ | 0.28 | 11.3-28.8 | 0.00051-0.0013 | (1.5-3x10 ⁶) [25] | Ni/Ag | Coupled |
| Ag | | 4.29 | 56.9-226 | 0.0013-0.0053 | (1-5x10 ⁷) [25] | Ni/Ag | Substrate |

*The cooling rates are adjusted based on 20μm thick foil by using the relation of inverse proportionality of cooling rate to the thickness.

Nusselt Number = $(h \cdot d)/k$

TABLE 5: Atomic Size Ratio vs. Relative Solubility Increase

Due to Rapid Quenching

| Alloy System | Solubility Ratio (Ex. S.S./M.Eq.S.S. (α)) | Wigner-Seitz Atomic Radius Ratio (R_s/R_{Ti}) |
|--------------|---|---|
| Ti-C | ~18 | 0.68 |
| -B | ~14 | 0.75 |
| -Si | ~ 9 | 1.04 |
| -Y | ~ 5 | 1.23 |
| -Ce | ~0.6 | 1.25 |
| -La | ~0.3 | 1.28 |

Annealed Ti-5Al-2.5Sn-3La alloy foil (700°C, 2h)

- Fig. 13**

Annealed Ti-5Al-2.5Sn-3La alloy foil (900°C, 2h)

Ti-5Al-2.5Sn-4Zr-3La alloy foil

- Fig. 15**

**Microhardness of alloys: Ti-5Al-2.5Sn-3La
and Ti-5Al-4Zr-2.5Sn-3La**

- Fig. 16a**

[Extended solid solubility/maximum equilibrium solid solubility] vs. [Solute atomic radius/Ti atom radius]

[Extended solid solubility/maximum equilibrium solid solubility] vs. Electronegativity

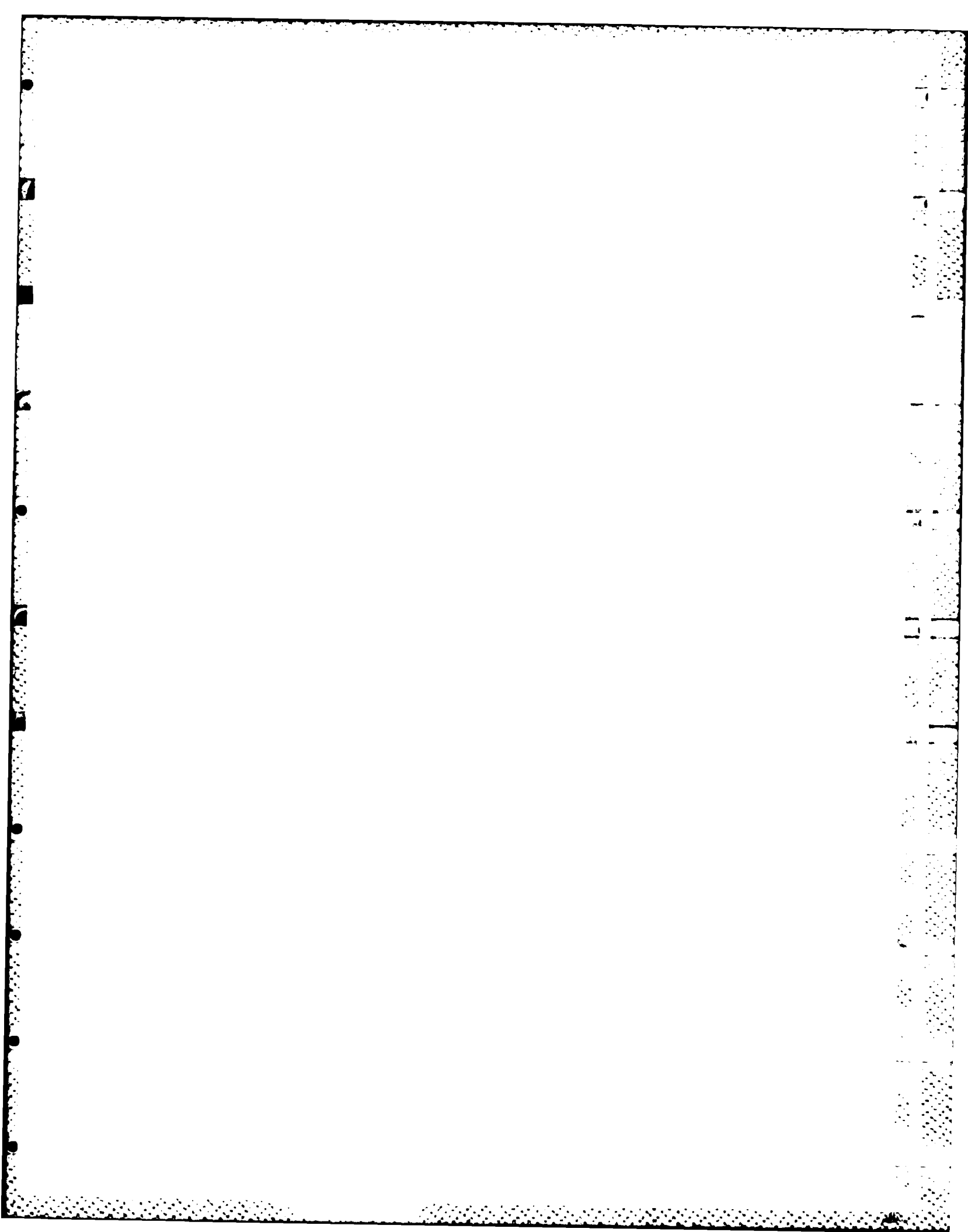




Fig. 1a As-quenched Ti-5Al alloy foil (B.F.)



Fig. 1b As-quenched Ti-3La alloy foil (B.F.)



Fig. 1c As-quenched Ti-5Al-3La alloy foil (B.F.)

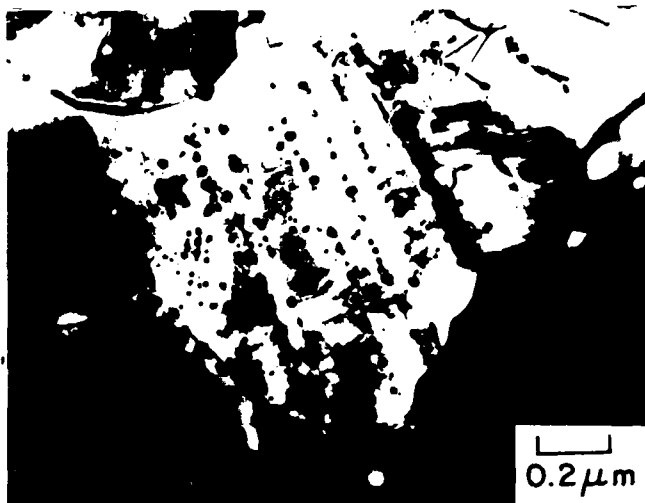


Fig. 2 Annealed Ti-5Al-3La alloy foil (700°C, 2h; B.F.)

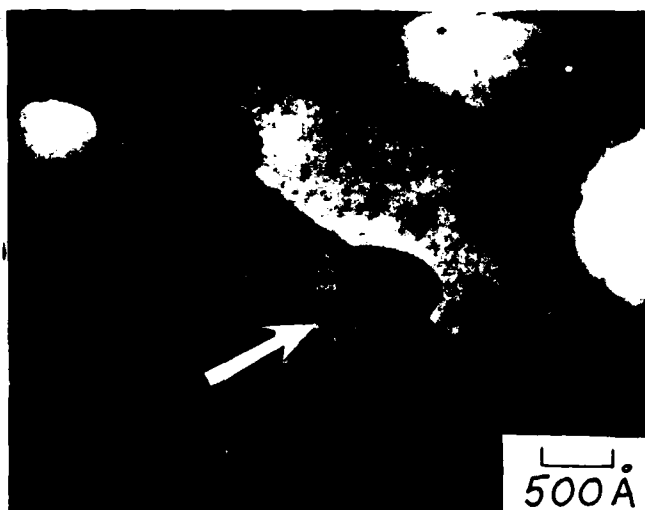


Fig. 3 Annealed Ti-5Al-3La alloy foil (700°C, 1h)

a) precipitates at the low angle grain boundary

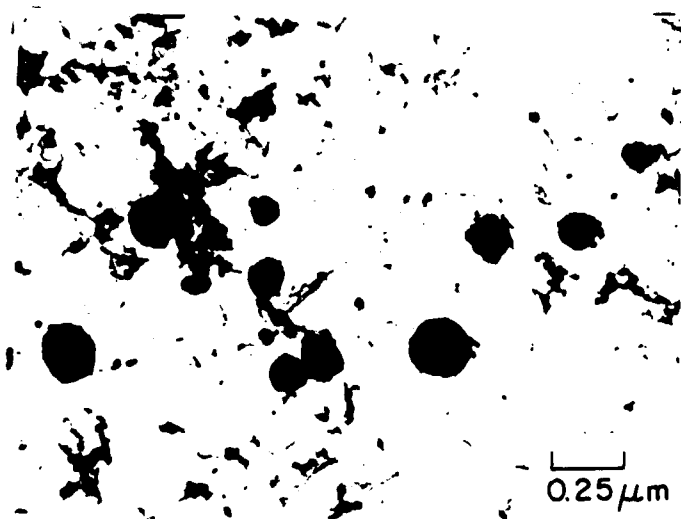


Fig. 4 Particles obtained from annealed Ti-5Al-3La alloy (900°C; 1h)

a) bright field

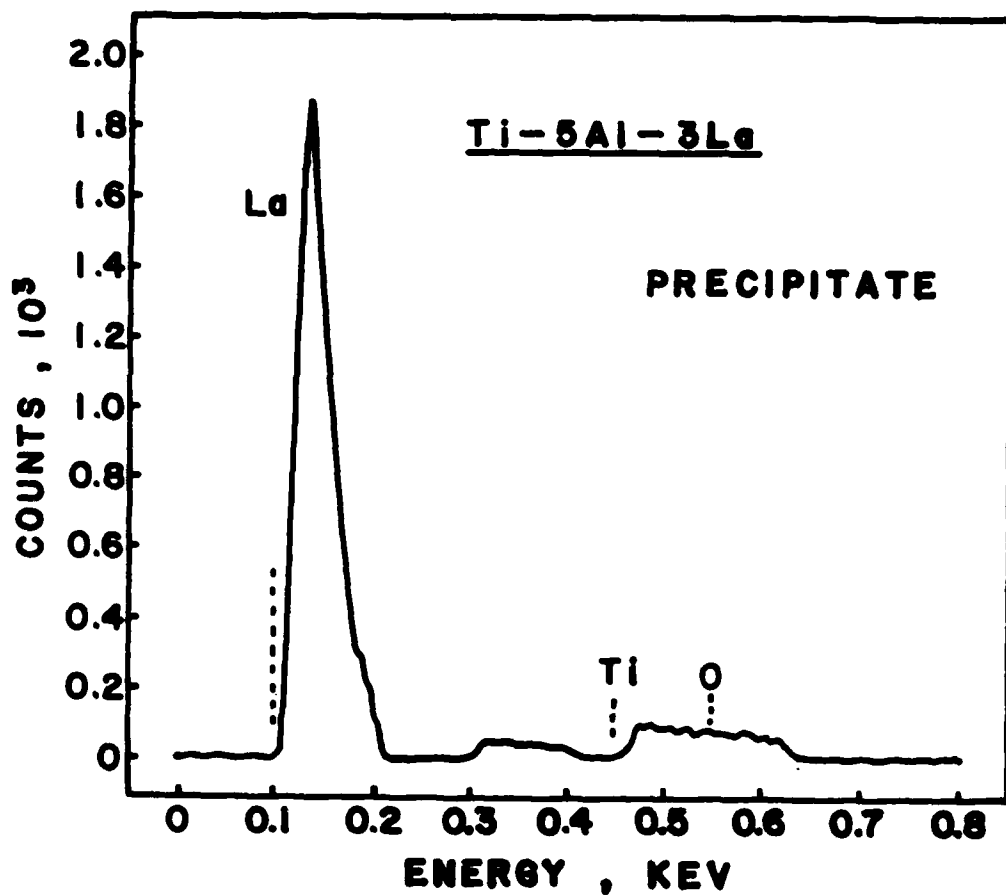


Fig. 3b) EELS of a precipitate
(arrow sign)

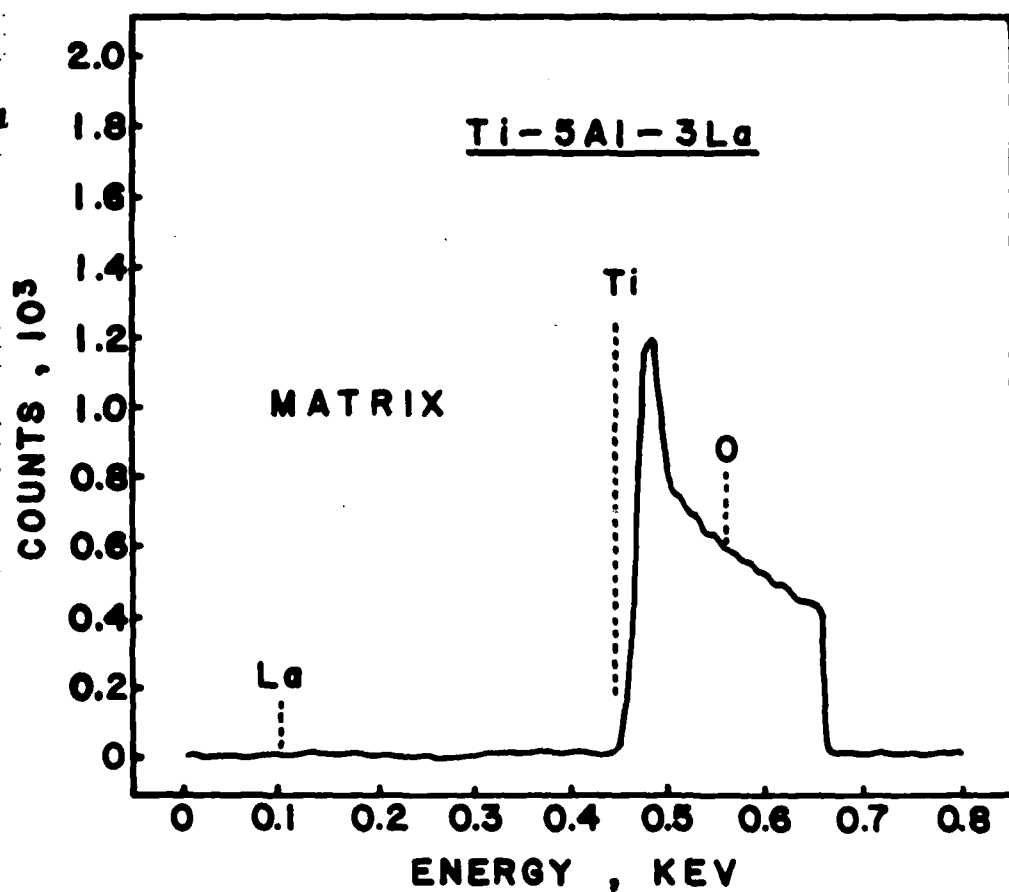


Figure 3c
EELS of the matrix near the
precipitate



Fig.4 b) diffraction pattern

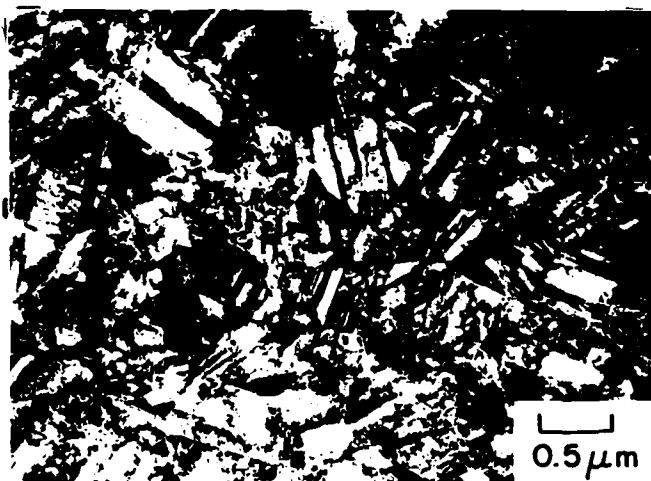


Fig. 5 As-quenched Ti-9.5Sn alloy foil

a) bright field

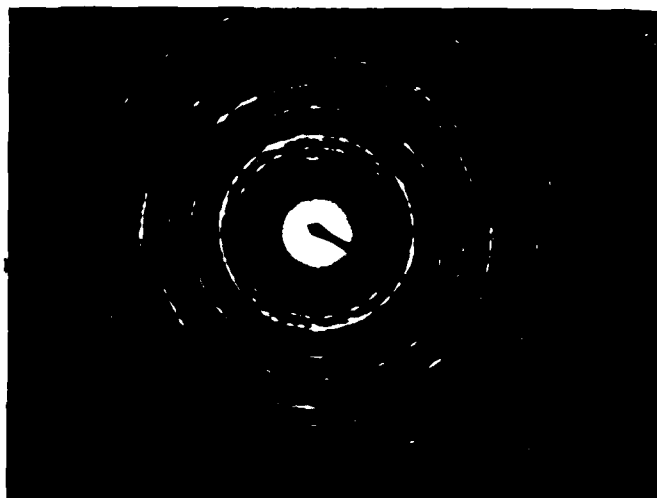


Figure 5b

diffraction pattern

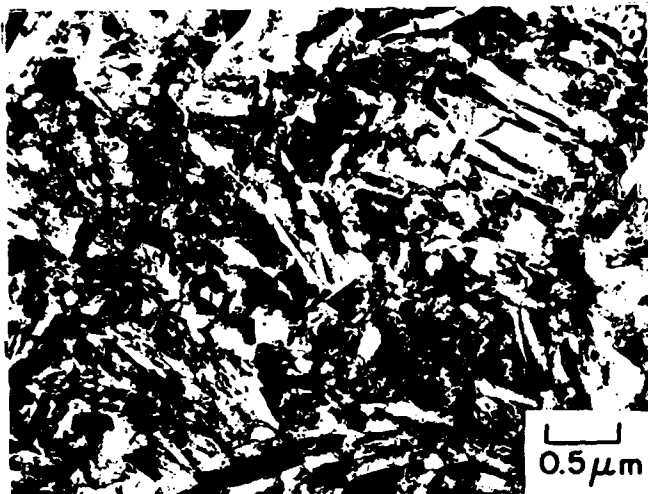


Fig. 6 Annealed Ti-9.5 Sn-5.3
La foil alloy

a) bright field

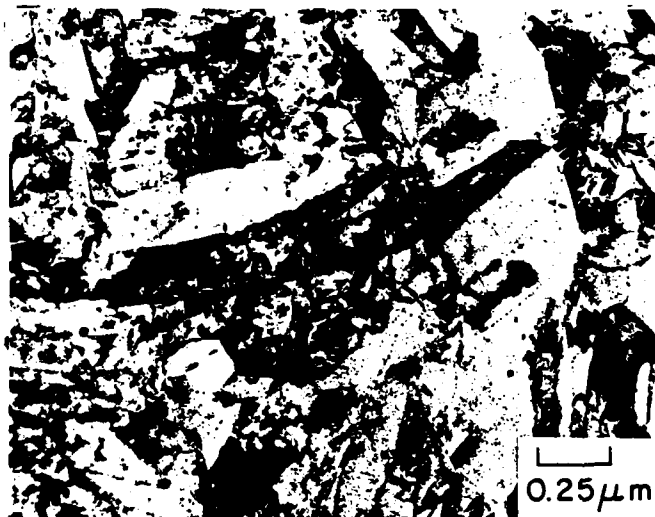


Figure 6b

higher magnification of a)



Fig. 7 Annealed Ti-5Sn-3La alloy
foil (700°C, 2h)

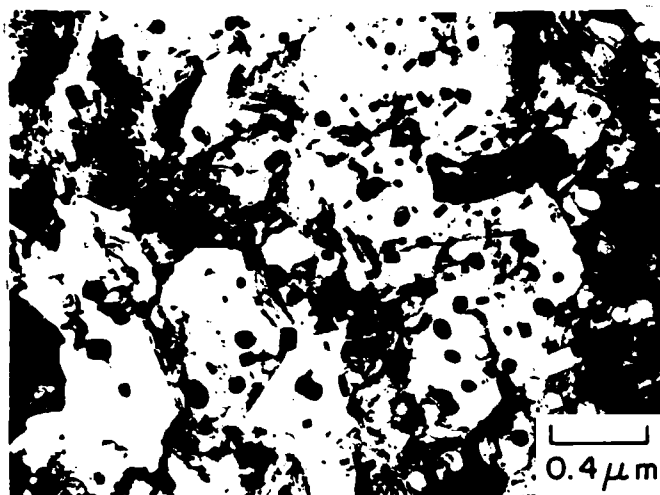


Fig. 8 Annealed Ti-9.5Sn-5.3 La alloy foil (850°C , 1h)

a) Bright field

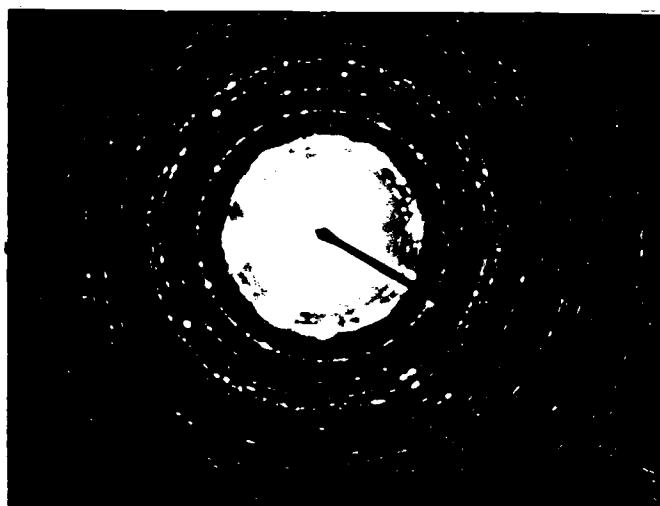


Fig. 8b) Diffraction pattern



Fig. 9 Annealed Ti-5Sn-4.5La alloy foil (800°C , 10h)

a) bright field

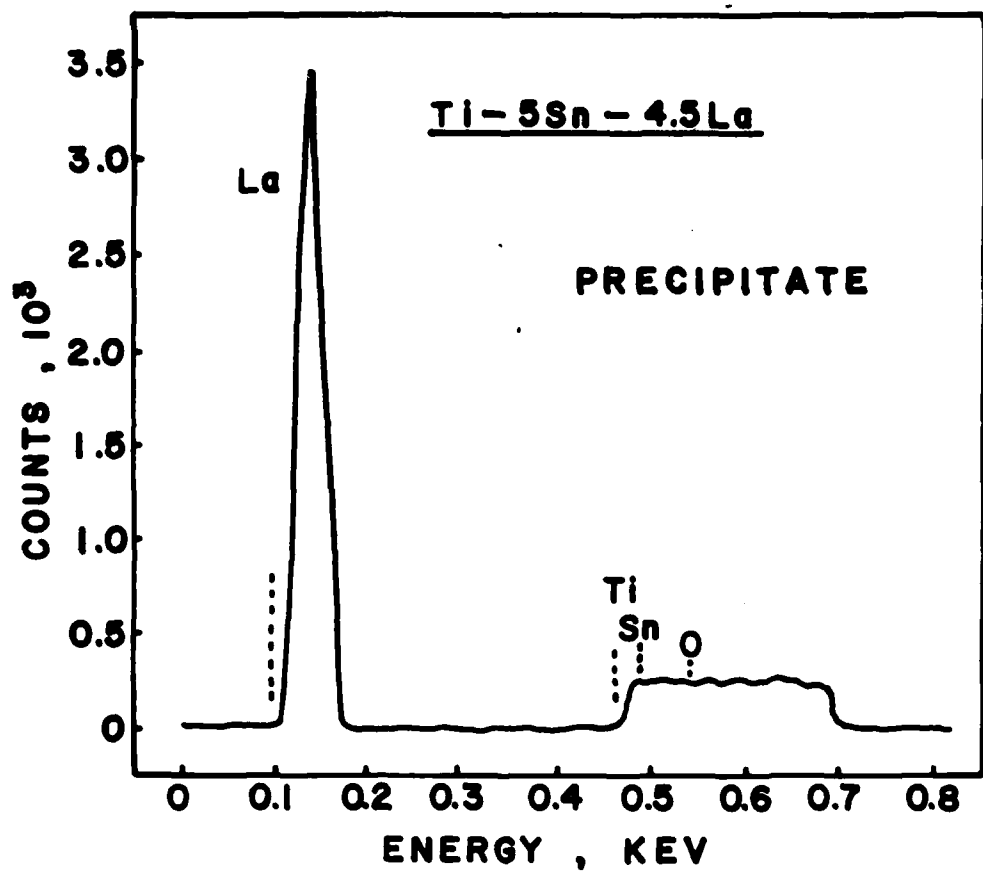


Figure 9b

EELS from the precipitate
(arrow sign)

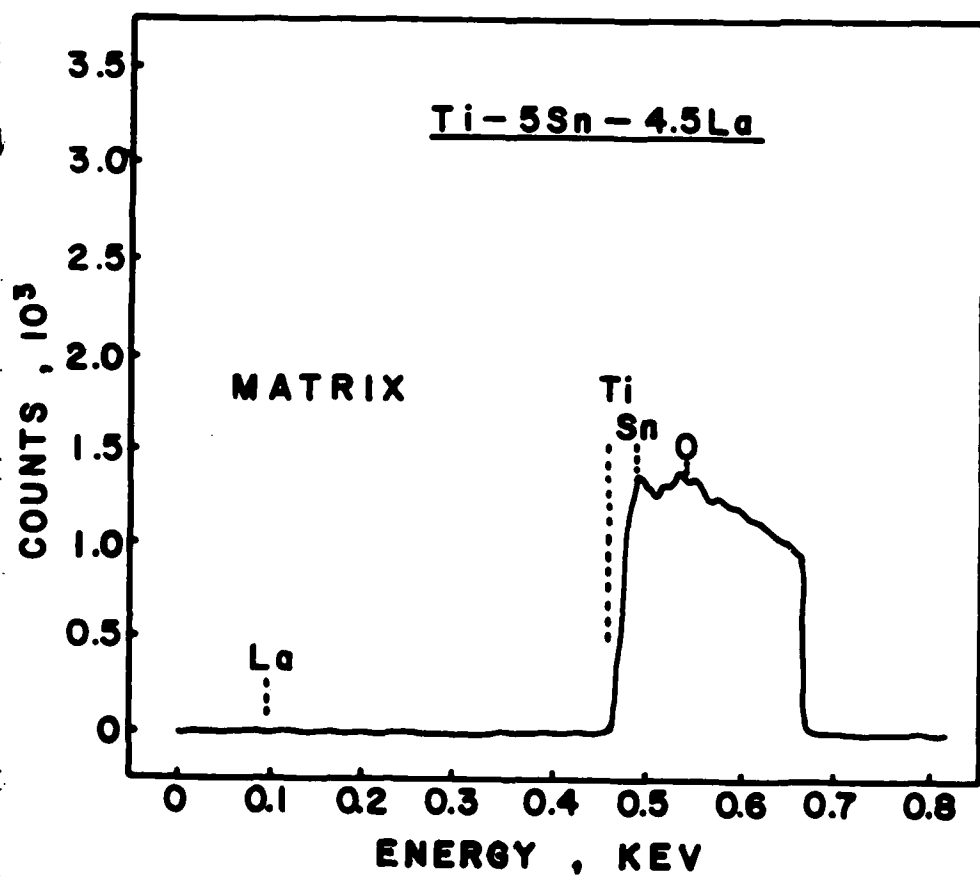


Figure 9c

EELS from the matrix

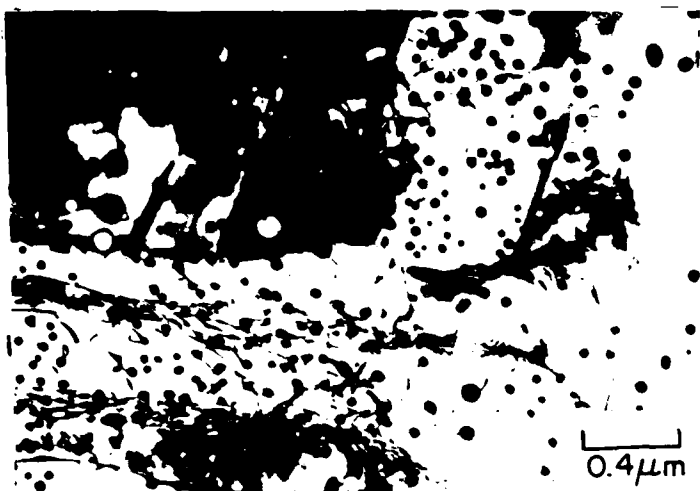


Fig. 10 As-quenched Ti-5Sn-4.5La alloy ribbon (50 μm thick)



Fig. 11 As-quenched Ti-5Al-2.5Sn-3La alloy foil

a) bright field



Figure 11b
diffraction pattern

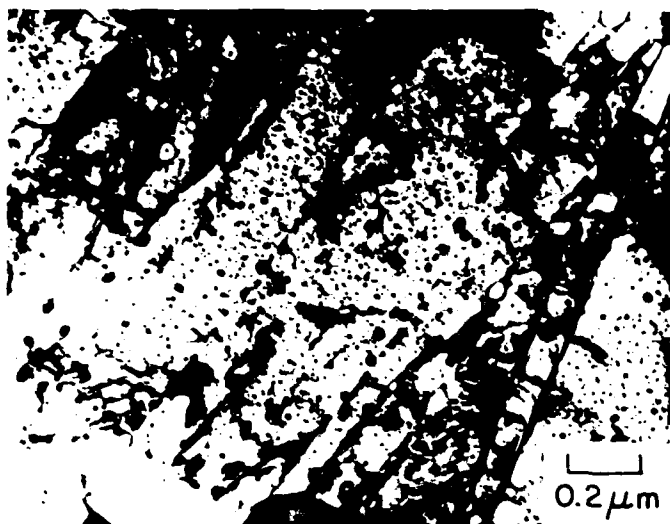


Fig. 12 Annealed Ti-5Al-2.5Sn-3La
alloy foil (700°C, 2h)

a) bright field



Figure 12b
diffraction pattern

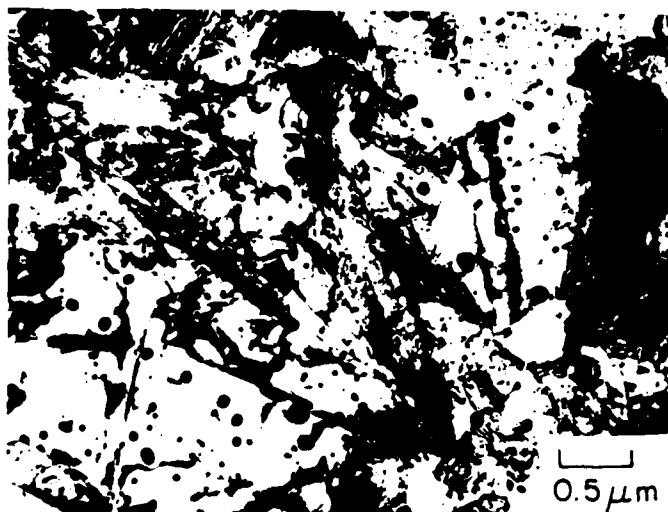


Fig. 13 Annealed Ti-5Al-2.5Sn-3La
alloy foil (900°C, 2h)



Fig. 14 Ti-5Al-2.5Sn-3La alloy foil

a) As-quenched state

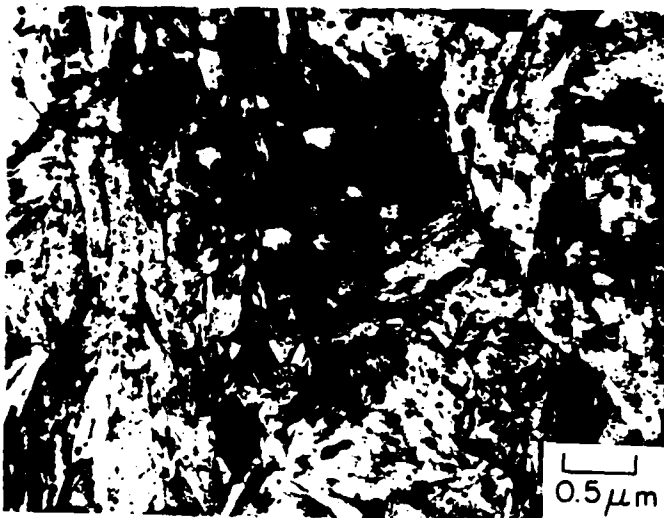


Figure 14

b) Annealed at 900°C, 2h

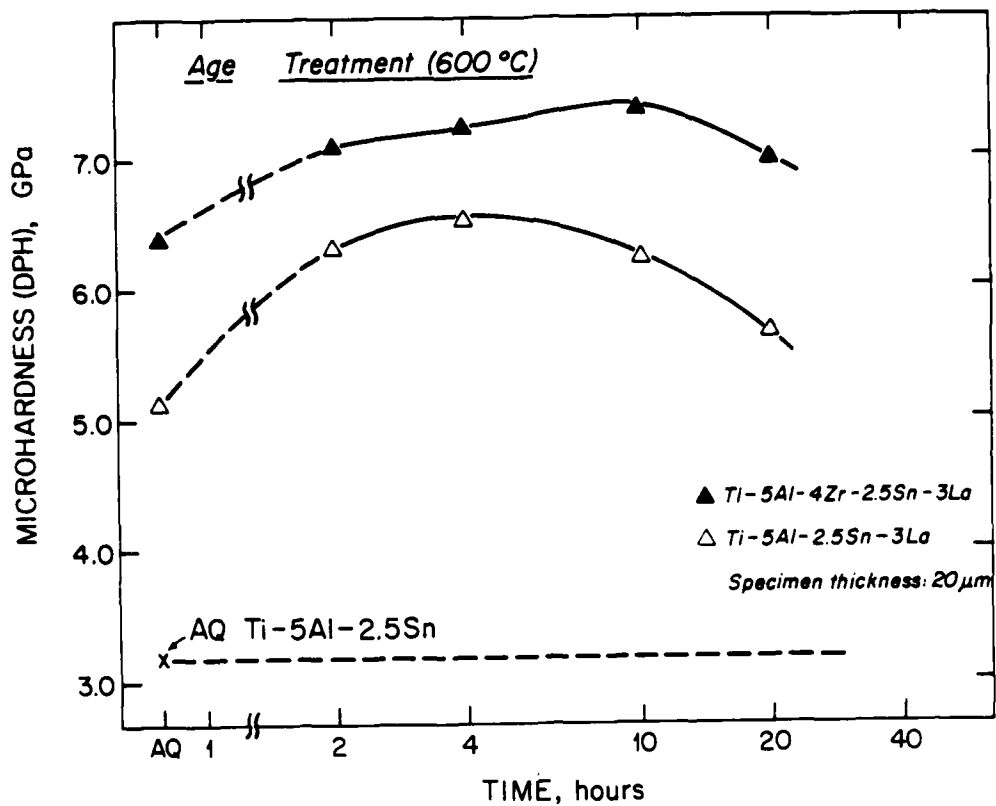


Fig. 15 Microhardness of alloys: Ti-5Al-2.5Sn-3La and Ti-5Al-4Zr-2.5Sn-3La a) Isothermal annealing at 600°C

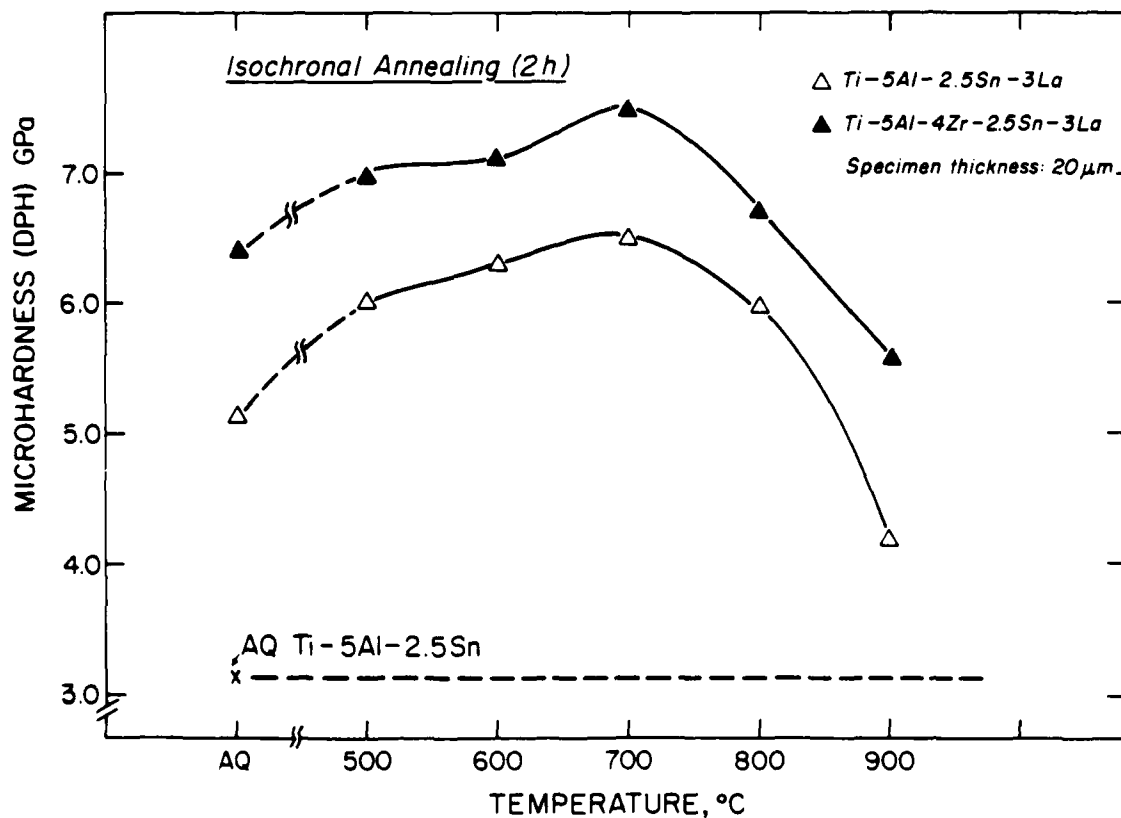


Figure 15

b) Isochronal annealing from 500°C to 900°C for 2h

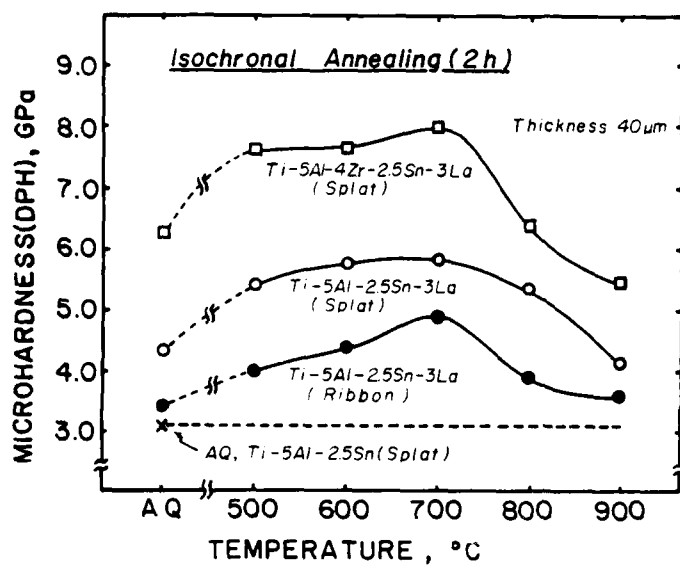


Figure 15

c) Comparison between splat foil and spun ribbon often isochromal annealing

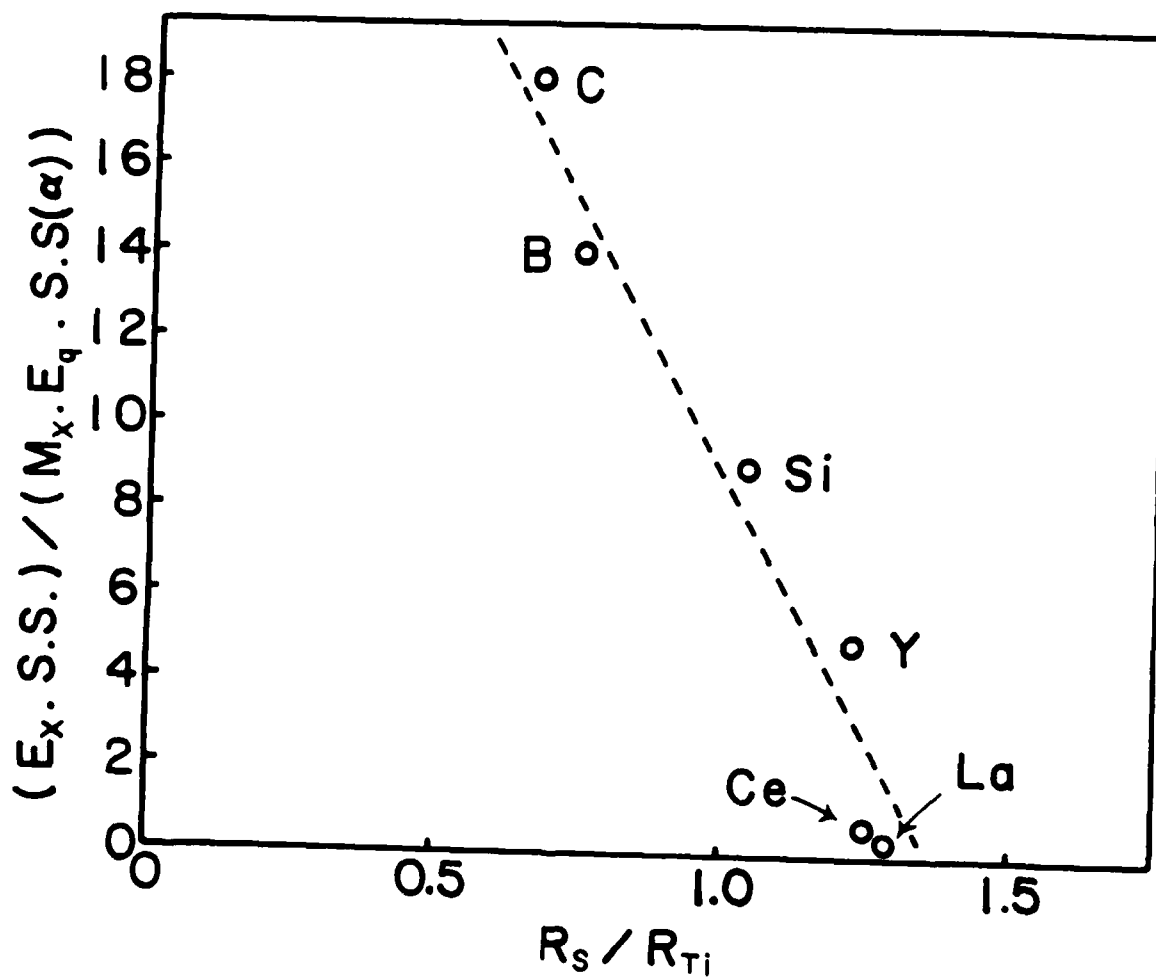


Fig. 16a [Extended solid solubility/
maximum equilibrium solid solubility]
vs. [Solute atomic radius/Ti atom
radius]

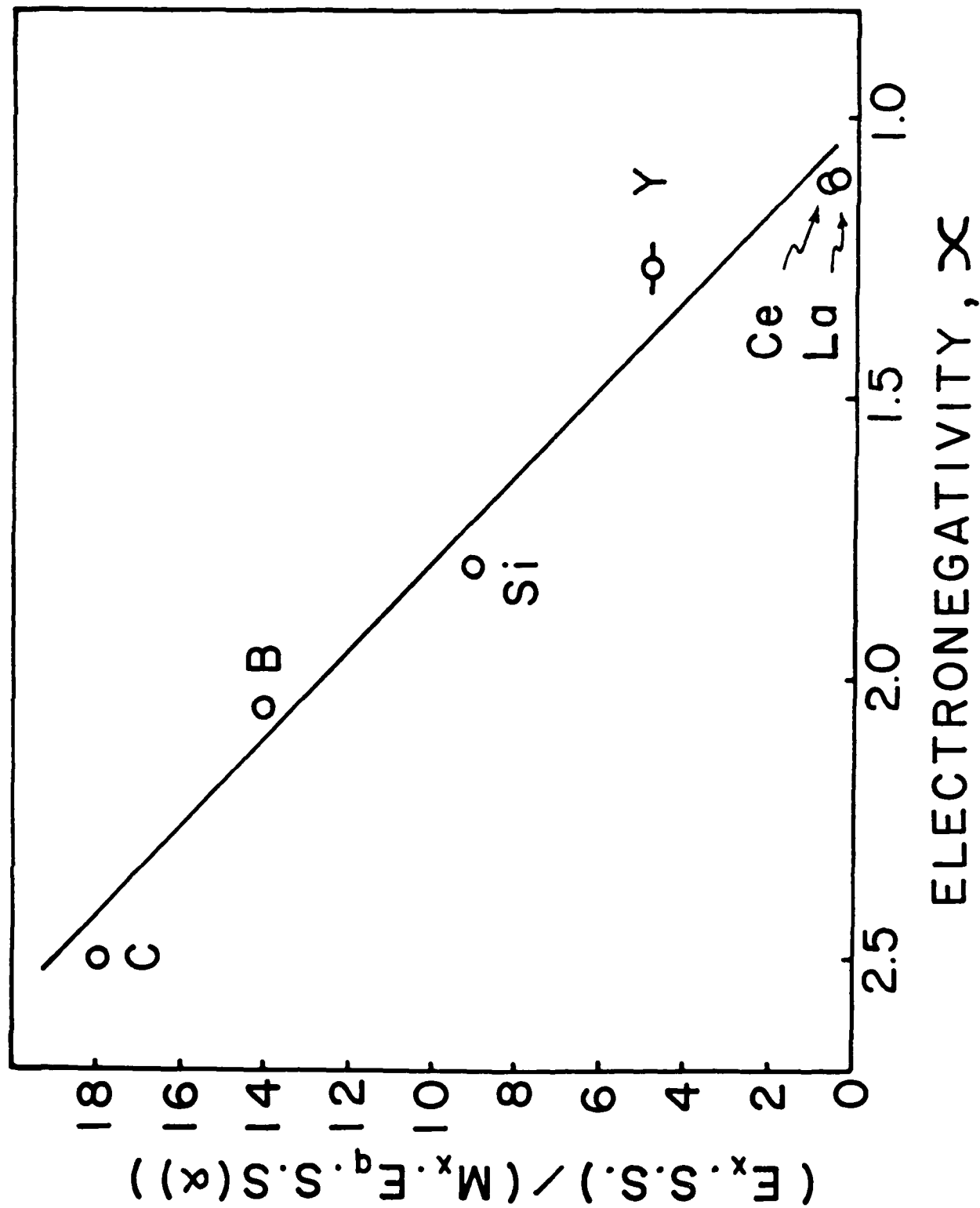


Fig. 16b [Extended solid solubility/
maximum equilibrium solid solubility]
vs. electronegativity

SECOND PHASE COARSENING IN Ti-5Sn-4.5La SYSTEM

Y.Z. Lu, C.S. Chi, and S.H. Whang

Proc. Fifth Int. Conf. Rapidly Quenched Metals,
Sept. 3-7, Wurzburg, W. Germany, the proceedings in press.

SECOND PHASE COARSENING IN RAPIDLY SOLIDIFIED Ti-5Sn-4.5La SYSTEM

Y.Z. LU, C.S. CHI and S.H. WHANG

Barnett Institute of Chemical Analysis and Materials Science, Northeastern University,
Boston, MA 02115, USA

Ostwald ripening of rare earth dispersoids in rapidly solidified Ti-5Sn-4.5La alloy was studied by TEM at 800°C (α -phase). The results show that 1) coarsening mechanism is basically governed by lattice diffusion 2) slow coarsening of these dispersoids is attributed to low diffusivity of La in α -Ti; $\sim 4 \times 10^{-14}$ cm²/sec at 800°C.

1. INTRODUCTION

The recent developments of rapidly solidified (RS) α -Ti alloys with high specific strength and good high temperature properties demonstrates that the alloy matrix is systematically strengthened by various novel dispersoids. These dispersoids consist of oxide and non-oxide compounds of metalloids or rare earth metals, created uniformly from the supersaturated matrix via heat treatment. In these dispersion strengthened alloys, the stability of the dispersoids at elevated temperatures becomes a critical parameter for high temperature mechanical properties. A previous study of particle coarsening in Ti-5Al-2Si alloy has shown that high diffusivity of Si is responsible for a strong propensity to second phase coarsening in this alloy [2].

Similarly, qualitative observation of particle coarsening in RS Ti alloys containing carbon or boron shows that the similar rapid coarsening of precipitates has been identified [1,3]. In contrast, in Ti-Al(Sn)-La alloy systems, microstructural study reveals that La dispersoids are coarsening resistant during high temperature annealing [4]. However, so far, no systematic study has been made of particle

coarsening kinetics for these rare earth dispersoids in Ti.

In this paper, we report on a preliminary study of Ostwald ripening of La₂Sn dispersoids [4] in Ti-5Sn-4.5 La Alloy at 800°C.

2. EXPERIMENTS

In order to prepare uniform foil alloys, the same quench conditions were applied during hammer and anvil quenching. Disk specimens of $20 \pm 5 \mu\text{m}$ were obtained from the middle section of the foils. For heat treatments the disks were sealed in quartz tubes under vacuum (10^{-3} torr) and annealed at desired temperatures and durations. The particle distributions of the annealed specimens were studied by TEM and image analyzer. The coarsening study was carried out using 400-600 particles for each data point. The precipitate volume is determined from the TEM micrographs using an approximate relation [5].

3. RESULTS AND DISCUSSIONS

Microstructural characteristics of the as-quenched alloy may be largely divided into two categories: 1) microstructural refinements due to high cooling rate, $\sim 10^6$ deg/sec, including acicular shaped grains

and fine twin-like structures; 2) uniform clusters of La in the matrix. When La concentration exceeds the solubility limit ~ 0.3 at %, the excess La deposits in the form of clusters. The cluster size is less than 50 Å diameter, as shown in Figure 1. These as-quenched microstructures disappear rapidly during high temperature annealing (800°C). Instead, new microstructures consisting of equiaxed grains and uniform precipitates replace the as-quenched ones (Figure 2). During annealing, the precipitates retain their spherical shape as they grow into coarse particles. The size distribution as a function of reduced particle radius remains constant throughout the entire annealing period. After trial and error, it was found that a linear correlation was obtained from the plot of the 3rd power of average particle radius (\bar{r}) vs. annealing time (t) (Figure 3). Therefore, the diffusivity of the solute concerned may be estimated using LSW equation [6,7]. According to LSW,

$$\bar{r}^3 - \bar{r}_0^3 = \frac{8}{9} \cdot \frac{K \cdot C_s(\infty) \cdot D \cdot \gamma \cdot V_m}{R \cdot T} (t - t_0)$$

\bar{r}_0, \bar{r} = average particle radii for the onset and final states

K = volume fraction factor

$C_s(\infty)$ = equilibrium solubility of solute in the matrix with particles of infinite size at a given temperature T

D = diffusion coefficient of solute, cm^2/sec

γ = interfacial free energy of particle, J/m^2

V_m = gram-molar volume of precipitate, $\text{cm}^3/\text{g-mole}$

t_0, t = onset and final annealing time, sec

R = gas constant, $\text{J}/\text{mole-K}$

T = absolute annealing temperature, K.

This equation contains an additional factor K to the original LSW equation [8,9]. The volume fraction factor K for the present

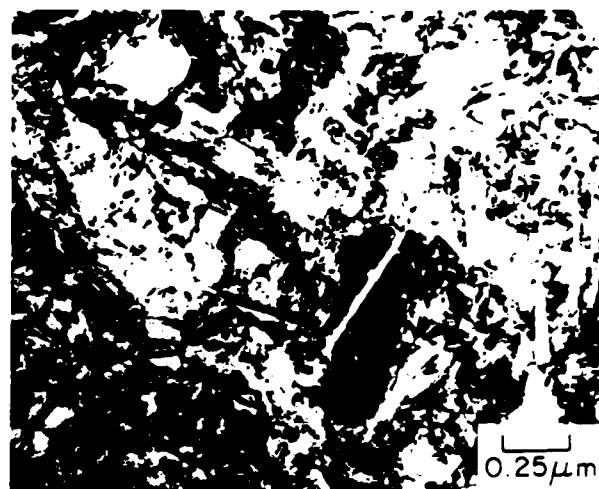


FIGURE 1
Bright field micrograph of as-quenched Ti-5Sn-4.5La foil alloy.

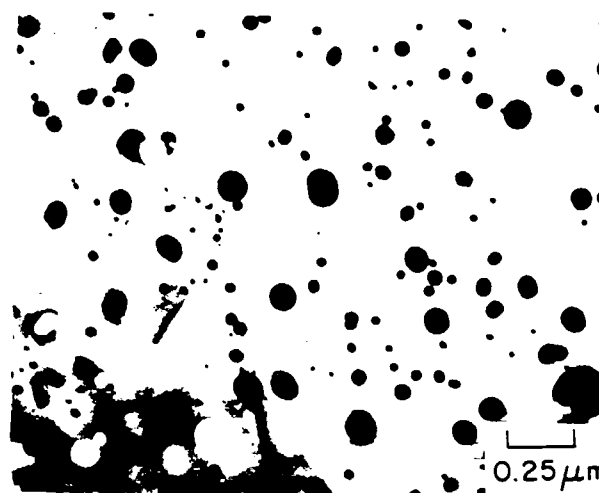


FIGURE 2
The annealed alloy of Fig. 1 at 800°C, 60h.

calculations was obtained from one of the models [8]. Interfacial free energy of the precipitates (La_2Sn) is arbitrarily assumed as $1 \text{ J}/\text{m}^2$, which is an intermediate value among the reported values for incoherent precipitates. In fact, interfacial free energy of precipitates can be determined with reasonable accuracy from an LSW

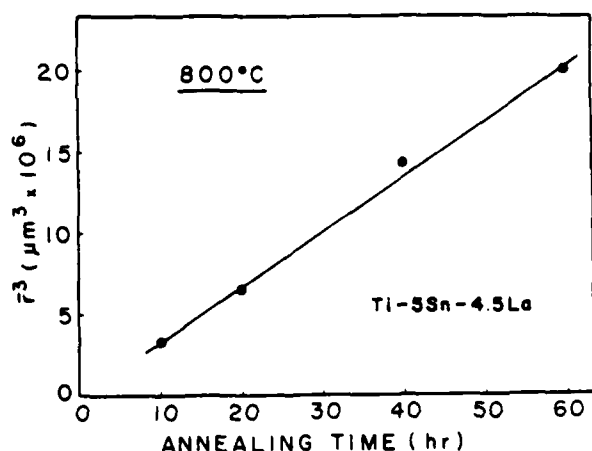


FIGURE 3

Plot of the cube of the average particle radius vs. annealing time.

equation, provided the accurate diffusion coefficient of the solute is known. Alternatively, interfacial free energy may be obtained by measuring the solid solubility of the solute as a function of annealing time [10]. Unfortunately, the former approach is outside of the current experimental context and the latter is not feasible technically. Using these given values, the diffusion coefficient of the solute was calculated from the modified LSW equation as listed in Table 1. The obtained diffusion coefficient is two orders of magnitude smaller than the corresponding diffusivity of Ti at 800°C. The diffusion coefficient is believed to represent that of La. The reason for that is as follows: First of all, the lattice diffusion for Ostwald ripening of the dispersoids involves

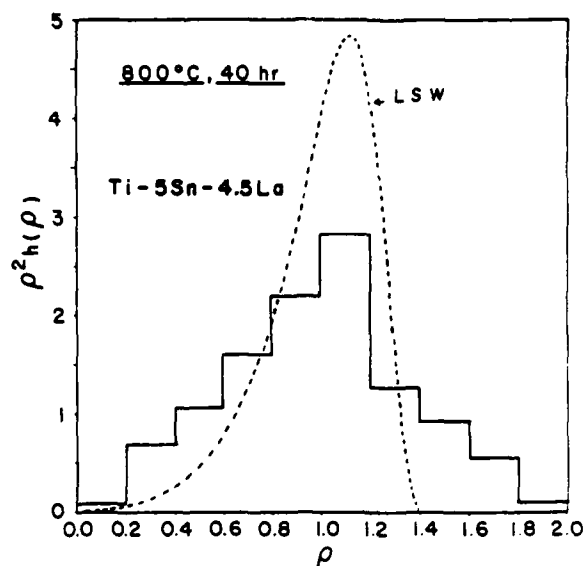


FIGURE 4

Plot of particle size distribution function vs. reduced particle radius.

two solutes, La and Sn, from the constitution of the precipitate (La_2Sn). Of these two solutes, Sn has almost identical diffusivity with that of Ti in β -Ti [12]. Hence, it is difficult to theorize that the diffusivity of Sn becomes suddenly two orders of magnitude smaller than that of Ti in α -Ti. Nevertheless, it is clear that these calculations involve significant error, perhaps because of multiplying effects between arbitrary interfacial free energy value, precipitate volume fraction factor and some uncertainty in equilibrium solubility measurement.

When size distribution function $\rho^2 h(\rho)$ was plotted against reduced particle radius

Table 1: Diffusion Coefficient of La in Ti-5Sn-4.5La

| Temperature °K | Slope in the $\bar{r}^3 - t$ plot (m^3/sec) | Total vol. fraction of precipitate (%) | K [8] | $C_s(\infty)$ [11] | V_m ($m^3/g-mole$) | D (La) (cm^2/sec) |
|-------------------|--|---|-------|--------------------|---------------------------|--------------------------|
| 1073 | 9.39×10^{-29} | 1.4 | 2.35 | ~ 0.0046 | 2.33×10^{-5} | 3.7×10^{-14} |

(ρ), apparent deviation from the LSW model was noted, i.e., the maximum value of ρ in these experiments is ~ 2.0 in comparison with 1.5 for the LSW model (Figure 4) and the predicted value 1.75 [8]. In fact, volume effects on the ripening were not well understood.

4 CONCLUSIONS

1. Particle coarsening in Ti-5Sn-4.5La alloy at a high temperature is controlled by the volume diffusion mechanism.
2. The slow coarsening rate of La_2Sn dispersoids is governed by low diffusivity of La in α -Ti. This fact is contrasted to the high diffusivity of metalloids and the high coarsening rate of metalloid dispersoids in α -Ti.
3. A significant deviation of particle size distribution from the LSW model is identified in Ti-5Sn-4.5La alloy.

ACKNOWLEDGEMENT

The authors would like to thank the support of the Office of Naval Research, VA (Contract No N00014-82-K-0597). Contribution # 231 from the Barnett Institute.

REFERENCES

1. S.H. Whang, J. Metals, 36 (1984) 34.
2. S.H. Whang, Y.Z. Lu and B.C. Giessen, Proc. Materials Research Society Meeting, Nov. 1983, Boston, vol. 8, in press.
3. C.S. Chi and S.H. Whang, Proc. Materials Research Society Meeting, Nov., 1983, Boston, Vol. 8, in press.
4. C.S. Chi and S.H. Whang, unpublished work.
5. E.E. Underwood, Quantitative stereology, (Addison-Wesley, 1970) 148.

6. I.M. Lifshitz and V.V. Slyozov, J. Phys. Chem. Solids, 19 (1961) 35.
7. C. Wagner, Z. Elektrochem, 65(1961) 581.
8. A.J. Ardell, Acta Met., 20 (1972) 61.
9. A.D. Brailsford and P. Wynblatt, Acta Metall., 27 (1979) 489.
10. A.J. Ardell, Acta Metall, 15 (1967) 1772.
11. E.M. Savitsku and G.S. Burkhanov, J. Less-Common Metals, 4 (1962) 301.
12. J. Askill and G.B. Gibbs, Phys. Status Solidi, 11 (1965) 557.

PILOT SCALE-ARC PLASMA MELT SPINNING PROCESS
FOR Ti RICH ALLOYS

S.H. Whang, C.S. Chi, and Y.Z. Lu

Proc. Fifth Int. Conf. Rapidly Quenched Metals,
Sept. 3-7, 1984, Wurzburg, W. Germany, the proceedings in press.

PILOT SCALE ARC MELT SPINNING FOR TI RICH ALLOYS

S.H. WHANG, C.S. CHI AND Y.Z. LU

Barnett Institute of Chemical Analysis and Materials Science, Northeastern University, Boston, MA 02115, U.S.A.

For pilot arc melt spinning of Ti alloys, thermal behavior of the melt during arc heating has been studied with respect to arcing conditions. Based on 1 dim. steady state heat flow analysis, the results suggest that Ti alloy melting requires a large superheat and a steep temperature gradient while intermediate cooling is characteristic at the alloy-crucible interface in the temperature range of 1200-1400°C. Some ribbon and flake Ti alloys were spun by the pilot arc melt spinning unit.

1. INTRODUCTION

Much past and current research [1-4] suggests that rapidly solidified Ti alloys with novel additives have distinct potential for developing high specific strength and good high temperature properties. In order to stimulate further research in this direction, more flexible processing techniques are essential. Although many rapid solidification processing techniques for Ti alloys have been developed [5-7], the arc melt spinning technique has many advantages over other techniques with respect to contamination-free processing, high quench rate, and inexpensive operation. In this technique, a cold copper crucible with an orifice, combined with a non-consumable arc electrode for melting and spinning, is employed. This scheme was, for the first time, applied to Ti alloys on a lab-scale [8]. However, some concerns about extensive freeze at the alloy-crucible interface and effectiveness of high intensity argon arc as a heat source have been raised. Therefore, it is necessary to investigate thermal behavior of the melt with respect to heating conditions and heat flow profiles at the steady state. This paper presents a preliminary study of such behavior of Ti alloy

and some results of melt spinning experiments using this unit.

2. EXPERIMENTS

Current experiments have been carried out using a pilot-scale arc melt spinning unit at Northeastern University. Fig. 1 shows the front view of this unit. This unit is also equipped for other processing parameters controls such as arc power, inert gas pressure, disk speed, electrode rotation speed and granule alloy feed rate. The detailed descriptions of this unit are given elsewhere [3]. In order to study thermal behavior of Ti-6.3Si alloy button in the cold copper crucible, a thermocouple (Pt-13Rh) and an optical pyrometer (Iacon 2000 series) were employed to monitor the temperatures of the top and the bottom surfaces. The alloy button has an ellipsoidal shape ($a=b=3\text{cm}$, $c=1.3\text{cm}$) weighing 50 g. A non-consumable tungsten electrode was placed above the button with a distance (L) of 1 cm and Ar pressure of 37 Kpa. Temperature readings as a function of current (100, 200, 300, 400, 500 A) have been made at a location between the center and the edge of the surfaces when the steady state heat flow conditions have been established.

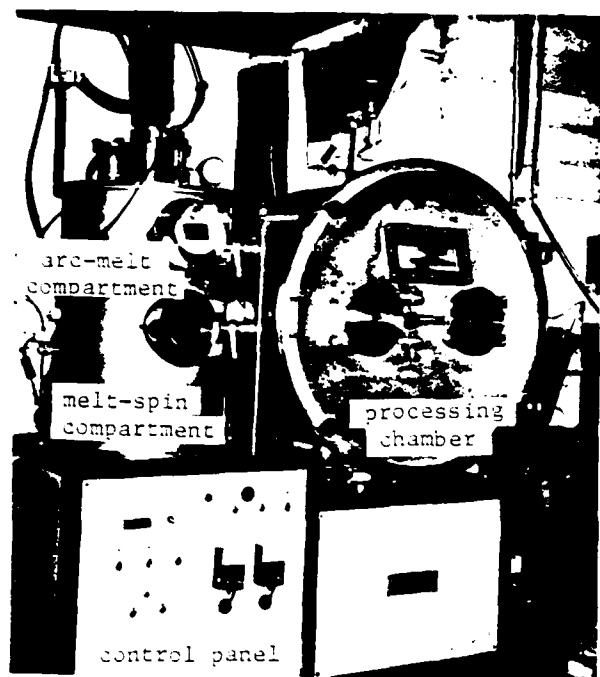


FIGURE 1
Front view of pilot arc melt spinning unit.

3. RESULTS AND DISCUSSIONS

The temperatures of the alloy button were measured by increasing nominal input power (Fig. 2). The temperature of the top surface increases rapidly in a non-linear manner, whereas the temperature of the bottom surface increases very slowly in a more or less linear fashion. As a result a large temperature gradient along the c axis, parallel to the incoming arc plasma, has developed as shown in Fig. 3. When the surface temperature (T_s) was plotted against the square-root of the total current (I) (Fig. 4), an empirical relation was found from the linear correlation

$$T_s = a + b \sqrt{I} \quad (1)$$

where a and b are temperature intercept and conversion factor.

In order to understand the situation more clearly, a schematic drawing is given in Fig. 5. By assuming that the heat flow only occurs along the c axis or in the direction parallel to the incoming arc plasma, the solidification front moves toward the alloy-crucible interface

by increasing superheat and total current. At the interface, the heat transfer is limited by the high interface resistance while at the top surface, very large superheat occurs, due to the poor conductivity of this alloy. Since the thermal conductivity (k) of Ti-6.3Si alloy is

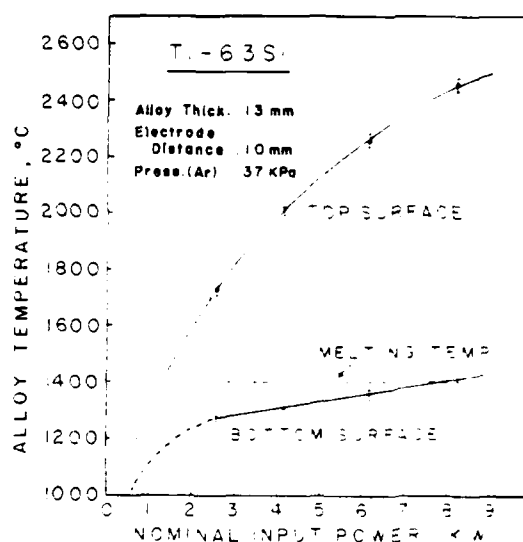


FIGURE 2
Plot of alloy temperature vs. nominal input power.

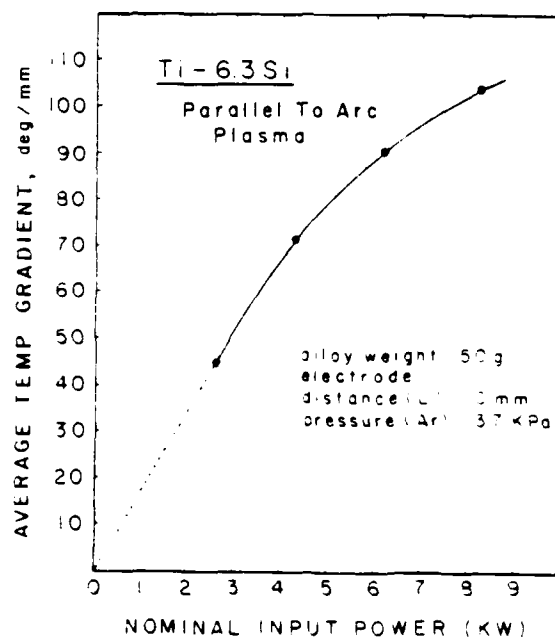


FIGURE 3
Plot of average temperature gradient vs. nominal input power.

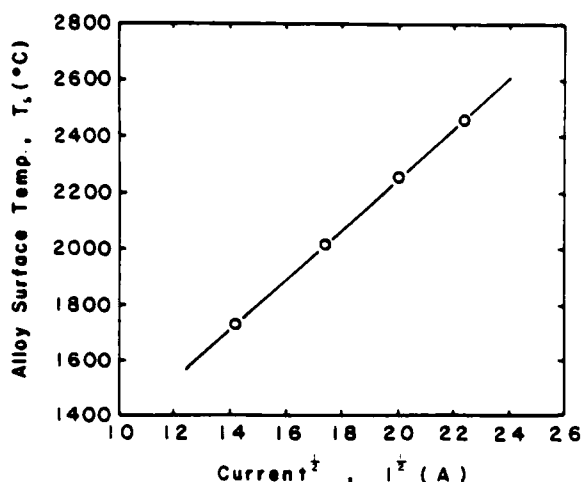


FIGURE 4
Plot of the top surface temperature vs. total input current.

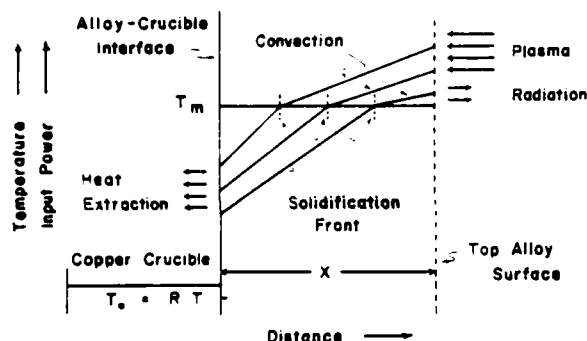


FIGURE 5
Schematic drawing of 1-D temperature profile along the thickness direction.

the range of 1200-2000°C is nearly constant [9], the heat flow of the steady state may be expressed using a standard 1-D poisson equation, neglecting heat flow in the radial direction (a and b axes)

$$\frac{d^2T}{dx^2} + \frac{Q_i}{k} = 0 \quad (2)$$

Where Q_i : heat generated by arc plasma

The solution of eq. (2) would provide temperature distribution as a function of x. In order to estimate the heat transfer coefficient (h) at the alloy-crucible

interface, this problem may be simplified into a plane wall case with the maximum temperature at the top surface.

$$h_I (T_I - T_O) = \frac{k(T_s - T_I)}{X} \quad (3)$$

Where:

h_I = heat transfer coefficient at the alloy-crucible interface

T_I = temperature of the alloy bottom surface

T_O = room temperature

X = alloy thickness (c axis)

Using equation (3), the heat transfer coefficient at the interface for the molten alloy is estimated as $\sim 0.6 \text{ W/cm}^2\text{-K}$ at $T_I = 1410^\circ\text{C}$. The value indicates that high interface resistance is characteristic in the cold hearth melting. On the other hand, at the top surface, heat transfer occurs in the form of radiation and Ar gas convection. The radiation can be expressed as:

$$Q_r = \epsilon \sigma T_s^4$$

Where: Q_r = heat loss through radiation

ϵ = total emissivity

σ = Stefan-Boltzman constant

Based on the previous assumptions, the radiation heat loss at $T_s = 2500^\circ\text{C}$ is $\sim 211 \text{ W/cm}^2$. The calculation of the heat transfer coefficient by the convection requires information about the ambient temperature near the surface.

Current 1-D heat flow analysis is not correct in a strict sense, since the temperature gradient and heat flux exist along the radial direction. Future study will include the solution of the 3-D poisson equation by a numerical method.

Many α -Ti alloys were spun by this unit and some of them are shown in Fig. 6(a) and 6(b). The ribbon alloy varies in thickness from 20 μm to 80 μm depending upon superheat and disk speed. Similar arguments can be applicable to flake materials.



FIGURE 6 (a)

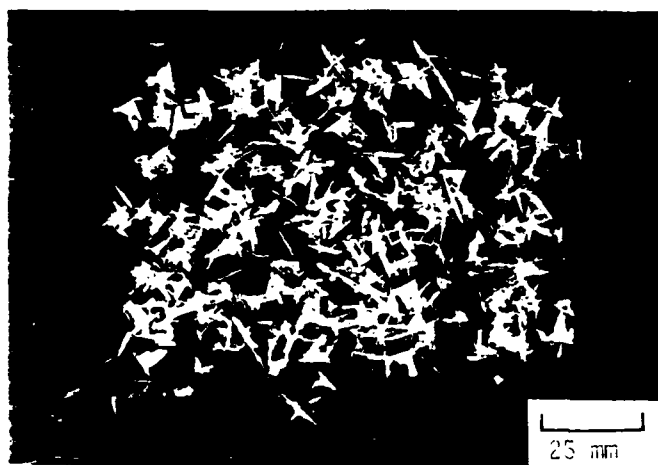


FIGURE 6 (b)

Figure 6. Spun materials by the pilot arc melt spinning unit (a) ribbon alloy (b) flake alloy.

4. CONCLUSIONS

1. Melting and spinning of Ti-6.3Si alloy in a cold copper crucible require large superheat and temperature gradient in the direction parallel to the incoming arc plasma due to the poor conductivity of this alloy.
2. The heat transfer coefficient of the melt-crucible interface is $\sim 0.6 \text{ W/cm}^2\text{-K}$ at 1410°C (above melting temperature).

3. The alloy surface temperature increases linearly with the square root of total current, provided other parameters such as Ar gas pressure, arc electrode distance are constant.
4. Heat loss by radiation from the top surface reaches as much as $\sim 10\%$ of the total heat loss at $\sim 2500^\circ\text{C}$.

ACKNOWLEDGEMENT

The authors would like to thank Mr. Y.T. Ning for his assistance in carrying out these experiments. The work has been supported by the office of Naval Research (contract No. N00014-82-K-05797). Contribution # 230 from Barnett Institute.

REFERENCES

1. N. J. Grant, U.S. Patent 3070468, Dec. 25, 1962.
2. Milton B. Vordahl, U.S. Patent 3622406, Nov. 23, 1971.
3. S.H. Whang, J. Metals, 36 (1984) 34.
4. S. M. L. Sastry, T.C. Peng P. J. Meschter, and J. E. O'Neal, J. Metals 35, (1983) 21.
5. R. Maringer and C. Mobley, J. Vac. Sci. Technology, 11 (1974) 1067.
6. P.R. Roberts and P. Loewenstein, in Powder Metallurgy of Titanium Alloys, F.H. Froes and J. E. Smugeresky eds. (TMS-AIME 1980) 21.
7. D.G. Konitzer, K.W. Walters, E.L. Heiser, and H.L. Fraser, Met. Trans. B, 15B (1984) 149.
8. S. H. Whang and R.C. Giessen, Proc. Third Conf. Rapid Solidification Processing, Robert Mehrabian ed, NBS (1982) 439.
9. C.Y. Ho, P.W. Powell, and P.E. Liley, J. Phys. and Chem. Ref. Data, vol. 3, 1974 supplement No 1, Am. Chem. Soc. and Am. Inst. Phy. for Nat. Bur. Stand.

MICROSTRUCTURES AND AGE HARDENING OF
RAPIDLY QUENCHED Ti-Zr-Si ALLOYS

S.H. Whang^a, Y.Z. Lu^a, and Y.W. Kim^b

Submitted to J. Mat. Sci. Lett.

^aBarnett Institute, Material Science Division, Northeastern University
Boston, MA 02115

^bMet. Cut. Materials Research Group, P.O. Box 33511,
Wright-Patterson AFB, OH 45433

MICROSTRUCTURES AND AGE HARDENING OF RAPIDLY QUENCHED Ti-Zr-Si ALLOYS

S.H. WHANG and Y.Z. LU

Barnett Institute of Chemical Analysis and Materials Science,
Northeastern University, Boston, MA 02115

Y-W. KIM

Metcut Materials Research Group, P.O. Box 33511, Wright Patterson
Air Force Base, OH 45433

Ti-Zr-Si alloys (0-8 at.% Si) rapidly solidified (RS) by arc melt spinning and the hammer-and-anvil techniques were studied to characterize microstructures and annealing behavior. TEM analyses show that extensive refinement of microstructures and extended solubility of Si (up to ~6at %) in Ti alloys result from rapid quenching. All the alloys exhibit a strong age-hardening at 500-600°C by forming uniformly distributed fine, spheroidal precipitates. At higher annealing temperatures, the precipitates become ellipsoidal, which is in contrast to rod or needle shaped silicides in conventional Ti alloys containing Si. A significant strength loss occurs after high temperature annealing (850-950°C/1-2 h) due largely to precipitate coarsening and in part to grain growth.

1. INTRODUCTION

Ti-Zr-Si alloys and their modified alloys have been studied by a number of authors [1-5] with respect to their strength, age hardening and creep strength. These alloys are strengthened by both solid solution of Zr and precipitates (silicides). The martensite structure that results from Zr addition provides not only an additional strength but also numerous nucleation sites for

the silicide precipitation. The precipitates $[(\text{Ti,Zr})_5\text{Si}_3]$ [2] in these alloys are more stable than Ti_5Si_3 precipitates in Ti-Si binary alloys, improving high temperature properties such as creep strength [6].

Recent alloy synthesis through rapid solidification processing yields extensive microstructural refinement [7,8] and extended solid solubility of solutes [9]. This, in many cases, leads to beneficial morphology and sizes of precipitates, aging response and mechanical properties that are not obtainable by conventional solidification techniques. In this paper, these effects are reported for rapidly solidified Ti-Zr-Si alloys.

2. EXPERIMENTS

$\text{Ti-Zr}_{10}\text{-Si}_{0-8}$ alloys were processed into ribbon (20-40 μm thick, 2 mm wide) by an arc melt spinning technique and foils (20-30 μm thick) by the hammer and anvil splat quenching technique. The injection pressure for this particular run was $\sim 8.8 \times 10^4$ Pa and the speed of the disk surface was ~ 18 m/sec. Samples of similar thickness ($\sim 20\mu\text{m}$) were used for the experiments in order to avoid experimental variation resulting from different cooling rates. The surface topology of ribbons and foils was examined by SEM and microstructures of foil samples were studied by TEM. For annealing, samples were wrapped with Ta foil and sealed in quartz tubings in vacuum. Annealing experiments were conducted in the temperature range of 350 - 850°C for 1-60 h. Microhardnesses of as-quenched and annealed samples were measured using a Vickers diamond pyramid tester with loads of 50 and 100 g.

3. RESULTS AND DISCUSSIONS

3.1 As-Quenched State

The free surface of ribbon processed by an arc melt spinner shows characteristic dimples (Fig. 1a) and the chill side has wetting patterns and relaxed air pockets (Fig. 1b and 1c). TEM observations show that as-quenched microstructures of all the alloys studied consist of equiaxed dendritic cells containing extremely fine martensite structure, as is shown in alloy $Ti_{84}Zr_{10}Si_6$ (Fig. 2a). The dark field image (Fig. 2c) of bright spots of the ring pattern (Fig. 2b) shows that the ring patterns consist of reflections from the fine cells. Up to the Si content of 6%, no precipitates were detected indicating that the extended solid solubility of Si in the Ti-Zr alloy is at least 6 at %.

As-quenched microhardness values are shown as a function of Si content (Fig. 3). Hardness increase in the Ti-Zr-Si alloys is a linear function of Si concentration up to 8% Si see (Fig. 3) which is consistent with TEM observations. The strength increment of Ti-Zr alloys is somewhat less with Si addition than with B addition [10].

3.2 Annealed State

Isothermal annealing at $550^{\circ}C$ resulted in gradual disappearance of martensite structure, nucleation of precipitate, formation of better defined sub-grain structure (0.1-0.3 μm dia.), and elimination of dendritic cells, as shown in $Ti_{84}Zr_{10}Si_6$ alloy (Fig. 4a). Fine, spherical precipitates ($\sim 30nm$) appear along prior dendritic cell boundaries. The corresponding

diffraction patterns (Fig. 4b) show tiny diffraction spots inside the first ring, which is in agreement with the appearance of the precipitates. The precipitates were not identified, but they are likely to be silicides. A high temperature annealing (800°C-900°C) resulted in coarsening of the precipitates (to 0.5-1 μ m) and grain growth (to 1-3 μ m) as shown in Fig. 5a. The corresponding diffraction patterns (Fig. 5b) exhibit many distinctive spots from the large precipitates (Fig. 5c). It is not clear whether these large silicides have the same structure as that of fine precipitates in Fig. 4. Such significant coarsening of silicide particles at a high temperature (Fig. 5a) may be explained by observing particle coarsening in a Ti-5Al-2Si alloy [11]. The coarsening rate of the silicides in this alloy system shows that the cube of particle radius increase per second is $\sim 3.4 \times 10^{-26} \text{ m}^3/\text{sec}$ at 800°C. The estimated diffusivity of Si in the Ti-5Al matrix is $\sim 1.2 \times 10^{-11} \text{ cm}^2/\text{sec}$. It appears that the high coarsening rate of silicides in Ti is attributable to the high diffusivity of Si in Ti alloys.

Microhardness of Ti-Zr-Si alloys increases at 550°C with time up to 20h and decreases with further annealing (Fig. 6). Similar trends are observed in the isochronal (2h) annealing curve (Fig. 7) where Ti-Zr₁₀-Si₈ age-hardens with temperature up to 600°C and softens significantly above 700°C. The hardness change is in accordance with precipitating as well as other microstructural coarsening. The strong age hardening observed in the rapidly

solidified Ti-Zr-Si foil alloys (Fig. 6 and Fig. 7) is in contrast to mild age hardening in the solution treated Ti-Zr-Si alloys [2]. This is because RS alloys contain a higher volume fraction of fine precipitates than their counterparts, conventional ingot alloys. Another distinctive feature observed in the RS Ti alloys is remarkably refined grain sizes and martensite structures. It is noted that the grain size remains within a sub-micron range even after annealing at high temperatures (850-950°C/1-2h) [7].

ACKNOWLEDGEMENT

We thank the Office of Naval Research for the support of this work. (Contract ONR N00014-82-K-0597) Contribution #202 from the Barnett Institute.

REFERENCES

1. K.C. Antone, Trans AIME, 242 (1968) 1454.
2. H.M. Flower, P.R. Swann, and D.R.F. West, Met. Trans. 2 (1971) 3289.
3. N.W. Paton and M.W. Mahoney, Met. Trans A 7A (1976) 1685.
4. S.M. Tuominen, G.W. Franti, and D.A. Koss, Met Trans. A, 8A (1977) 457.
5. C. Ramachandra and Vakil Singh, Met. Trans A, 13A (1982) 771.
6. H.M. Flower, P.R. Swann and D.R.F. West, in Titanium Science and Technology, R.J. Jaffee and H.M. Burte, eds., Plenum Press, New York, NY (1973), vol. 2, pp. 1143-54.
7. C.S. Chi and S.H. Whang, Proc. Materials Research Society, Nov., 1983, Boston, in press.
8. S.H. Whang, J. Metals, 36 (1984) 34-40.
9. S.H. Whang and C.S. Chi, unpublished results (1984).

10. Y.Z. Lu and S.H. Whang, unpublished results (1984).
11. S.H. Whang, Y.Z. Lu and B.C. Giessen, Proc. Materials Research Society Symposium, Boston MA (1983), in press.

FIGURE CAPTIONS

Figure 1. SEM micrographs of as-quenched $\text{Ti}_{84}\text{Zr}_{10}\text{Si}_6$ ribbon alloy

- a. The free surface (x50)
- b. The substrate side surface (x50)
- c. Detailed micrograph of b (x200)

Figure 2. TEM micrograph of as-quenched $\text{Ti}_{84}\text{Zr}_{10}\text{Si}_6$ foil alloy

- a. Bright field micrograph
- b. Selected area diffraction
- c. Dark field micrograph

Figure 3. Microhardness of $\text{Ti-Zr}_{10}\text{-Si}$ alloy system as a function of Si Content.

Figure 4. TEM micrograph of aged $\text{Ti}_{84}\text{Zr}_{10}\text{Si}_6$ at 550°C , 20 h

- a. BFM
- b. SAD

Figure 5. TEM micrograph of annealed $\text{Ti}_{84}\text{Zr}_{10}\text{Si}_6$ alloy at 950°C , 2 h

- a. BFM
- b. SAD
- c. DFM

Figure 6. Microhardness of $\text{Ti-Zr}_{10}\text{-Si}$ alloys as a function of time at 550°C

Figure 7. Microhardness of $\text{Ti}_{84}\text{Zr}_{10}\text{Si}_6$ alloy as a function of annealing temperature (2h each)

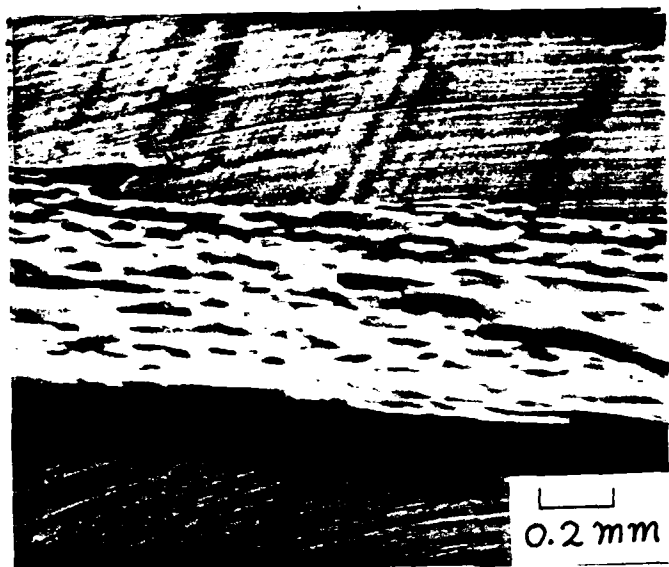


Figure 1 a



Figure 1 b

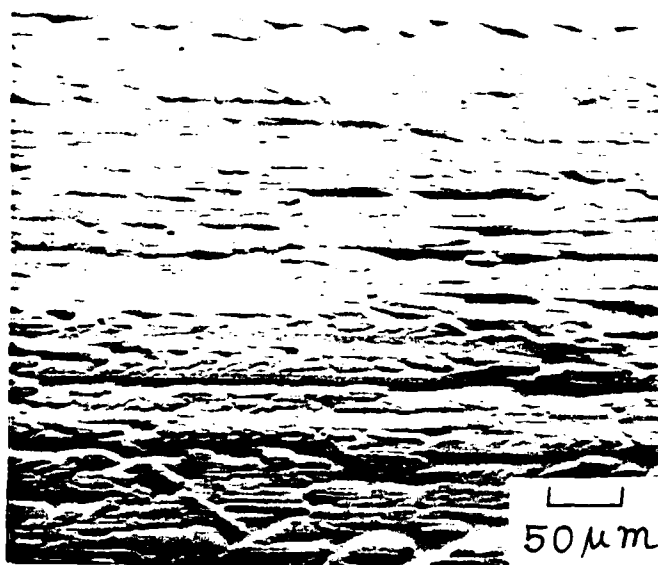


Figure 1 c

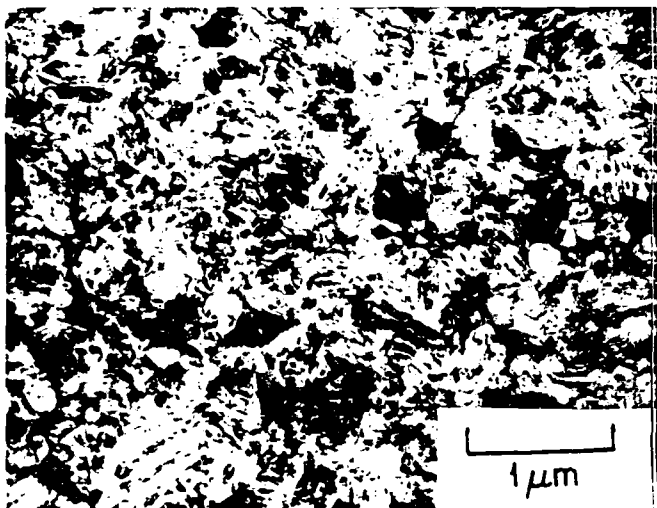


Figure 2 a

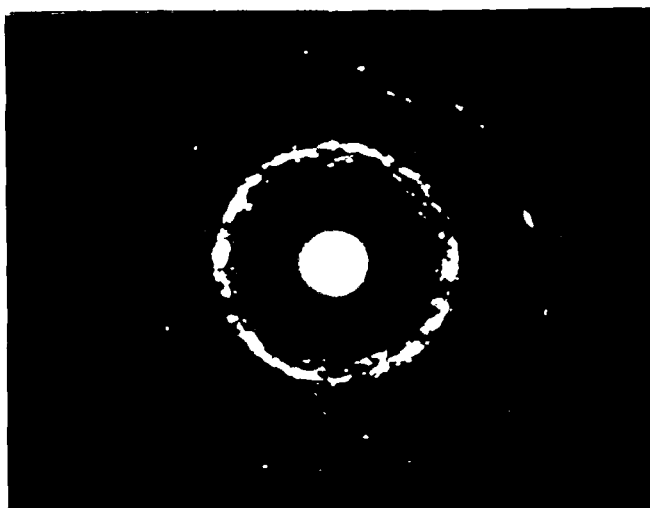


Figure 2 b

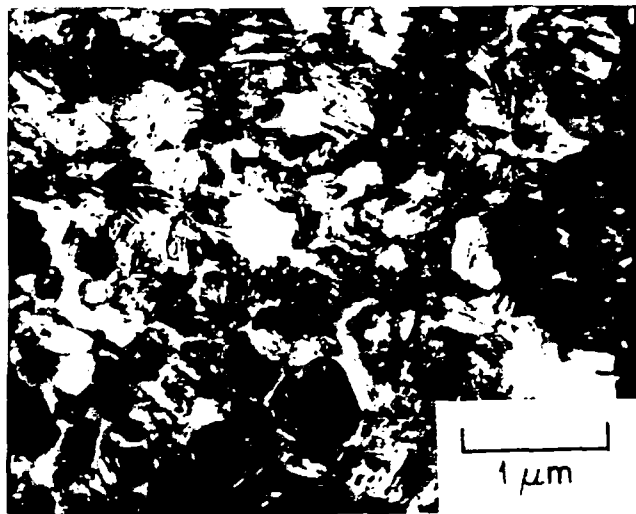


Figure 2 c

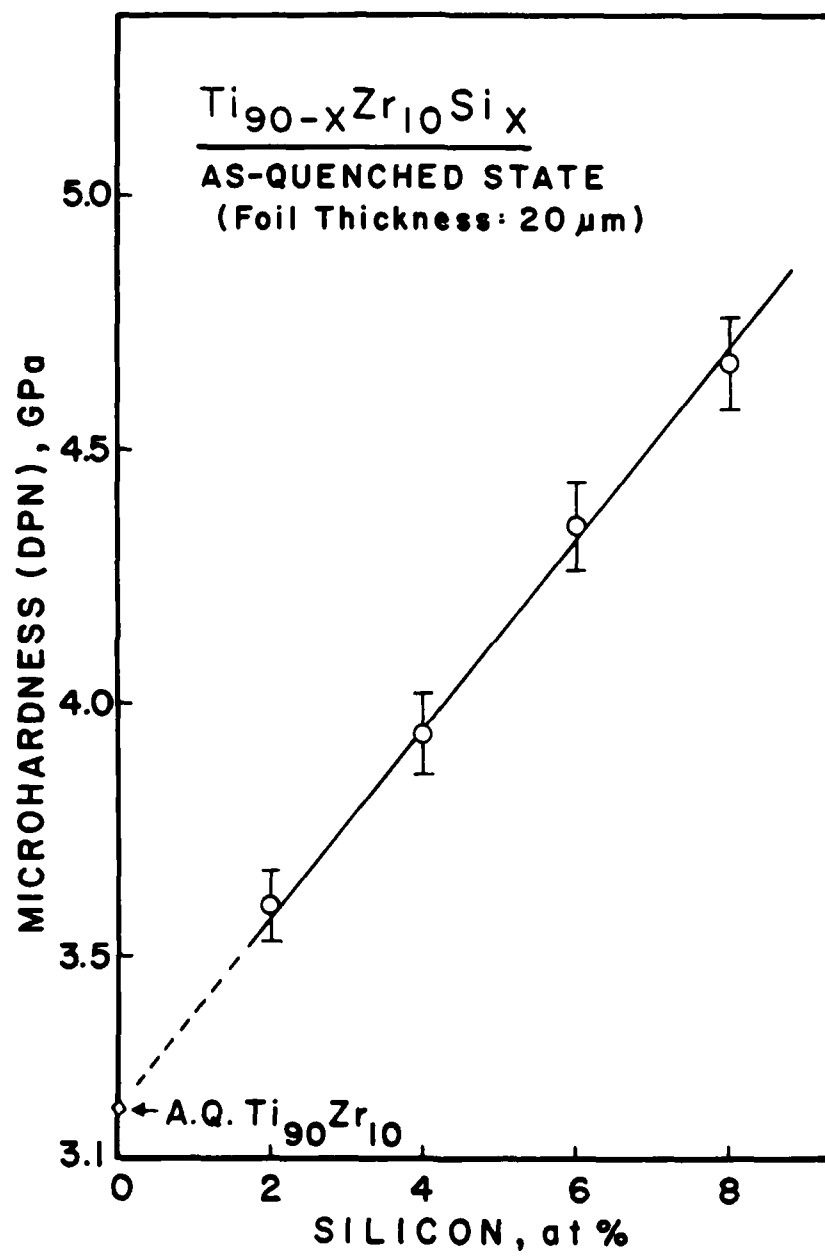


Figure 3

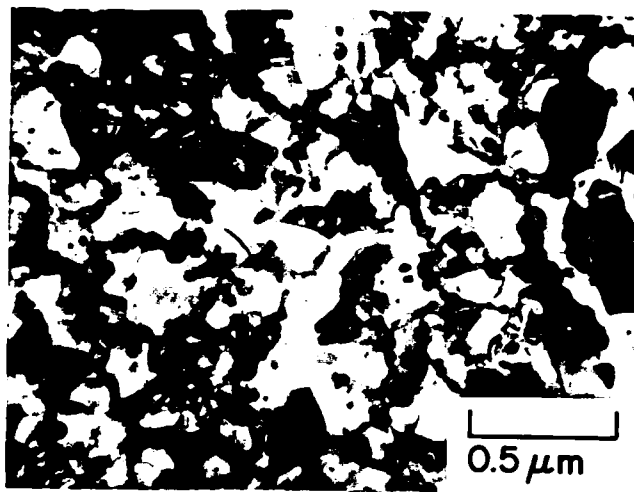


Figure 4 a

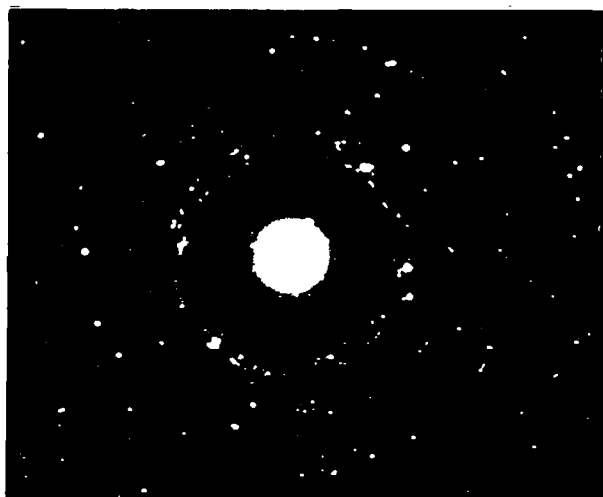


Figure 4 b

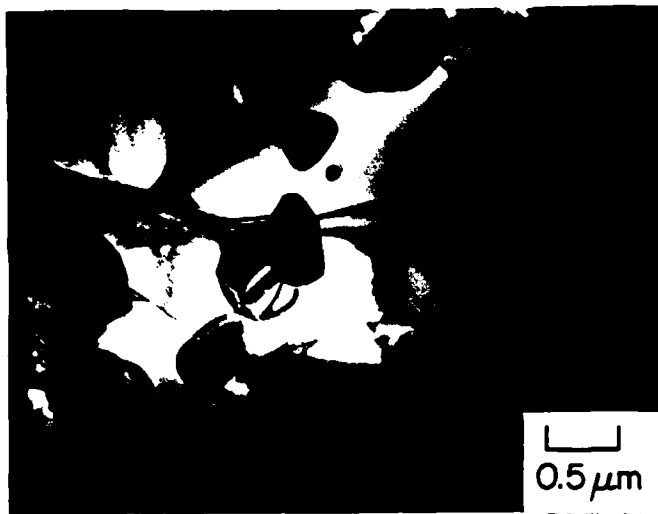


Figure 5 a

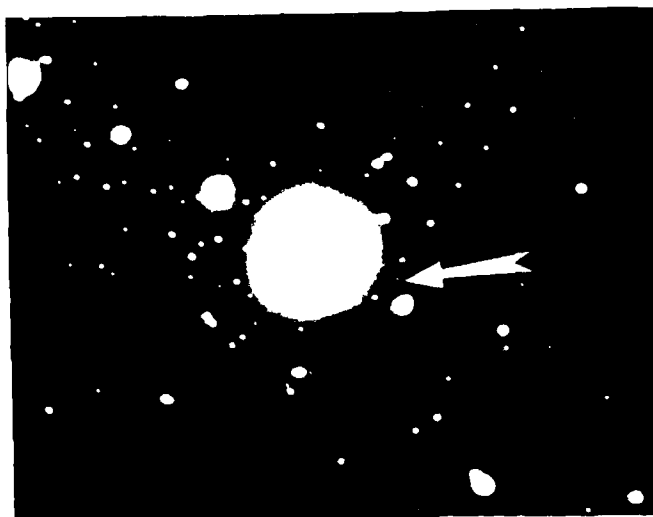


Figure 5 b

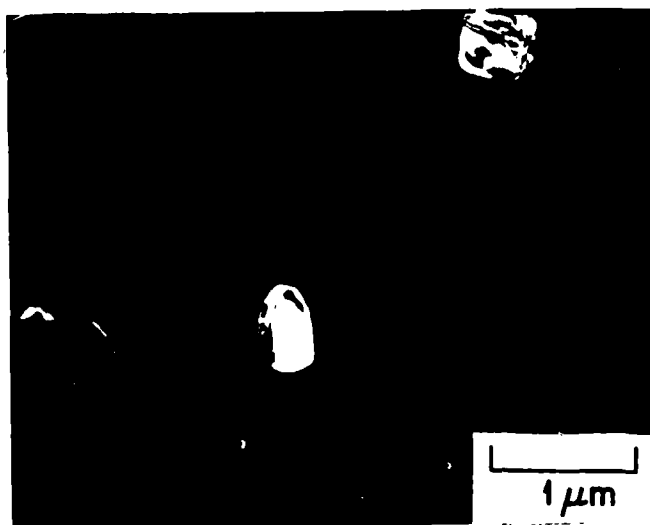


Figure 5 c

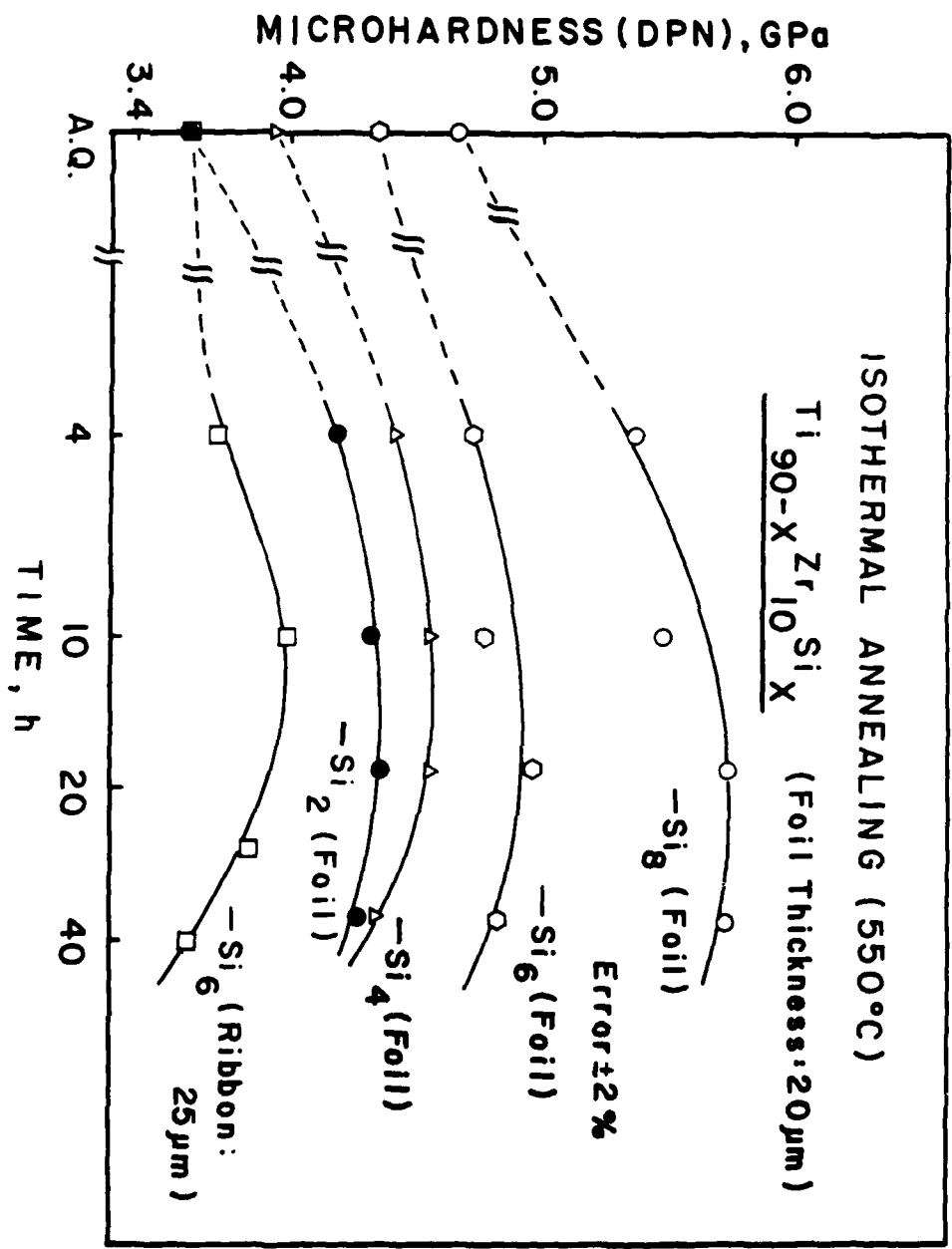


Figure 6

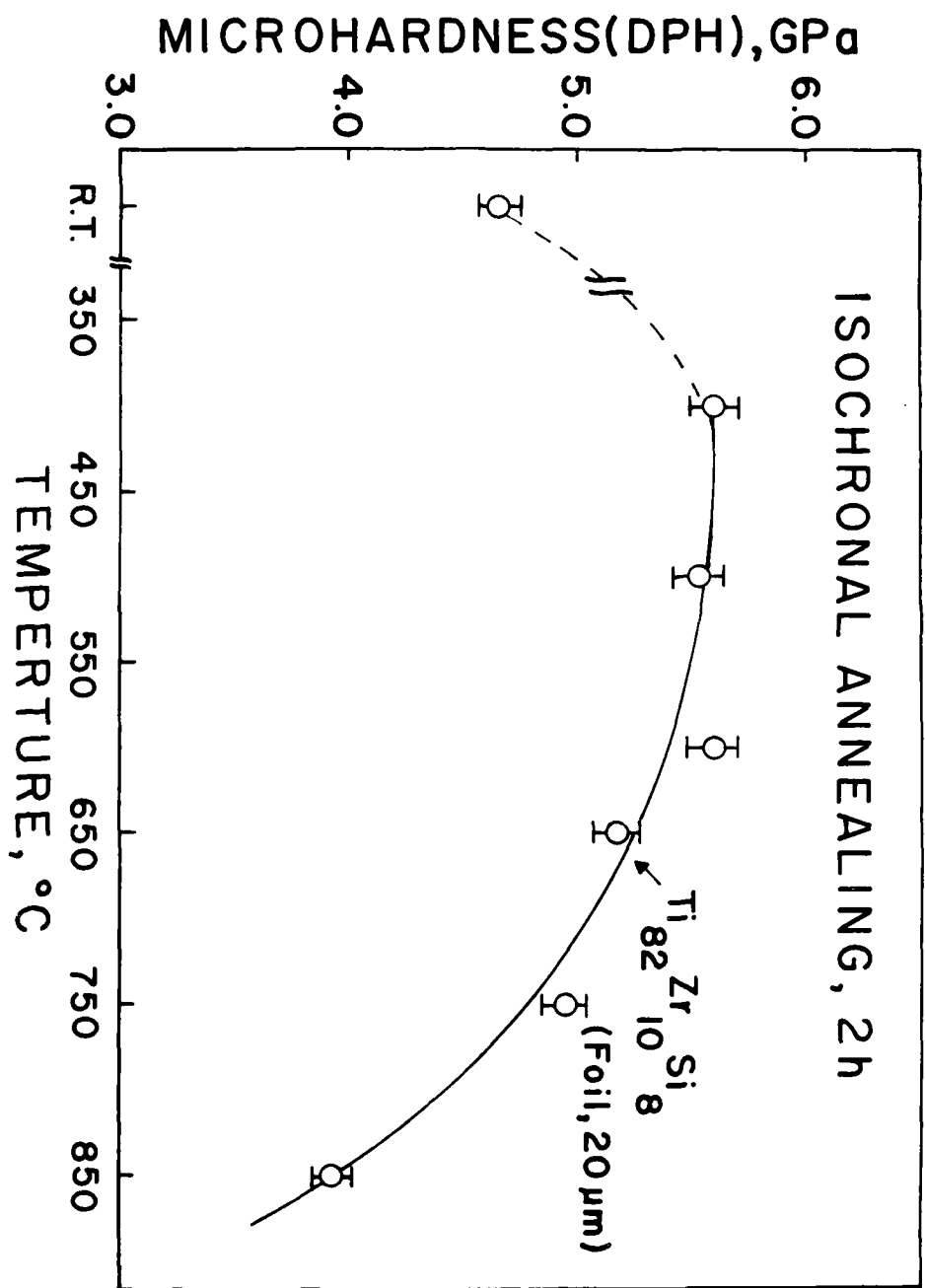


Figure 7

PRECIPITATION HARDENING OF RAPIDLY QUENCHED Ti-Zr-B ALLOYS

Y.Z. Lu and S.H. Whang

Submitted to J. Mat. Sci., Nov. 1984

PRECIPITATION HARDENING OF RAPIDLY QUENCHED Ti-Zr-B ALLOYS

Y.Z. Lu and S.H. Whang

Barnett Institute of Chemical Analysis and Materials Science
Northeastern University, Boston, MA 02115

Extensive solid solubility of boron (up to 6 at.%) in Ti can be achieved through rapid solidification (the cooling rate of $\sim 10^6$ K/sec). A small increase in lattice parameters is noted with increasing boron concentration in Ti. Transmission electron microscope observations show that age hardening in this alloy is associated with very fine boride precipitates that are preferentially formed along prior-beta grain boundary. These precipitates also grow directionally into rod shapes after annealing at elevated temperatures. A strong age hardening occurs from 500°C to 600°C, whereas a significant softening due to microstructural coarsening exists above 800°C.

1. INTRODUCTION

In recent years, research on rapidly solidified Ti alloys has been focused on the formation of stable dispersion by novel additives in the Ti matrix [1-5]. In the past, the dispersion strengthening of Ti alloys has been investigated with Si addition through solution treatment [6-8]. By contrast, the fact that boron has little solubility in Ti at high temperature makes it difficult to utilize solution treatment. Alternatively, homogeneous Ti-B alloys can be prepared through rapid solidification processing. The succeeding heat treatment would result in uniform titanium borides (TiB , TiB_2), which are attractive as dispersions because of their good stability at high temperatures.

Previously, the effects of Ti borides on microstructure and mechanical

properties in Ti-5Al-2.5Sn-1B alloy were reported [2,9]. In this paper, a study on the effects of B addition to Ti-Zr₁₀ alloys will be discussed.

2. EXPERIMENTS

Small Ti_{90-x}-Zr₁₀-B_x and Ti_{100-x}B_x alloy buttons (1-2g) were prepared by melting pure Ti (99.9%), Zr (99.9%) and B (99.5%) in an arc furnace under Ar gas atmosphere where $x = 0-8$ at %. The buttons were remelted repeatedly to insure compositional homogeneity. Splat foils and thin ribbons were made by the hammer and anvil technique and by an arc melt spinning technique [10-11], respectively (Fig. 1). In the arc melt spinning technique, an alloy button (0.5-1g) is melted in a cold copper crucible and injected through an orifice (0.5-1 mm dia) centered in the crucible by applying a gas pressure differential above and beneath the crucible. The spinning speed for the ribbon processing and the pressure differential for the injection were ~ 18 m/sec and $\sim 8.8 \times 10^4$ Pa, respectively. Surface topology of as-quenched samples was examined by scanning electron microscopy (SEM) and microstructural changes with heat treatment were examined by transmission electron microscopy (TEM). Thermal properties of alloy ribbon were studied by differential scanning calorimetry (DSC) at a temperature range of 293 K to 1000 K with a heating rate of 20°/min. Microhardness of samples (the substrate side surface) was measured by the Vickers diamond pyramid tester with loads of 50g and 100g.

3. RESULTS AND DISCUSSIONS

3.1 Microstructures

Fig. 2 shows SEM micrographs of the free surface (a) and the substrate side surface (b) of as-spun Ti₈₄Zr₁₀B₆ alloy ribbons. The free

surface is characterized by longitudinal wavy patterns with finely distributed dimples. The substrate-side contains large air pockets and fine wetting patterns.

As-quenched Ti_{96}B_4 alloy did not contain any precipitates, according to the bright field micrograph (Fig. 3a) and the diffraction patterns (Fig. 3b). Microstructures of as-quenched ternary alloy $\text{Ti}_{84}\text{Zr}_{10}\text{B}_6$ (Fig. 4a) consisted of fine martensite structure, prior-beta grain (1-3 μm) and cellular structure along the prior-beta grain boundaries. The diffraction pattern (Fig. 4b) from Fig. 4a does not show the presence of any precipitates.

Upon aging at 550°C for 20 h, the fine martensite structure changed into lenticular shaped structure while the prior-beta grain boundary produced G.P. zone-like precipitates (Fig. 5a), which are identified as spot patterns inside the first ring pattern of the diffraction patterns (Fig. 5b). The size of G.P. zone-like precipitates ranges up to 100 Å in diameter. When heat treated at 950°C for 2 h, the precipitates grow into rod-shaped structures with high aspect ratios (Fig. 6a and b). The growth of grains is sluggish and their average size is generally smaller than 1 μm after annealing at 950°C for 2 h.

3.2 Extended Solid Solubility

Equilibrium solid solubility of B in α -Ti is very small (0.43 at %, 886 C), whereas rapidly solidified Ti-B alloys (cooling rate 10^5 - 10^6 deg/sec [3]) show homogeneous matrices up to 6 at %B based on the TEM study (Figs. 3a and 4a). The lattice parameters of the as-quenched Ti-B alloys measured by x-ray diffractometer are shown in Fig. 7. The x-ray patterns exhibit both significant line broadening and peak amplitude decrease with

increasing B concentration, indicative of lattice strain, probably caused by boron solid solution. Both a and c axes increase with increasing boron concentration. In addition, a large increase in the c axis and a small increase in the a axis results in the increase in c/a ratio. This trend is in agreement with the case of carbon in Ti as shown in Table 1. Despite boron's having a larger atomic size than carbon, the lattice expansion by boron is rather smaller than that of carbon. This discrepancy raises a question--does boron form the interstitial solid solution, as does the carbon in Ti? First, the atomic radius of boron (0.82 \AA) is larger than the octahedral hole radius (0.61 \AA) by about 34.4%; in comparison, there is a 27% difference between carbon (0.77 \AA) and the hole radius. Therefore, from this simple argument, it is not likely that all boron atoms reside at the interstitial site. The absence of B atoms from the interstitial sites may be attributed to one of the following circumstances: 1) The boron segregates to the prior beta grain boundary ($\sim 2 \mu\text{m}$ dia). The calculated average diffusion length is $0.8 - 1.5 \mu\text{m}$, using alloy cooling rate $\sim 10^5$ k/sec and diffusivity of carbon in Ti at 1100°C (representative temperature). This figure indicates a real possibility of a certain degree of such segregation to the prior grain boundary, though the actual diffusivity of B in Ti might be lower than that of carbon. A distinct dark line separating the prior beta grain boundaries, however, was observed (Fig. 4a). It is not known how much boron segregates to the boundaries. 2) Another plausible explanation for the absence of boron from the interstitial site may be that the boron atom occupies the substitutional site (1.32 \AA radius) which is 60% larger than the boron atom radius ($12n.n$). Evidently, such replacement leads to the collapse of the substitutional site and forms a strong compression field center. 3) As a hypothetical situation (since

sufficient evidence does not exist to support this argument, two boron atoms occupy one substitutional site and one octahedral site (or one tetrahedral) depending upon energy minimization. It is interesting to see whether or not this is a similar situation to the di-substitutional solid solution in rapid-quenched Gd-Fe [14]. 4) As the last possible explanation, the rest of the atoms may form clusters which can't be identified by ordinary x-ray diffraction. From the evidences given, this possibility also can't be ruled out.

In order to resolve the site question, it is desirable to measure density and to study electrical resistivity, Mössbauer spectra and EXAFS of as-quenched alloy. In addition, the sample quenched at a cooling rate of 10^7 deg/sec or larger should be used in order to prevent significant segregation to the sub-grain boundary.

Thermal behavior of $\text{Ti}_{84}\text{Zr}_{10}\text{B}_6$ alloy foils has been studied by DSC. No visible exothermic peak was observed up to 1000 K. This indicates that fine boride formation is not related to the strong exothermic reaction.

3.3 Mechanical Properties

Microhardness increase in $\text{Ti-Zr}_{10}\text{-B}$ alloys is linearly proportional to B concentration (Fig. 8), which is in agreement with that in $\text{Ti}_{90-x}\text{Zr}_{10}\text{Si}_x$ alloys where $x=0-6$ at.% [15]. The degree of hardness increment is more distinct in the B containing alloy than in the Si containing alloy. The $\text{Ti}_{86}\text{Zr}_{10}\text{B}_4$ foil alloy shows a strong age hardening response at 550°C while the $\text{Ti}_{82}\text{Zr}_{10}\text{B}_8$ foil alloy exhibits a slight age hardening (Fig. 9). The $\text{Ti}_{84}\text{Zr}_{10}\text{B}_6$ ribbon alloy has lower hardness than the foil alloys ($\text{Ti}_{82}\text{Zr}_{10}\text{B}_8$, $\text{Ti}_{86}\text{Zr}_{10}\text{B}_4$) and its aging response is relatively weak. Isochronal annealing of $\text{Ti}_{84}\text{Zr}_{10}\text{B}_6$ foil alloy (Fig. 10) demonstrates that a significant softening occurs above 800°C after 2 h due to the precipitate coarsening, as is shown in Fig. 6a.

Microstructural features such as early precipitation and dendritic

structure along a prior-beta grain boundary suggest that this boundary is rich with B and, therefore, solidified at the last minute. In the isothermal annealing curve, the microhardnesses of alloy ribbons is systematically lower than those of splat alloys. This is because low population of fine precipitates ($\sim 100 \text{ \AA}$ dia) are present in the ribbon alloys, as shown by microstructural study. That is, coarse precipitates already exist in the ribbon materials at the as-quenched state. This low cooling of the ribbon alloy for a given thickness results primarily from the one-sided substrate quench and, secondarily, from the fact that the ribbon contact with the substrate is not ideal at the cooling stages, a situation evidenced by air pockets and wetting patterns [3].

ACKNOWLEDGEMENT

We would like to express our gratitude for the support by the Office of Naval Research (Contract ONR N00014-82-K-0597). Many thanks are due to Dr. Y-W Kim for his help in the preparation of TEM micrographs and manuscripts. Contribution #203 from the Barnett Institute.

REFERENCES

1. S.H. Whang, J. Metals, 36 (1984) pp 34-40.
2. C.S. Chi and S.H. Whang, Proc. Materials Research Society Symposium, Vol. 28 (1984) pp 353-360.
3. C.S. Chi and S.H. Whang, submitted to Met. Trans, A, Nov., 1984
4. S.M.L. Sastry, T.C. Peng, P.J. Meschter and J.E. O'Neal, J. Metals, 35 (1983) pp 21-28.
5. S.M.L. Sastry, P.J. Meschter and J.E. O'Neal, Met. Trans A, 15A (1984) pp 1451-1474.
6. H.M. Flower, P.R. Swann and D.R.F. West, Met. Trans. 2, (1971) 3289.
7. S.M. Tuominen, G.W. Franti and D.A. Koss, Met. Trans. A, 8A (1977) 457.
8. C. Ramachandra and Vakil Singh, Met. Trans. A, 13A (1982) 771.

9. C.S. Chi and S.H. Whang, TMS-AIME paper Selection F83-14, September, 1983.
10. D.G. Konitzer, B.C. Muddle and H.L. Fraser, Met. Trans. A, 14A (1983) pp 1979-1988.
11. S.H. Whang and B.C. Geissen, Proc. Third Conf. Rapid Solidification Processing, R. Mehrabian, ed; NBS, 1982, p 439.
12. I. Cadoff and J.P. Nielson, Trans. AIME 197 (1953) 248.
13. W.L. Finley and J.A. Snyder, Trans AIME, 188 (1950) 277.
14. R. Ray, M. Segnini and B.C. Giessen, Solid State Communication, Vol. 10 (1972) 163-167.
15. S.H. Whang, Y.Z. Lu and Y-W Kim, submitted to J. Mat. Sci. lett., Nov. 1984.

FIGURE CAPTIONS

- Figure 1. Schematic figure of an arc melt spinning unit.
- Figure 2. SEM micrographs of surfaces of alloy ribbon.
(a) The free surface exposed to Ar atmosphere.
(b) The substrate side surface contacted with a copper disk.
- Figure 3. TEM micrographs of as-quenched Ti_{96}B_4 alloy.
- Figure 4. TEM micrographs of as-quenched $\text{Ti}_{84}\text{Zr}_{10}\text{B}_6$ alloy.
- Figure 5. TEM micrographs of $\text{Ti}_{84}\text{Zr}_{10}\text{B}_6$ alloy aged at 550°C, 10 h.
- Figure 6. TEM micrographs of $\text{Ti}_{84}\text{Zr}_{10}\text{B}_6$ alloy annealed at 950°C, 2 h.
(a) BFM
(b) SAD
- Figure 7. Lattice parameters of Ti-B (0-6 at %B).
- Figure 8. Plot of microhardness vs. B concentration in Ti-Zr-B alloys
- Figure 9. Plot of age hardening of Ti-Zr-B alloys at 550°C.
- Figure 10. Plot of isochronal annealing of Ti-Zr-B alloys from 350°C to 850°C.

TABLE 1

| Alloy | Lattice Expansion per Unit at % | | | | Max. Equil. Alpha Solubility |
|---|------------------------------------|--------------|----------------|--------------|---------------------------------|
| | Δc (Å) | ϵ_c | Δa (Å) | ϵ_a | |
| Ti ₉₉ B ₁ (as quenched) | 0.0096 | 0.0020 | 0.0013 | 0.00044 | 0.43 |
| Ti ₉₉ C ₁ (Equilibrium) | 0.0126 | 0.0027 | 0.0027 | 0.00091 | 2 [12] [13] |

$$\epsilon_c = \frac{\Delta c}{c_o}$$

$$\epsilon_a = \frac{\Delta a}{a_o}$$

Where Δc and Δa are lattice parameter increments for 1 at %B; $c_o = 4.686 \text{ Å}$ and $a_o = 2.950 \text{ Å}$.

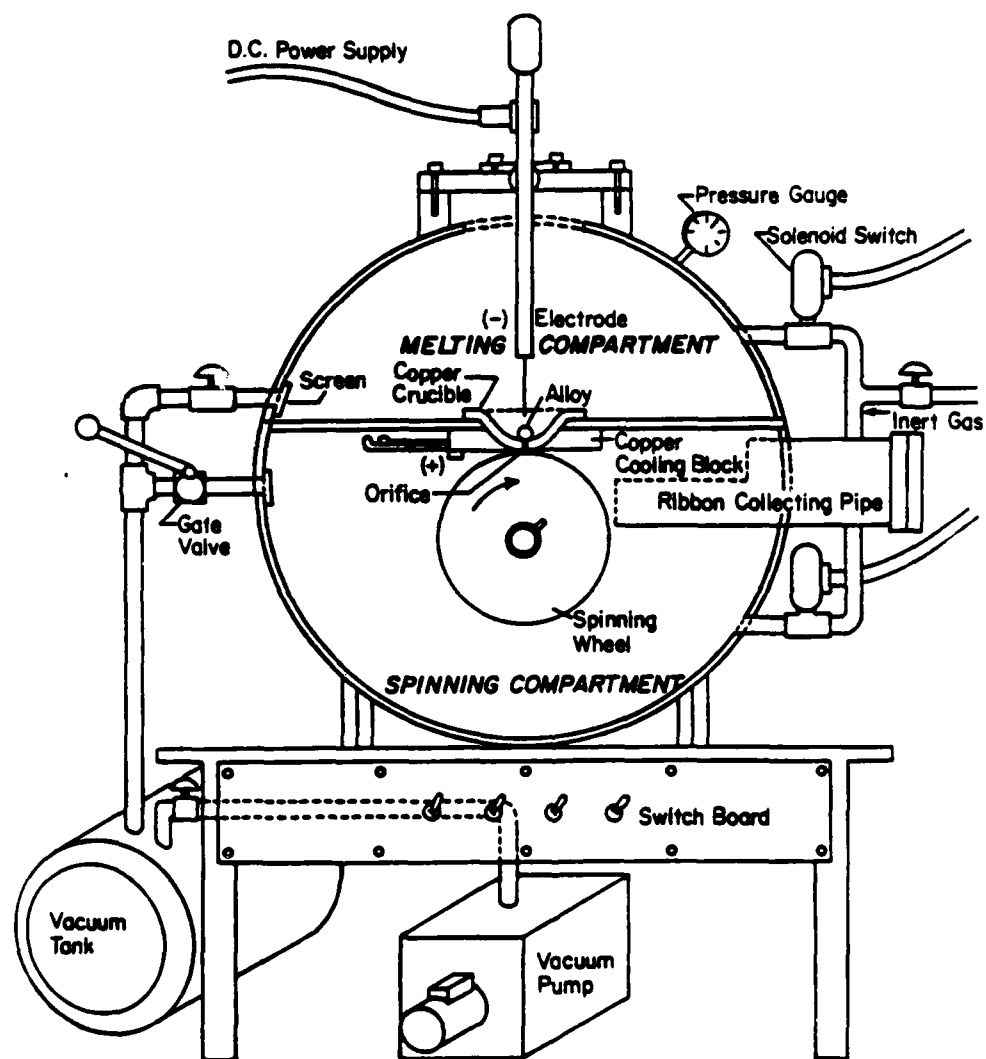


Fig. 1

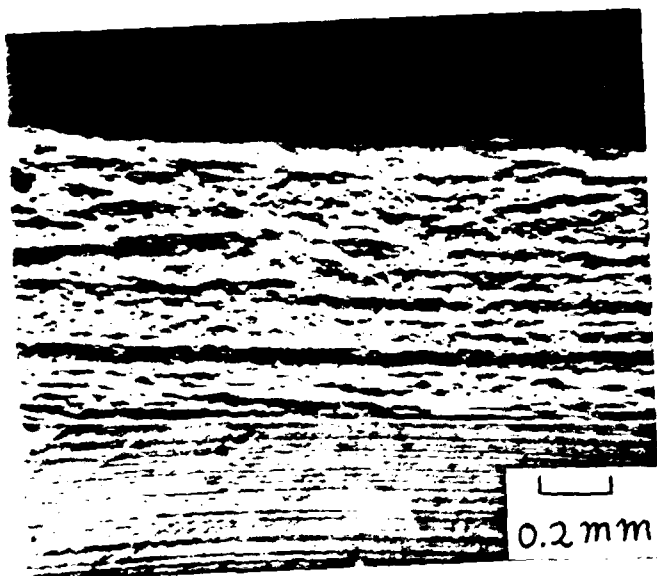


Fig. 2a

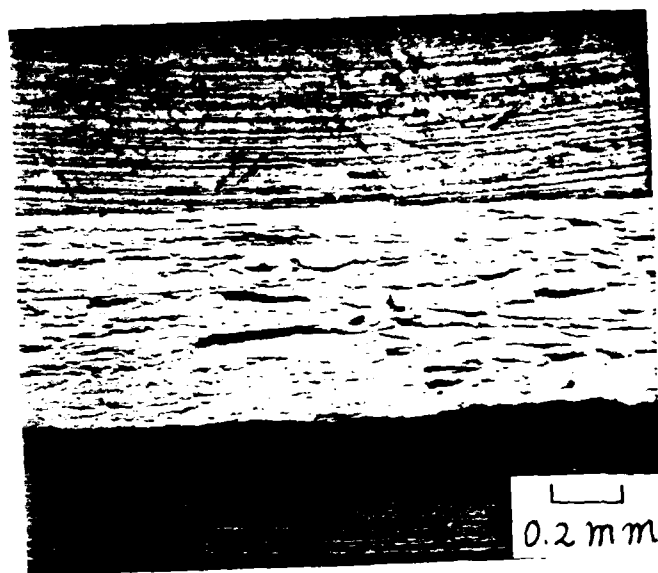


Fig. 2b

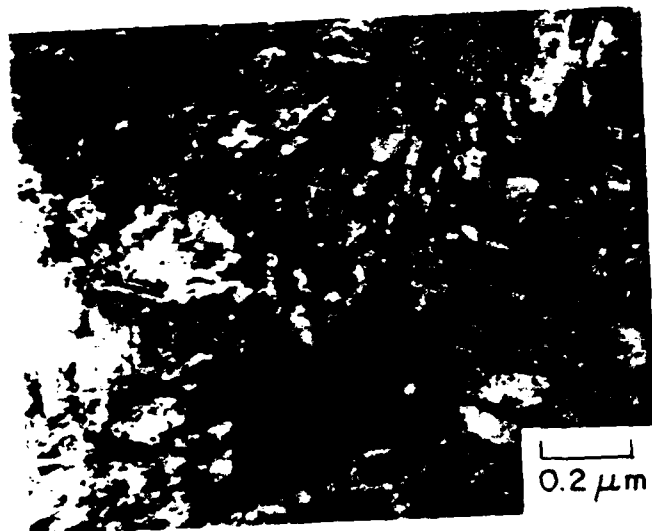


Fig. 3a

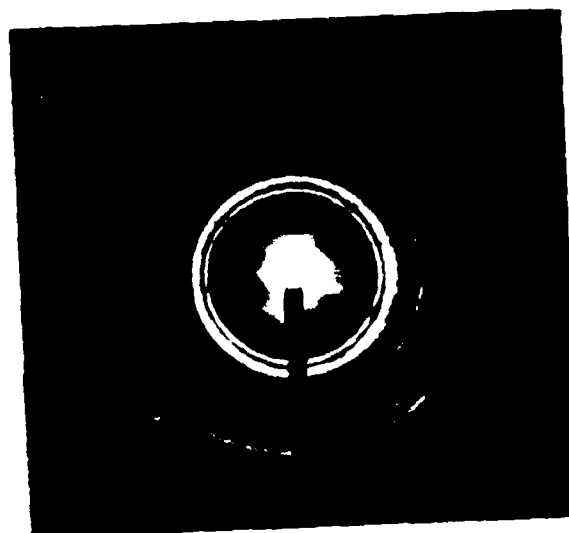


Fig. 3b

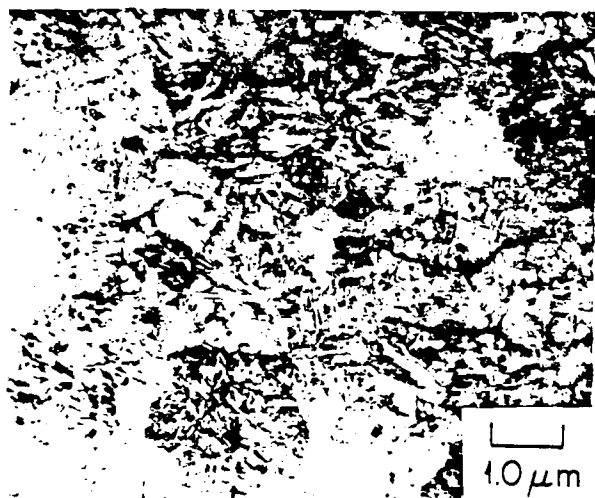


Fig. 4a

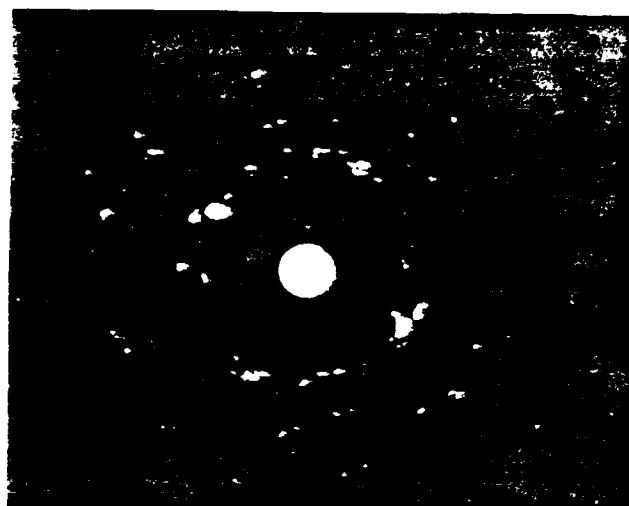


Fig. 4b

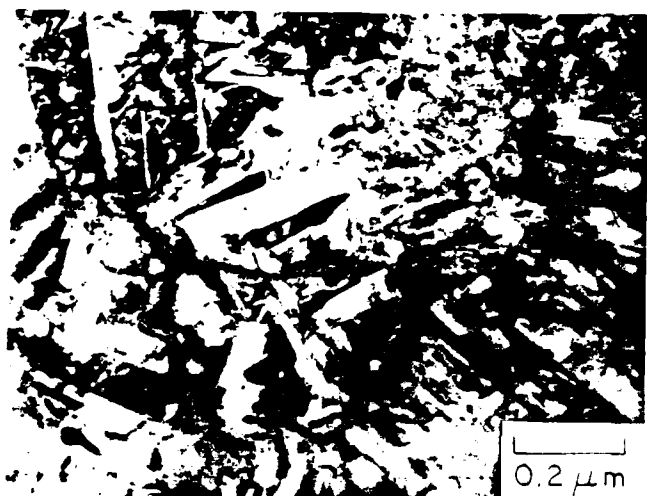


Fig. 5a

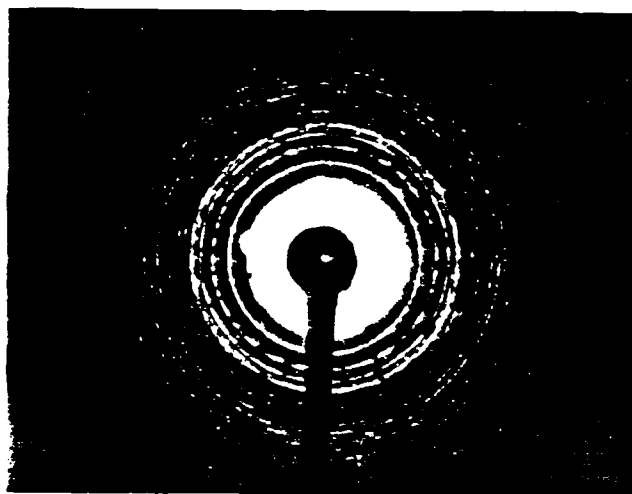


Fig. 5b

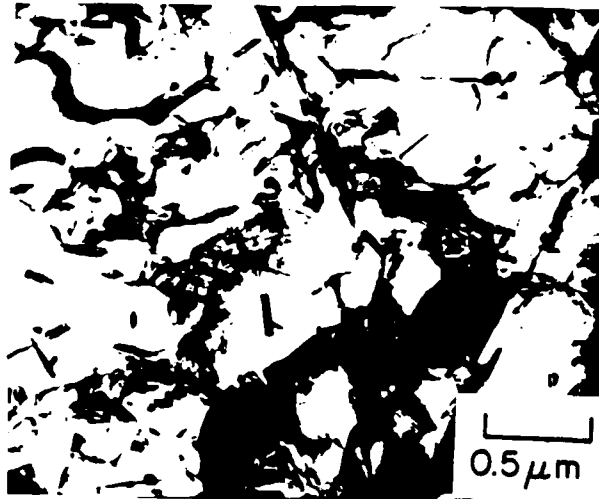


Fig. 6a

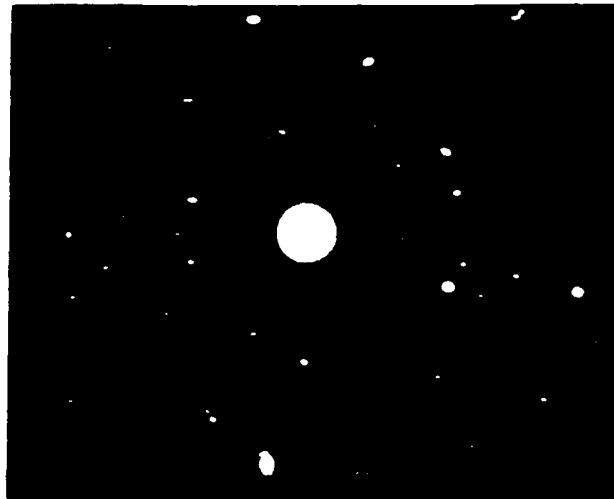


Fig. 6b

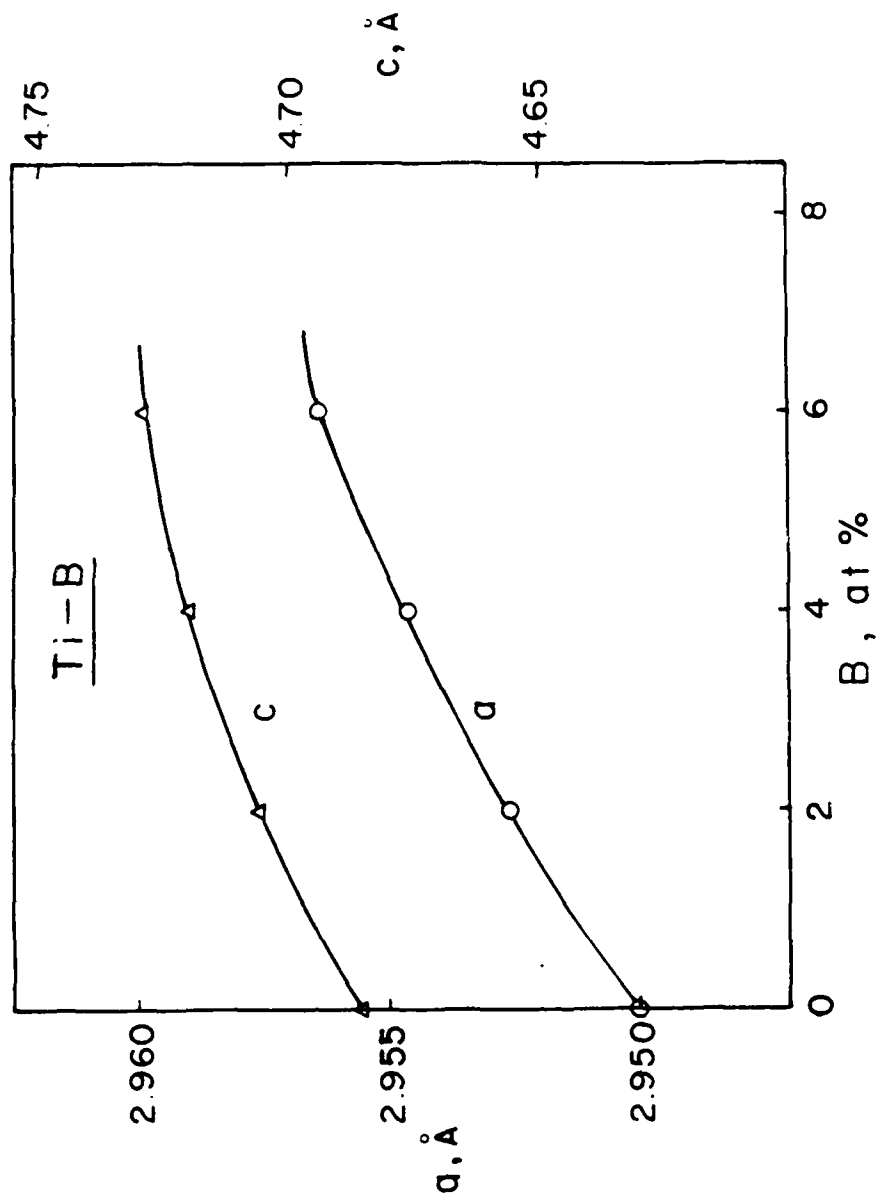


Fig. 7

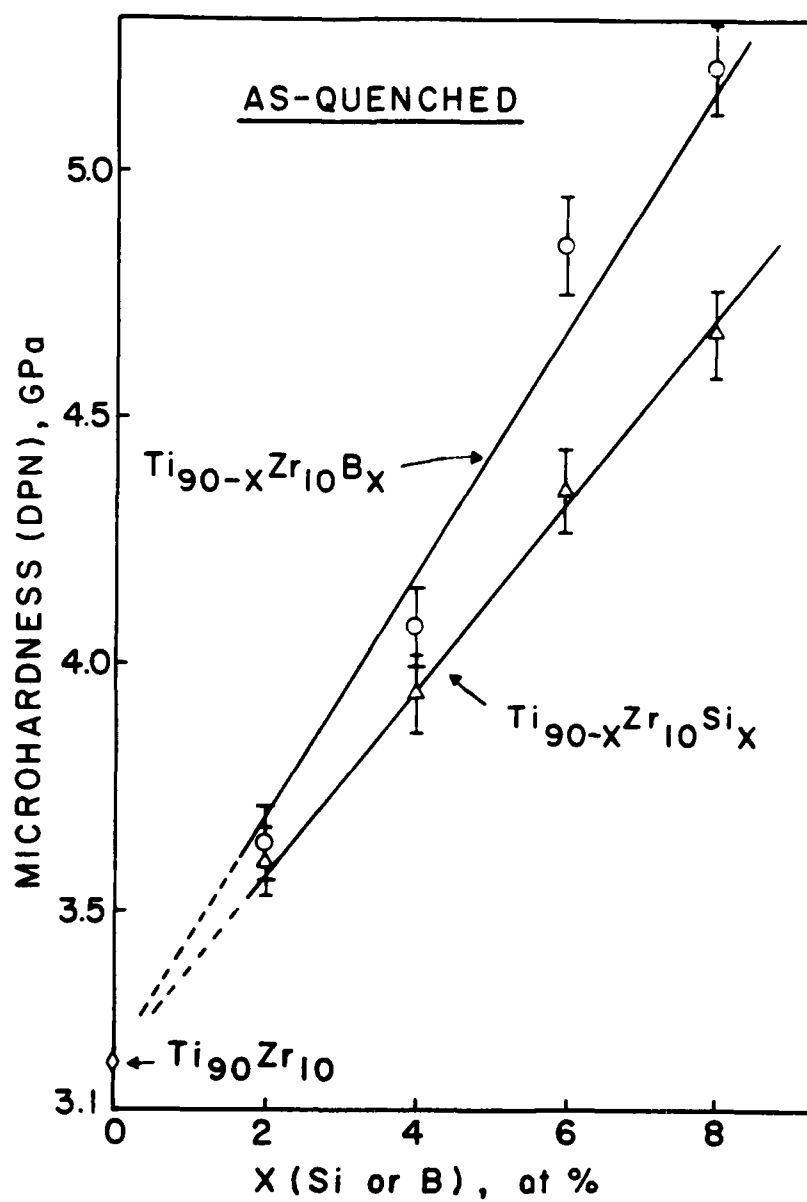


Fig. 8

AD-A149 609

ALLOY DEVELOPMENT PROCESSING AND CHARACTERIZATION OF
DEVITRIFIED TITANIUM. (U) NORTHEASTERN UNIV BOSTON MA
BARNETT INST OF CHEMICAL ANALYSIS. S H WHANG DEC 84
N00014-82-K-0597

2/2

UNCLASSIFIED

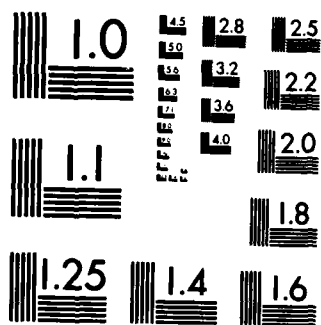
F/G 11/6

NL

END

FILMED

DTIC



MICROCOPY RESOLUTION TEST CHART
NATIONAL BUREAU OF STANDARDS-1963-A

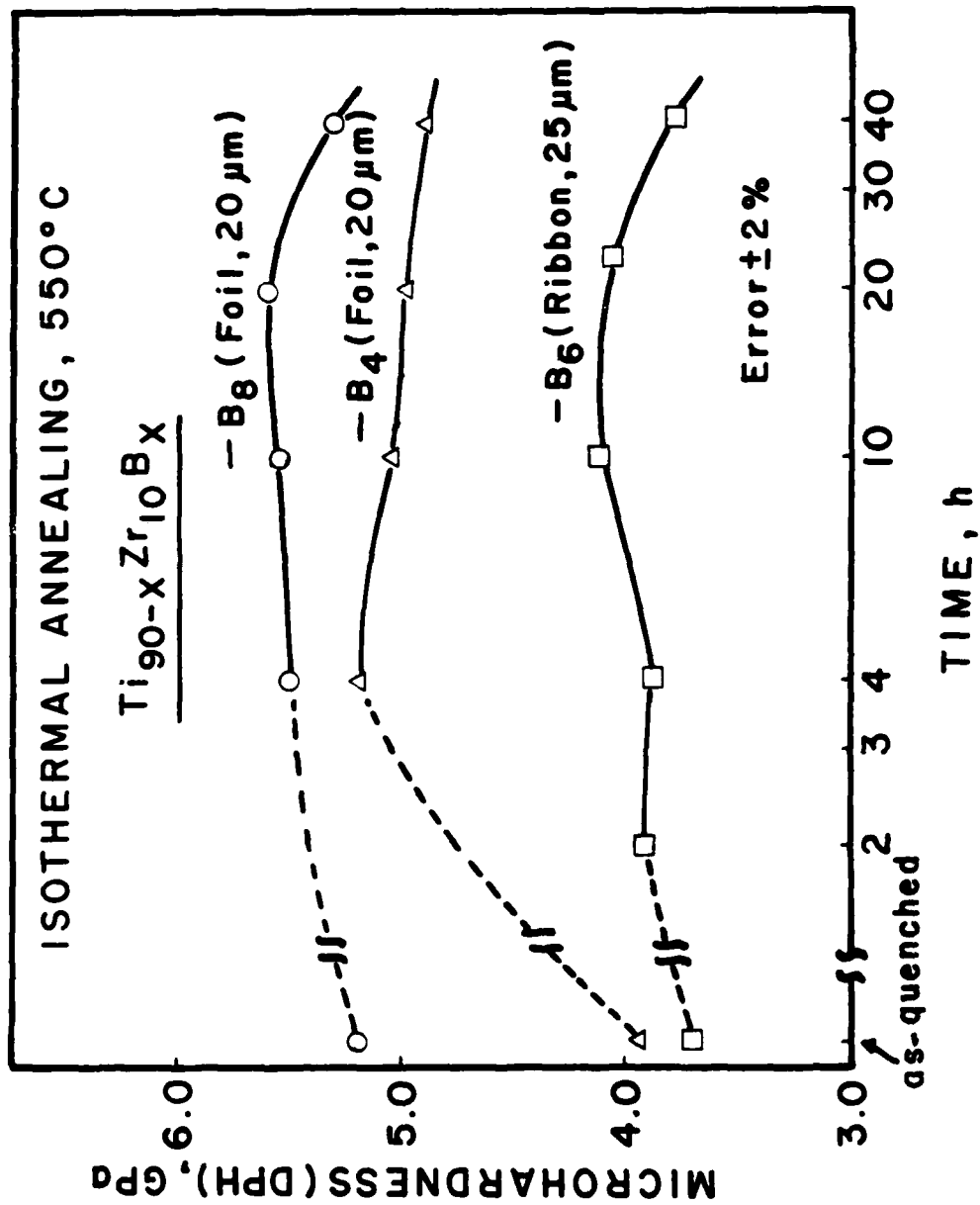


Fig. 9

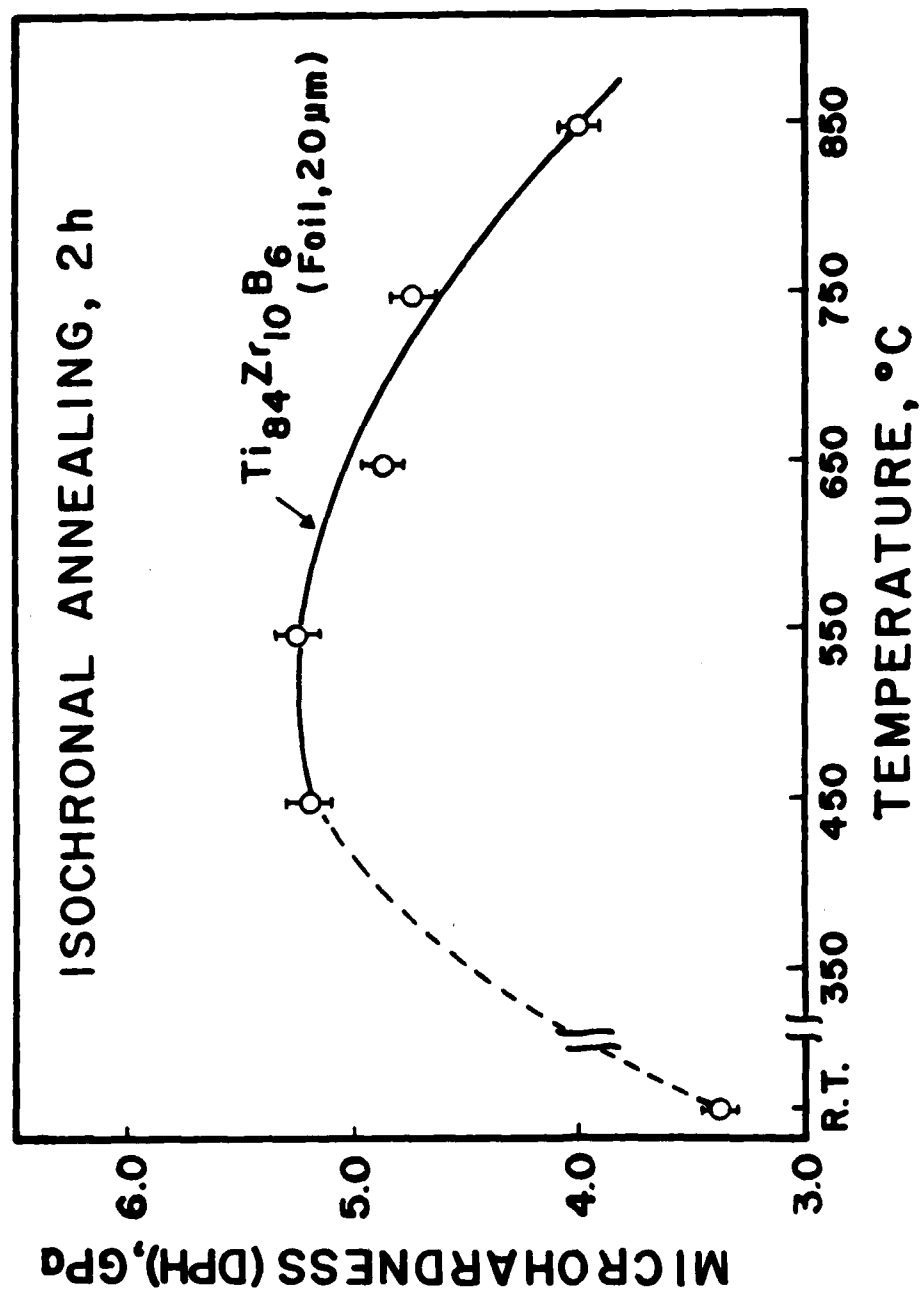


Fig. 10

END

FILMED

2-85

DTIC